Adsorption Energetics on Pd Model Catalysts by Microcalorimetry

Construction of a UHV Single Crystal Adsorption Microcalorimeter and Measurement of CO Adsorption Energetics as a Function of Particle Size

D I S S E R T A T I O N

zur Erlangung des akademischen Grades

doctor rerum naturalium
(Dr. rer. nat.)
im Fach Physik

eingereicht an der
Mathematisch-Naturwissenschaftlichen Fakultät I
der Humboldt-Universität zu Berlin

von
Dipl.-Phys. Jan-Henrik Fischer-Wolfarth (geb. Fischer)
10. Juli 1979 in Hannover

Präsident der der Humboldt-Universität zu Berlin:
Prof. Dr. Christoph Markschies

Dekan der Mathematisch-Naturwissenschaftlichen Fakultät I:
Prof. Dr. Andreas Herrmann

Gutachter:
1. Prof. Dr. Hans-Joachim Freund
2. Prof. Dr. Helmut Winter
3. PD Dr. Michael Gottfried

eingereicht am: 15. September 2010
Tag der mündlichen Prüfung: 14. Januar 2011

Abstract

The efficient use of the limited resources on earth is a critical factor to sustainable life. The development of better catalysts can make a significant contribution. Complete understanding of the catalytic activity would facilitate the design and control of specific catalytic processes. Consequently, by tuning of the catalytic reactivity, the amount of energy to run a reaction and the amount of waste products could be reduced significantly.

In this work, the correlation of the catalyst structure and the heats of adsorption of gas-phase particles was investigated. In particular, the heat of adsorption for CO on Pd particles was determined as a function of particle size, using a well-characterized model catalyst system, Pd particles supported on an iron oxide film, and UHV single crystal adsorption microcalorimetry.

The presented thesis is divided into two distinct parts. The subject of the first part is the construction and calibration of a new UHV adsorption microcalorimeter experiment. The second part presents results on adsorption heats on single crystals as well as oxide supported metal nanoparticles.

The completed microcalorimeter experiment comprises a preparation chamber and a calorimetry chamber, providing all means to prepare and characterize oxide supported metal nanoparticles and to perform adsorption energy measurements. The calorimeter is based on the design of Campbell *et al.*, using a pyroelectric β-PVDF ribbon as a detector. Improvements with respect to alignment, temperature stability, and vibration isolation were implemented. A pulsed molecular beam is used to expose the surface to a stable and homogeneous flux of gas-phase molecules. Further, a dedicated in situ reflectivity measurement setup allows optical characterization of the model catalyst surfaces, which is crucial for an accurate energy calibration of the calorimeter. The calorimeter shows a very good sensitivity and is capable to resolve deposited energy densities of about $120\,\mathrm{nJ/cm^2}$, which corresponds to an equivalent amount of $4 \cdot 10^{-4}$ monolayers of CO on Pt(111) (with a heat of adsorption of $130\,\mathrm{kJ/mol}$). A monolayer is defined by the number of Pt(111) surface atoms, being $1.5 \cdot 10^{15}\,\mathrm{cm^{-2}}$. The estimated heat of adsorption has a precision of 6.3 to 32.0% and an accuracy of about 5%.

The heats of adsorption for CO and benzene on Pt(111) were determined as a function of coverage, being initially $(130 \pm 3)\,\mathrm{kJ/mol}$ and $(119 \pm 3)\,\mathrm{kJ/mol}$ at room temperature, respectively. For the first time, the heat of adsorption of CO was measured also at 120 K, coinciding mainly with the room temperature data. The initial heat of adsorption was $(124 \pm 3)\,\mathrm{kJ/mol}$. The obtained data are compared to previous studies, verifying the proper functioning of the calorimeter experiment by the good agreement.

By the unique combination of single crystal adsorption calorimetry, molecular beam techniques and supported model catalysts, it was possible to resolve the longstanding controversy, how the heat of adsorption of CO on Pd particles changes with particle size. The heat of adsorption for CO on Pd particles was studied on Fe_3O_4 supported Pd particles with a mean diameter of 1.8 to 8 nm and Pd(111). The initial heat of adsorption was found to decrease with decreasing particle size. Presumably, this observation can be rationalized as a reduction of the chemisorption strength and the Van der Waals interaction.

Zusammenfassung

Die effiziente Nutzung der begrenzten Ressourcen auf der Erde ist ein entscheidender Faktor für ein nachhaltiges Leben. Die Entwicklung besserer Katalysatoren kann dabei einen wesentlichen Beitrag leisten. Ein umfassendes Verständnis der katalytischen Reaktivität würde es ermöglichen, spezifische katalytische Eigenschaften zu konzipieren und zu kontrollieren. Somit könnte durch gezielte Veränderung der katalytischen Reaktivität der Energieaufwand chemischer Reaktionen und die Produktion von ungewünschten Nebenprodukten erheblich reduziert werden.

In diese Arbeit wurde die Korrelation der Katalysatoroberfläche mit den Adsorptionswärmen von Molekülen aus der Gasphase untersucht. Insbesondere wurde die Adsorptionwärme von CO auf Pd-Partikeln als Funktion der Partikelgrösse mittels gut charakterisierte Modelkatalysatorsysteme, eisenoxidgeträgerte Pd-Partikel, und UHV-Einkristalladsorptionskalorimetrie bestimmt.

Die vorliegende Arbeit ist in zwei Abschnitte unterteilt. Der erste Abschnitt beinhaltet den Aufbau und die Kalibration eines neuen UHV-Einkristalladsorptionskalorimetrie-Experiments. Der zweite Abschnitt befasst sich mit Adsorptionswärmemessungen auf Einkristallen und Oxidfilm geträgerten Pd-Partikeln. Das Mikrokalorimeterexperiment besteht aus einer Präparationskammer und einer Kalorimetriekammer, die sowohl die Präparation und Charakterisierung von geträgerten metallischen Nanopartikeln, als auch Adsorptionsenergiemessungen ermöglichen. Das Kalorimeter basiert auf dem Design von Campbell *et al.* und nutzt eine pyroelektrische β-PVDF Folie als Detektor. Es wurden Verbesserungen in Bezug auf Ausrichtung, Temperaturstabilität und Vibrationsisolation implementiert. Eine gepulster Molekularstrahl wird eingesetzt, um die Oberfläche einem stabilen und homogenen Flusss von Gasphasenmolekülen auszusetzten. Desweiteren erlaubt ein in situ Reflektivitätsmessaufbau die Bestimmung optischer Eigenschaften von Modelkatalysatoroberflächen, was entscheidend für eine akkurate Energiekalibration des Kalorimeters ist. Das Kalorimeter ermöglicht es deponierte Energien bis etwa $120\,\mathrm{nJ/cm^2}$ aufzulösen, was der Adsorption von $4 \cdot 10^{-4}$ Monolagen von CO auf Pt(111) (mit einer Adsorptionswärme von $130\,\mathrm{kJ/mol}$) entspricht. Eine Monolage ist durch die Anzahl von Oberflächenatomen von Pt(111), $1{,}5 \cdot 10^{15}\,\mathrm{cm^{-2}}$, gegeben. Adsorptionsenergiemessungen haben einen statistische Fehler zwischen $6{,}3$ und $32{,}0\%$ und einen systematische Fehler von circa 5%.

Die Adsorptionwärmen von CO und Benzol auf Pt(111) wurden als detailierte Funktion der Bedeckung bestimmt. Die Anfangsadsorptionswärmen für CO und Benzol waren $(130 \pm 3)\,\mathrm{kJ/mol}$, beziehungsweise $(119 \pm 3)\,\mathrm{kJ/mol}$ bei Raumtemperatur. Erstmalig wurde die Adsorptionswärme für CO auf Pt(111) bei $120\,\mathrm{K}$ gemessen. Die Daten stimmen im Wesentlichen mit den Daten der Raumtemperaturadsorption überein und die Anfangsadsorptionswärme beträgt $(124 \pm 3)\,\mathrm{kJ/mol}$. Die gute Übereinstimmung mit früheren Studien verifiziert das einwandfreie Funktionieren des Kalorimeterexperiments.

Die einmalige Kombination von Einkristalladsorptionskalorimetrie, Molekularstrahltechniken und geträgerter Modelkatalysatoren ermöglichte es, die langjährige Kontroverse, wie sich die Adsorptionswärme von CO auf Pd mit der Partikelgrösse ändert, aufzulösen. Die Adsorptionswärmen wurde für CO auf Fe_3O_4 geträgerten Pd-Partikeln mit mittleren Größen zwischen 1.8 und $8\,\mathrm{nm}$, sowie Pd(111) untersucht. Es zeigte sich dabei, dass die Anfangsadsorptionsenergie mit abnehmender Partikelgrösse kleiner wird. Für die kleinsten Partikel wurde eine Anfangsadsorptionswärme von $(106 \pm 2)\,\mathrm{kJ/mol}$ bestimmt, im Vergleich zu $(149 \pm 4)\,\mathrm{kJ/mol}$ auf der ausgedehnten Pd(111) Oberfläche. Vermutlich kann diese Beobachtung durch eine Abnahme der Chemisorptions- und der Van-der-Waals-Wechselwirkung erklärt werden.

Contents

1. Introduction

Heterogeneous catalysis is of high environmental importance. With its wide field of industrial applications — comprising chemical synthesis, energy storage and conversion [1, 2] as well as environmental chemistry [3] — an improved understanding of heterogeneous catalysis is of vital interest for a more efficient use of the limited resources on earth. Fundamental research can make a substantial contribution by the development of a detailed microscopic understanding, which would facilitate the design and control of reaction kinetics by tuning the appropriate properties of the catalyst, most notably the activity and the selectivity. Both, activity and the selectivity, are related to the catalyst's geometric and electronic structure and the catalyst's surface may contain several active components, e.g. transition metals or oxides, and a characteristic shape. In industrial applications, the active components are commonly finely dispersed as particles on porous supports. Primarily, the dispersion maximizes the surface area. However, the reduced dimensions of the active components can change the geometric and electronic structure of the catalysts significantly [4], where both of which can be influenced also by a particle-support interaction. Further, the supports themselves may be catalytically active and contribute to the reaction kinetics. Accordingly, the catalytic activity of a supported system depends sensitively on the structural parameters, i.e. particle size and shape, [4–8] and the properties of the support [9–11].

Investigations on industrial catalysts suffer from their vast complexity. Additionally, detailed microscopic insights are essentially concealed because of ill-defined surface properties that are related to the porosity and the commonly low electrical conductivity of the supports, limiting the number of applicable methods. Comprehensive efforts, using surface science methods, are therefore restricted to catalyst systems with reduced complexity. By a systematic approach that correlates the surface properties of the catalysts with its activity, a detailed understanding of the reaction kinetics and their underlying surface interactions can be obtained [12]. Early studies focused on metal single crystal surfaces, including stepped and defect-rich surfaces [13, 14]. These experiments provided important data for the catalytic activity of ideal and defect rich surfaces. However, extended surfaces do not resemble supported catalysts as neither confinement effects nor particle-support interactions are present. To resolve this problem a variety of supported model catalysts was developed, consisting of catalytically active components supported on thin oxide films or oxide single crystals [8, 15]. Foremost, the applicability of surface science methods is granted, e.g. electron and photon spectroscopies as well as scanning tunneling spectroscopy, allowing to study heterogeneous catalysis on disperse particles at the atomic level [16–19]. This microscopic characterization enables the comparison of experimental results with detailed theoretical modeling. Further, supported model catalysts offer the opportunity to control the complexity of the system, namely the composition and structure of the active components and also the structure of the oxide support. The successful concept of using model catalysts, catching part of the complexity of real catalysts, was reviewed recently [20].

Object of this work

One of the key aspects in heterogeneous catalysis is the binding energy of the adsorbate to the surface, i.e. the adsorption energy, as it comprises one of the first elementary steps in the catalytic cycle. The gas-surface interaction strength depends not only on the composition of the surface but also on its structural properties. Consequently, the determination how surface structure relates to the gas-surface interaction is a fundamental issue in the course of understanding the adsorbate dynamics and its reaction kinetics. Therefore an exact quantitative correlation of structural properties and interaction strength is needed. In particular, this work addresses the question how the heat of adsorption for CO on Pd particles changes with particle size. Earlier attempts to determine the adsorption energy of carbon monoxide on Pd particles as a function of particle size, using temperature desorption spectroscopy and molecular beam relaxation, reported conflicting results [21, 22]. The corresponding analyses were based on kinetic models of the desorption processes and relied on assumptions on the pre-exponential factors. Consequently, the direct measurement of the adsorption energy is unavoidable to circumvent the encountered limitations of kinetic modeling and is feasible by single crystal adsorption calorimetry. Single crystal adsorption calorimetry is based on the detection of the temperature rise of the surface up on adsorption. It involves no further assumption as the adsorption signal can be calibrated by comparison to laser light absorption [23]. Single crystal adsorption calorimetry was successfully pioneered by King *et al.* [24] who reported a collection of adsorption energies on single crystals [25]. In the present work, single crystal adsorption calorimetry was combined with molecular beam techniques and supported model catalysts. The supported model catalyst employed in this work consists of Pd particles supported on an iron oxide film, $Pd/Fe_3O_4/Pt(111)$, and was extensively characterized in our department with respect to its electronic and geometric structure as well as to its adsorption properties.

Realization and Accomplishment

The present thesis is structured in two parts which constitute the major steps in the accomplishment of the set object of determining the heat of adsorption of carbon monoxide on Pd particles as a function of particle size. Prior to these two parts, chapter 2 introduces relevant gas-particle dynamics at surfaces with a focus on gas-surface interaction and adsorption.

Part I

The first part describes in detail the successful realization and calibration of a new UHV adsorption calorimeter experiment. Completing the construction of the experimental setup was a major milestone in the course of this work. Its design requirements were not only focused on the current project, but should enable further studies involving supported model catalysts. Therefore the following design requirements had to be met:

- Facilities to prepare and characterize supported model catalysts on ultrathin single crystals (about 1 μm) have to be incorporated.

- For an accurate energy calibration of the calorimeter the optical reflectivities of the supported model catalysts have to be determined in situ.
- The number of adsorbed molecules has to be known.
- The calorimeter should be able to resolve the temperature rise induced by small amounts of adsorbates (covering about 1% of the surface).
- During calorimetric measurements the temperature of the surface should be controllable in the range of 100 to 300 K in order to control the adsorbate species that is formed on the surface.
- Thermal desorption spectroscopy should be possible to compare adsorption and desorption energies for reversible processes.

The challenge in calorimetry lies in a good accuracy and precision. Accordingly great care was taken in every step of the implementation to maximize the significance of the calorimetric measurement. Chapter 3 gives a general introduction to the experimental surface science techniques that were implemented and used in this work. Chapter 4 contains a detailed description of the experimental setup, which comprises a preparation chamber and a calorimetry chamber. The preparation chamber contains all means to prepare and characterize supported model catalysts and single crystals. In particular, it incorporates an in situ reflectivity measurement setup, which is necessary for an accurate energy calibration of the calorimeter. After successful preparation and characterization, the samples can be transfered to the calorimetry chamber by a transfer stage. The calorimetry chamber contains the calorimeter, a pulsed effusive molecular beam and detectors for the absolute calibration. The implementation of the single crystal adsorption calorimeter is based on the design reported by Campbell *et al.* [26], using a pyroelectric β-PVDF detector in contact with the single crystal, allowing measurements below 300 K. A pulsed effusive molecular beam is used to provide gas-particles onto the surface, and the adsorbed fraction of the molecular beam pulse is quantified by a sticking probability measurement. Chapter 5 discusses the calibration of the system components, which are important for the determination of (i) the amount of deposited energy upon adsorption and (ii) the number of adsorbed molecules.

Part II

The second part covers the determination of adsorption heats on single crystals and supported model catalysts.

The first adsorption experiments were performed on single crystals and intended to verify the proper functioning of the calorimeter setup. Chapter 6 describes the acquisition of sticking probabilities and deposited energies as a detailed function of coverage for carbon monoxide and benzene on Pt(111). Thereby, the according heats of adsorption at 298 K were derived. For the first time, the heat of adsorption at 120 K was determined for CO adsorption on Pt(111). The results are discussed with respect to the available data on the adsorption energies from indirect methods, like thermal desorption spectroscopy, as well as previous single crystal adsorption calorimetry measurements by other groups.

Chapter 7 covers the determination of the particle size dependent heat of adsorption of carbon monoxide on Pd nanoparticles. These calorimetric experiments establish an accurate correlation of the catalyst structure, i.e. its size, and its interaction strength with gas phase particles. The CO adsorption experiments on iron oxide supported Pd particles are described where the particle size was systematically varied between 1.8 and 8 nm. The previous characterization of the Pd/Fe_3O_4/Pt(111) model catalyst is reviewed. The Pd particles were found to exhibit mainly (111) facets. Therefore the heat of adsorption for CO was also determined on Pd(111), which serves as a reference for extended surfaces. It was found that the heat of adsorption decreases with decreasing particle size. Finally, the most important achievements of this work are summarized in chapter 8.

2. Dynamics at Surfaces

In this chapter, a brief overview of dynamic processes of molecules at surfaces is provided, dealing with the adsorption and binding of molecules to surfaces as well as adsorbate dynamics. Finally, the effects of surface-confinement encountered with oxide supported metal nanoparticles will be discussed.

Gas-phase particles near a surface are affected by the interaction with the surface's potential. In figure 2.1 simple particle dynamics are depicted for incident gas-phase particles. Incident gas-phase particles may scatter elastically or inelastically, see figure 2.1a or adsorb, see figure 2.1b where also the adsorbate dynamics, i.e. diffusion, desorption, and possible reaction upon successful adsorption is shown. More details on these processes will be given below.

2.1. Adsorption: Gas-Surface Interaction

The reason for adsorption is the attractive interaction of gas-phase particles and the surface This gas-surface interaction is commonly divided into two regimes, physisorption and chemisorption.

Physisorption

Physisorption is a process of weak interaction between an atom or a molecule with a surface in which the electronic structure of the gas phase atom or molecule is barely perturbed upon

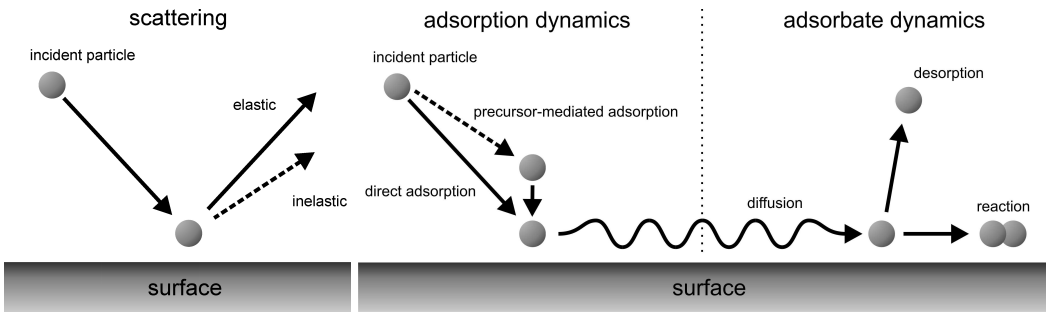

(a) Scattering **(b)** Adsorption and Adsorbate Dynamics

Figure 2.1.: Schematic overview of elementary surface dynamics: scattering (elastic and inelastic), adsorption dynamics (direct and precursor-mediated adsorption), and adsorbate dynamics (diffusion, desorption, and reaction)

adsorption, i.e. there is hardly any mixing of the electron wave functions, or in other words, electrons are not shared in a new covalent bond. Although, it has to be mentioned that the chemical bonds within the adsorbate can be significantly polarized. Physisorption can be conveniently discussed in terms of two opposite interactions: an attractive Van der Waals interaction and Pauli repulsion.

When a polar particle, either an atom or a molecule, approaches a surface, it will set up an according image dipole moment induced on the surface of a polarizable medium. This leads to an attractive dipole interaction. The same is also true for nonpolar atoms or molecules where random quantum fluctuations are the source of an induced dipole interaction resulting in the London dispersion force. Figure 2.2 shows a schematic drawing of a dipolar particle in vacuum at distances R from a metal surface and its corresponding image charge. The potential energy of the Van der Waals interaction can be written as [27]:

$$V_{VdW} = \frac{e^2}{4\pi\varepsilon_0}\left(\frac{-1}{2\,|\mathbf{R}-\mathbf{R'}|}+\frac{-1}{2\,|(\mathbf{R}+\mathbf{r})-(\mathbf{R'}+\mathbf{r'})|}+\frac{1}{2\,|\mathbf{R}-(\mathbf{R'}+\mathbf{r'})|}+\frac{1}{2\,|(\mathbf{R}+\mathbf{r})-\mathbf{R'}|}\right) \tag{2.1}$$

$$\Longleftrightarrow V_{VdW} = \frac{e^2}{4\pi\varepsilon_0}\left(\frac{-1}{4d}+\frac{-1}{4(d+z)}+\frac{1}{2\,|(2\mathbf{R}-\mathbf{r'})|}+\frac{1}{2\,|(2\mathbf{R}+\mathbf{r})|}\right), \tag{2.2}$$

where **R** and **R'** define the position of the positive charge and its image charge with respect to the surface at a distance d, and **r** the position of the negative charge with respect to the position of the positive charge. The first two terms in equation 2.2 describe the attraction between the nucleus and its image charge and the electron and its image charge, and the last two terms describe the corresponding coulomb repulsions. Equation 2.2 can be expanded in a Taylor-series in terms of $|\mathbf{r}|/|\mathbf{R}|$:

$$V_{VdW} = -\frac{e^2}{4\pi\varepsilon_0}\frac{1}{8d^3}\left(\frac{x^2+y^2}{2}+z^2\right). \tag{2.3}$$

So the Van der Waals interaction is attractive overall and generally behaving as:

$$V_{VdW} \propto -\frac{C_{VdW}}{d^3}, \tag{2.4}$$

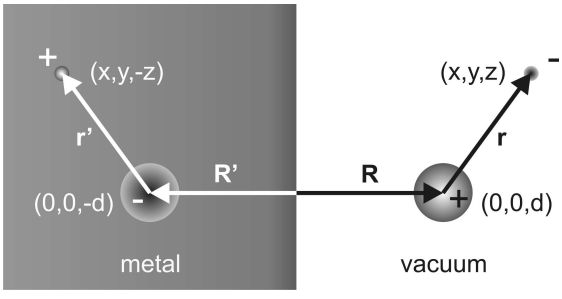

Figure 2.2: Schematic drawing of a dipolar particle with the corresponding image charge in a polarizable medium

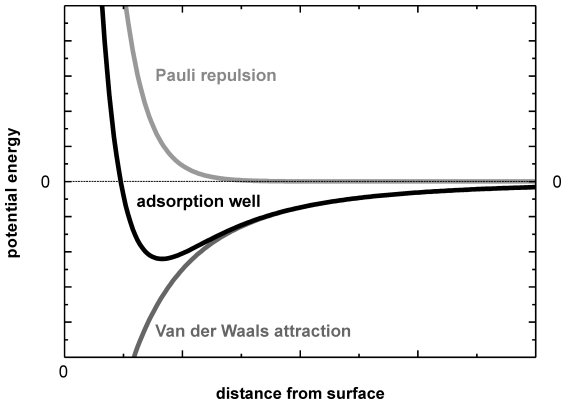

Figure 2.3: Physisorption potential as a superposition of an attractive Van der Waals potential and a Pauli repulsion potential. The depth of the adsorption well governs the adsorption energy.

where C_{VdW} is the Van der Waals constant, which depends on the polarizability of the particle and the response of the surface medium. The polarizability α is defined as the ratio of the induced dipole moment p in an electric field E:

$$\alpha = \frac{p}{E} \tag{2.5}$$

The polarizability is directly related to the permittivity ε of the medium, also known as the dielectric constant.

At small distances d the electrons of the atom or molecule and the surface begin to interact strongly. The electron wave functions have to orthogonalize as a consequence of the Pauli principle resulting in a repulsive exchange interaction. A simple approximation of this repulsive potential V_R is based on the exponential decay in electron density:

$$V_R \propto e^{-\frac{d}{a}}, \tag{2.6}$$

where a is a characteristic length.

The physisorption potential results from superposition of the attractive and the repulsive interaction potentials:

$$V_{Physisorption} = V_R + V_{VdW} \cong C_R e^{-\frac{d}{a}} - \frac{C_{VdW}}{d^3}, \tag{2.7}$$

where C_R is a constant accounting for the magnitude of the Pauli repulsion. Figure 2.3 shows the resulting adsorption well. Obviously, this approximation is not valid for small d, where for $d \to 0$ the term of the Pauli repulsion would become constant ($V_R \to C_R$) in contrast to an infinitely strong term for the Van der Waals attraction ($V_{VdW} \to \infty$).

Chemisorption

Chemisorption is defined by the mixing of the adsorbate's and the surface's charge densities, or in other words, by the formation of valence bonds usually accompanied by an effective charge

transfer. As a consequence, the electronic structure changes upon adsorption with respect to the gas phase atom or molecule and the clean surface [28].

A complete knowledge of chemisorption phenomena requires the determination of:

- the geometrical structure of the system
- the adsorption sites
- the adsorbate's binding and diffusion activation energy,
- the electronic structure of the adsorbate and the substrate,

Adsorption on a Transition Metal

Transition metals have a broad sp band and a narrow intense d band. The adsorbate interaction with the sp band results in a lowering and broadening of the adsorbate energy levels. Additionally, the strong interaction of the adsorbate levels with the d-band, which can be considered as a broad orbital itself, results in formation of bonding and antibonding orbitals. The important implication is a weakening of intramolecular bonds for molecules with antibonding orbitals below the Fermi energy. This weakening facilitates the dissociation of the adsorbate, a key process in heterogeneous catalysis. For CO, a first comprehensive model was introduced by Blyholder [29], in which binding occurs via a charge transfer from the 5σ orbital of CO to the metal and a backdonation from the metal into the antibonding $2\pi^*$ orbital of CO. More details about CO-Pd interaction will be given in section 7.2.1.

Effect of Stress and Strain in the Metal

Stress and strain in the surface affects the interatomic distances of the surface metal atoms, causing a change in the overlap of the electronic orbitals and consequently in the electronic structure of the surface [30]. A decreasing overlap, caused by an increasing interatomic distance, results in a narrowing of the d band as well as a shift in energy to lower electron binding energies. Therefore, the chemisorption bond to an adsorbate is strengthened. On the other hand, an increasing overlap caused by decreasing interatomic distance, results in a broadening of the d band as well as a shift in energy to higher electron binding energies. This observation allows one to rationalize typically observed higher adsorption energies at low-coordination site. Low-coordination site lack neighboring atoms. The resulting reduced overlap of electron wave functions narrows the d band and shifts it to lower electron binding energies.

Heats of Adsorption

The most important quantity for the description of the phenomenon of adsorption is the binding energy between adsorbate and surface. A quantity that describes this interaction strength of the adsorbate with the surface is the heat of adsorption. There are two definition of the isothermal heat of adsorption, referring to the difference in the total energies E_i or in the enthalpies H_i of

the *surface system* and the *adsorbate covered surface system* [31]:

$$q_{st} \equiv h_{surface} - h_{adsorbate+surface} \quad \text{(isosteric heat of adsorption)} \tag{2.8}$$

$$q_d \equiv e_{surface} - e_{adsorbate+surface} \quad \text{(differential heat of adsorption)}, \tag{2.9}$$

where the lower case letters refer to the molar quantities of the energy e_i and the enthalpy h_i at constant pressure p , temperature T, and surface area A. The heats of adsorption are related in good approximation by:

$$q_{st} \cong q_d + RT \ , \tag{2.10}$$

where R is the gas constant. RT originates from the volume work present in the enthalpies. More details can be found elsewhere [31–35].

Indirect Measurement of Adsorption Energies

The heat of adsorption can be determined indirectly by measuring the temperature dependence of the equilibrium between gas phase and the adsorption phase. Equilibrium adsorption isotherms yield the isosteric heat of adsorption q_{st}, which is related to pressure p and temperature T at a constant coverage of adsorbates on the surface as follows:

$$\left(\frac{\mathrm{d}\, ln(p)}{\mathrm{d}T}\right)_{\theta} = \frac{-q_{st}}{RT^2} \ , \tag{2.11}$$

where θ refers to the adsorbate coverage. The analysis is restricted to reversible adsorption process, as it considers an adsorption system in equilibrium state. This equation refers to a system where the adsorbate resides on a truly inert substrate. In other words, equation 2.11 can only rigorously be applied to weakly interacting physisorbate systems. For chemisorbates, this equation is not strictly applicable because the thermodynamic parameters of adsorbate and surface cannot be separated. More details can be found elsewhere [32–34]

Thermal desorption spectroscopy experiments also give access to a quantitative analysis of the adsorption energy E_{ads}, linking the desorption activation energy E_{des} to the adsorption energy by the assumption that the desorption process is the reverse of the adsorption process and $E_{ads} \approx E_{des}$. Thermal desorption is usually described in the form of an Arrhenius expression, often called the Polanyi-Wigner equation:

$$r(\theta, T) = \frac{\mathrm{d}\theta}{\mathrm{d}t} = \nu(\theta)\theta^n \exp\left(-\frac{E_{des}}{RT}\right), \tag{2.12}$$

where r is the rate of desorption, θ the adsorbate coverage, ν the frequency factor, n the order of desorption, R the gas constant, T the temperature and E_{des} the desorption activation energy. In an adsorption-desorption equilibrium, the desorption activation energy E_{des} is approximately related to the isosteric heat of adsorption by [36]:

$$E_{des} \cong q_{st} - \frac{1}{2}RT \ . \tag{2.13}$$

The complication in TDS arises from the fact that the parameters governing the desorption rate,

namely the desorption activation energy E_{des} and the frequency factor ν can strongly depend on the surface coverage θ. The order of desorption n has to be accounted for. In general, the order of desorption n and the frequency factor ν are unknown. Therefore different approaches – using different assumptions – for the analysis of the thermal desorption spectra exist [37, 38], e.g. the *Redhead analysis* [39], the *Leading Edge Analysis* [40] or the *Complete Analysis* [41]. TDS analysis is limited to fully reversible adsorption processes. It can not be applied accurately to adsorption processes involving dissociation, cluster formation, diffusion into the bulk or reaction with co-adsorbates.

Direct Measurement of Adsorption Energies

The adsorption heat can be determined directly by calorimetry. In addition to fully reversible processes also adsorption processes involving dissociation, cluster formation, diffusion into the bulk or reaction with co-adsorbates can be probed. The calorimetrically measured energy q_{cal} is determined by the energy difference of the *surface system* and the *adsorbate covered surface system* and could have principally a contribution from volume work, but it is unclear how much will contribute to the detected heat [32]. Therefore q_{cal} will be in between the isosteric heat of adsorption and the differential heat of adsorption:

$$q_d \leq q_{cal} \leq q_{st} \ . \tag{2.14}$$

The adsorption heat can be measured by detection of the induced temperature change in the surface, either by contact or non-contact temperature measurement methods. The comparison of molecular adsorption to light absorption enables one to determine an absolute energy calibration. Further, molecular beam techniques and sticking probability measurements enable one to determine the amount of adsorbed gas-particles accurately. A detailed description of the calorimeter measurement scheme is presented in section 3.1.1.

2.2. Adsorption Dynamics

A gas-phase particle interacting with a surface can be scattered elastically or inelastically. If enough kinetic energy in the direction perpendicular to the surface is transfered it may get trapped in the surface potential. Figure 2.4 shows one-dimensional representations of possible trajectories on two different potential energy surfaces, where a physisorption well is at distance r_{phy} from the surface, and a chemisorption well at distance r_{chem}. Scattering will occur either elastically, case 1 in 2.4a, or inelastically, cases $2-6$. Inelastic scattering may lead to entering an adsorption state, cases $3-6$.

The adsorption process can be non-activated or activated. For non-activated adsorption, the molecule does not encounter an energetic barrier. Accordingly, activated adsorption is characterized by an energetic barrier that has to be overcome. The barrier may relate to the ongoing restructuring of the adsorbing atom's or molecule's electronic and geometric structure (including dissociation) finally resulting in the formation of a chemical bond to the surface. Figure 2.4a and 2.4b show non-activated (case 3 and 4) and activated (case 5) adsorption processes , respectively.

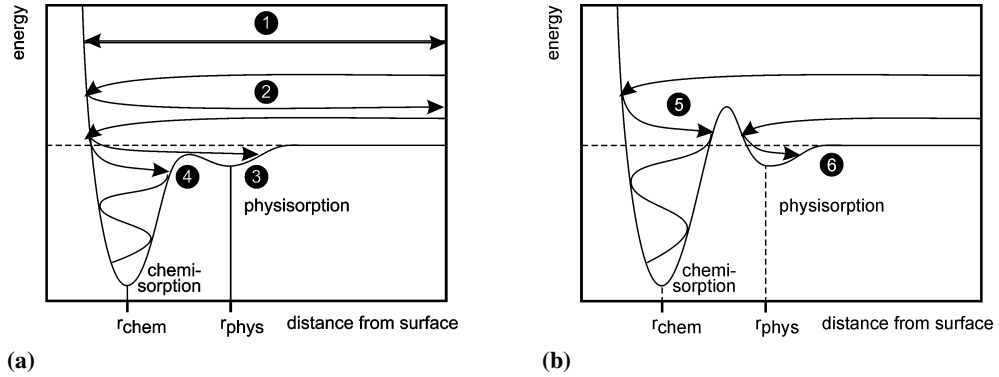

Figure 2.4.: One-dimensional representation of possible trajectories on the potential energy surface for (a) non-activated adsorption and (b) activated adsorption, after [42]

For activated chemisorption the atom or molecule may access the chemisorption well r_{chem} directly, case 5 in figure 2.4b, or via the population of a physisorbed precursor state, case 6, where energy from the surface may be transfered to the atom or molecule enabling it to overcome the energy barrier. Physisorption, in contrast to chemisorption, is always non-activated.

Precursor-Mediated Adsorption

The adsorption may be mediated by a precursor state through which the adsorbing atom or molecule passes on its way to the chemisorption state. Precursor mediated adsorption was observed in numerous systems, including e.g. CO on Pt(111) [43, 44]. In contrast to the Langmuir type of adsorption, it is characterized by high sticking probabilities, which remain nearly constant until the saturation coverage is reached. This phenomenon arises from the ability of the incoming molecules to stick not only to the empty surface sites, but also to get trapped on-top of the adsorbate overlayer, already formed on the surface and diffuse across to find an appropriate empty position.

Sticking Probability

In order to stick to the surface the atom or molecule has to lose its kinetic energy normal to the surface. The sticking probability of an impinging atom or molecule on a surface refers to the likelihood that it will successfully adsorb on the surface. The sticking probability S is defined as the ratio of the number of adsorbed atoms or molecules $\mathrm{d}N_{ads}$ over the number of impinging atoms or molecules $\mathrm{d}N_{imp}$:

$$S(\theta) = \frac{\mathrm{d}N_{ads}}{\mathrm{d}N_{imp}} \,. \tag{2.15}$$

The sticking probability can crucially depend on the surface coverages θ_i of species i, the mass relation of the atom or molecule and the surface atoms governing the momentum transfer and the number of excitable internal degrees of freedom in the molecule to incorporate the energy. Experimentally, the sticking probability can be derived from the amount of scattered atoms or

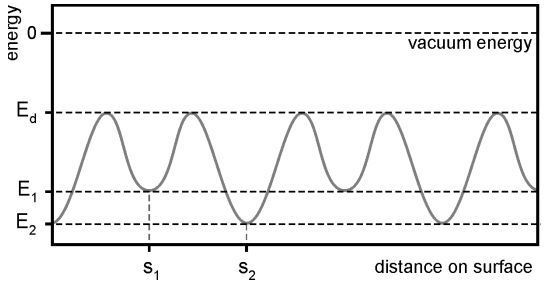

Figure 2.5: Energy potential along the surface with two non-equivalent adsorption sites s_1 and s_2 exhibiting adsorption energies of E_1 and E_2, correspondingly, and a diffusion barrier E_d, after [31]

molecules ΔN_{sca} for a finite coverage increment of $\Delta N_{ads} = \Delta N_{imp} - \Delta N_{sca}$ by the *King-Wells method* [45]:

$$S(\theta) = \frac{\Delta N_{ads}}{\Delta N_{imp}} = 1 - \frac{\Delta N_{sca}}{\Delta N_{imp}} \tag{2.16}$$

The *King-Wells method* and its actual adaption in the present experiment will be discussed in more detail in section 3.3.

2.3. Dynamics of Adsorbates

Diffusion and Desorption

After adsorption the molecule – in thermal equilibrium with the underlying solid– is located at an adsorption site. Thermal fluctuations, however, drive the particle back to the vacuum/gas phase or enable it to jump laterally along the surface from one site to the next. These processes are denoted as desorption and diffusion, respectively. Obviously, both processes are governed mainly by the surface temperature, since an activation barrier has to be overcome to leave the potential minimum. The activation energies for diffusion are generally much smaller than for desorption. Therefore an atom or a molecule typically performs a large number of diffusion steps before leaving the surface.

Diffusion

Diffusion in general is described by the *diffusion equation* [46]:

$$\frac{\partial c(\vec{r},t)}{\partial t} = \nabla \cdot (D(c,\vec{r})\nabla c(\vec{r},t)), \tag{2.17}$$

where t is the time, $c(\vec{r},t)$ is the density of adsorbates on a unit area at location $\vec{r}$ and $D(c,\vec{r})$ the diffusion coefficient. The diffusion equation is nonlinear if the diffusion coefficient D is a function of the location, e.g. depending on the inhomogeneous adsorbate density $c(\vec{r},t)$, which is the case, for instance, when the adsorbates interact with each other. The root mean square distance $\langle d \rangle^{1/2}$ traveled by an adsorbate diffusing on the surface is defined by the residence time t and the diffusion coefficient D:

$$\langle d \rangle^{1/2} = (4Dt)^{1/2} \tag{2.18}$$

The diffusion of an adsorbate on a surface, especially at low coverage, can be considered in

good approximation as hopping between adsorption sites, where the potential energy has local minima. Therefore, diffusion is an activated process. Figure 2.5 shows such a one-dimensional potential energy surface exhibiting two nonequivalent adsorption site s_1 and s_2 with adsorption energies, E_1 and E_2, and a uniform diffusion barrier E_d. Atoms or molecules residing in these adsorption sites have to overcome the diffusion barrier in order to move to an adjacent adsorption site. Diffusion barriers need not be uniform across a surface.

Adsorbates may diffuse on the surface at a rate depending on the ratio of thermal energy k_BT and diffusion barrier E_d parallel to the surface. Based on this approximation, assuming a uniform potential, and neglecting interadsorbate interaction, the diffusion coefficient D can be expressed as:

$$D = D_0 \cdot \exp\left(\frac{E_d}{k_BT}\right) \tag{2.19}$$

For $E_d \ll k_BT$, the adsorbates behave like a two-dimensional gas. For $E_d \geq k_BT$, translational degrees of freedom are frozen out, leading to an immobile adsorbate for the limit of $E_d \gg k_BT$.

Desorption

As the adsorbate is trapped in a potential well of finite depth, it is naturally possible that the particle can overcome the desorption barrier E_{des} by gaining enough energy. The desorption can be thermally stimulated. The desorption rate R_{des} can be expressed with help of transition-state-theory [47]:

$$r(\theta,T) = \nu \cdot \exp\left(-\frac{E_{des}}{k_BT}\right)(\theta)^n \tag{2.20}$$

where θ is the surface coverage, T is the surface temperature, ν is the frequency factor, E_{des} the desorption activation energy, and n the order of desorption. In simple examples the desorption order n is identical to the molecularity and integer values of n are given for coverage independent desorption ($n = 0$), molecular desorption ($n = 1$) and recombinative desorption ($n = 2$). Desorption involving lateral interactions between adsorbates, i.e. repulsion or island formation, often shows a non integer desorption order. In many cases, the desorption order n is not known.

Thermal desorption typically occurs with an energy distribution characteristic for the surface temperature and a cosine angular distribution.

Desorption is of fundamental importance in heterogeneous catalysis. In this regard particularly the desorption of reaction products keeps the catalyst active.

Reaction

Surface reactions can proceed via two types of reaction mechanisms: *Langmuir-Hinshelwood reactions* and *Eley-Rideal reactions*. The *Langmuir-Hinshelwood mechanism* describes the reaction of adsorbates A_{ads} and B_{ads} on the surface, indicated by the reaction scheme: $A_{ads} + B_{ads} \rightarrow AB_{ads}$ [48]. The *Eley-Rideal mechanism* is based on a direct reaction of a gas-phase particle and an adsorbate [49]. Examples of Eley-Rideal reactions are rare [50].

Effects of Supported Particles

Supported particles are inherently different from single crystal surfaces. Particles have a finite size in contrast to the semi-infinite extension of the single crystal surface. Particles can expose different facets in close proximity whereas the single crystal is limited to one facet (neglecting possible high defect densities). Particles have an interface with a support where interactions can take place. The influence of the support and the particle will be discussed separately in the following.

Support Related Effects

- *Surface Rearrangement and Electronic Structure:* The interaction of the particle and the support may result in rearrangement of the highly dispersed supported particles and strong modification of their electronic properties. As a consequence, the adsorption properties and the catalytic behavior of the particles may undergo considerable changes as compared to single crystals. A prominent case is the *strong metal-support interaction* (SMSI), e.g. for Pt particles supported on an Fe_3O_4 film [51].

- *Adsorption and Diffusion on the Support:* Molecules or atoms may adsorb and diffuse on the support. If the adsorption energy on the particle is significantly stronger than on the support, migration leads to an increasing adsorbate density/coverage on the particles. The support surface area contributing to the migration of adsorbates is called *capture zone*. The capture zone effect supported catalysts was first formulated by Gillet and Matolin [52].

- *Reactions on the Support:* For some surface reactions the adsorbates may interact strongly with the support, opening up reaction pathways which are different from that one on the metal particles. Examples of oxide support reactivities are the oxidation of carbon monoxide on a monolayer thin FeO film [53] or the dissociation of methanol on Fe_3O_4/Pt(111) model oxide film [54].

Particle Related Effects

- *Geometric Effects:* Highly dispersed supported particles expose a variety of non-equivalent adsorption and reaction sites, such as e.g. different facets, particle edges, corners, steps or defects, and interface sites at the particle perimeter. The properties of these sites control the kinetics of a catalytic reaction. For example, the adsorbates may occupy preferentially only one type of these non-equivalent sites, as it was shown for example for oxygen adsorption on the alumina supported Pd nanocrystallites [55].

  Some of the reaction steps may take place on specific surface sites, or, more generally, the different surface sites and facets may exhibit different activity and selectivity in the catalytic reaction. The species, preferentially adsorbing on the certain sites, may change the electronic properties and hence the adsorption and reaction behavior of neighboring sites as well.

As already stated before, stress and strain, related to the particles surface-to-volume ratio may affect the interatomic distance of the surface metal atoms causing a change in the overlap of the electronic orbitals and consequently in the electronic structure of the surface [30].

- *Particle Reshaping:* The shape of a supported particle and its stability depends on the interaction strength of the particle and the support. The equilibrium geometric shape of particles is determined by the Wulff rule, stating that the shape is a consequence of minimizing the total surface free energy [56]. The shape of the particles under experimental conditions, where they become covered with adsorbates obeys the same rule. The only difference is that the surface tension is modified by the adsorbate [57]. This can result in a shape transformation, including changes of exposed facets, or even removal and/or creation of the new facets. However, these processes are often kinetically hindered.

- *Electron Confinement:* For metal particles of very small size (~ 40 atoms per particle) the band structure commonly found for bulk material starts to discretize into separate energy levels. The average spacing of the successive quantum levels is denoted by δ, also called the Kubo gap [58]. Since the number of states from the bottom of a valence band to the highest occupied level is equal to the number of electrons, the average spacing is of the order of [59]:

$$\delta = \frac{4E_F}{3N},$$

where E_F is the Fermi energy of the bulk material and N is the number of valence electrons in the particle. The energy levels need to be separated by more than the thermal energy k_BT in order to change the metallic characteristic of the particle:

$$\delta \gg k_BT \approx 25\,\mathrm{meV}, \text{ for } T = 300\,\mathrm{K}\,.$$

The particles are rendered nonmetallic when the energy level spacings become comparable to thermal energy k_BT. Consequently the reactivity and selectivity may be subject to pronounced changes as a function of particle size.

- *Communication effects:* For particles exhibiting different facets, coupling between different sites via surface diffusion may dramatically influence global reaction kinetics [60–62]. With adsorbate coverages close to the adsorption-desorption equilibrium of the adsorbed overlayer, reactant diffusion is usually of minor importance. If the reaction occurs with adsorbate coverages far below these equilibrium conditions, a significant net mass transport of adsorbates may occur.

Part I.

The new UHV Single Crystal Adsorption Microcalorimeter Experiment

3. Background on Experimental Methods

In this chapter the experimental techniques — i.e. single crystal adsorption calorimetry, molecular beams, sticking probability measurements and thermal desorption spectroscopy — are introduced.

3.1. Single Crystal Adsorption Calorimetry

With single crystal adsorption calorimetry the heat of adsorption is measured by detection of the energy deposited upon adsorption and the determination of the number of contributing molecules or atoms. The deposited energy yields a transient temperature rise in the sample detected with an appropriate transducer. In order to determine an accurate value of the deposited energy, it is necessary to have an absolute energy calibration.

3.1.1. General Measurement Scheme

Single crystal adsorption calorimetry requires three important ingredients: (i) a molecular beam source that allows a well-defined pulsing of gas molecules on the timescale of milliseconds, (ii) a heat detector that can be accurately calibrated in energy and (iii) an ultrathin single crystal substrate to maximize the resulting temperature rise.

The necessary scheme of measurements to determine adsorption energies is shown in figure 3.1 and will be briefly explained in the following. First, a directed flux of known molecular intensity is formed in a molecular beam source where the continuous flux is then chopped into pulses. When a pulse arrives at the sample a fraction will be adsorbed on the surface and induces a transient temperature rise due to deposition of the adsorption energy. The transient temperature rise is detected by a heat detector. Simultaneously, the scattered fraction of the gas pulse is detected in a mass spectrometer.

The adsorption signal of the calorimeter is calibrated by substituting the molecular beam by a laser beam of known power, as described first in [23]. For that purpose the laser beam is coupled into the molecular beam source and guided into the same path as the molecular beam, also passing the beam chopper. Thereby, the geometry and timing of the molecular beam pulse and the laser beam pulse are identical. This is important regarding the projection of the beams on the sample surface. The projections of the molecular beam path and the laser beam path on the sample surface must coincide to result in an equal heat transfer to the detector. Only then can the molecular adsorption signal be compared directly to the laser light absorption signal.

If the sample temperature and the molecular beam are not at the same temperature, the detected energy of the gas phase molecule-surface interaction is superimposed with two additional contributions. These originate from (i) temperature equilibration of the molecule with the surface – i.e. equilibration of the inner degrees of freedom – for impinging molecules, either be-

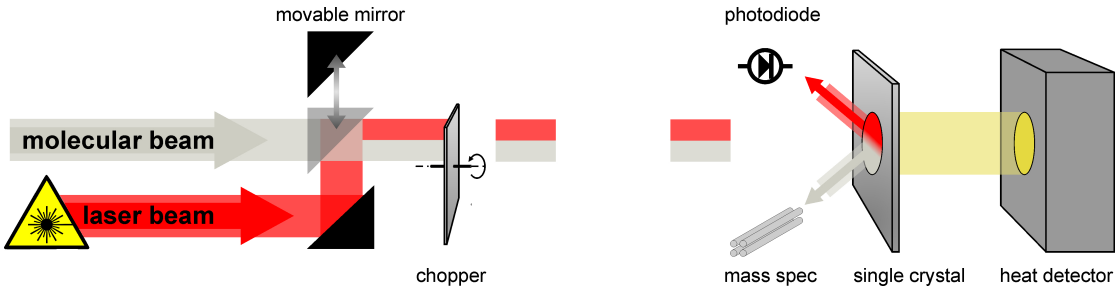

Figure 3.1.: Detection principle of the microcalorimeter experiment. The measurement of the heat of adsorption requires (i) a pulsed molecular beam of known flux and shape, (ii) a heat detector, (iii) a corresponding energy calibration system, here by laser absorption, and (iv) a mass spectrometer to detect the scattered fraction of the gas pulse

ing adsorbed or scattered, and (ii) at least the gas phase molecules' kinetic energy normal to the surface. Typically, the contributions are small compared to the specific energy range of chemisorption, which is $\sim 1\,\mathrm{eV}$ or $\sim 100\,\mathrm{kJ/mol}$.

The fraction of molecules actually adsorbing on the surface during the gas pulse and contributing to the adsorption signal in the calorimeter are derived from a simultaneous sticking probability measurement, which is described in section 3.3. By this method, which was originally proposed by King and Wells [45] the sticking probability can be determined as a function of surface coverage. To obtain the absolute number of adsorbed molecules, an independent quantitative calibration of the molecular beam flux and the pulse length is necessary. If desorption between gas pulses is negligible, the surface coverage can be calculated by summation of the number of adsorbed molecules for each pulse.

In the present case, a pyroelectric heat detector is brought in thermal contact with the sample. The transient temperature rise induced by the deposited adsorption energy generates a surface charge, which can be detected as a voltage signal. An energy calibration is necessary for each new contact of heat detector and sample because of the irreproducible thermal contact. A critical quantity in the determination of the energy response is the reflectivity of the sample surface, setting the absorbance of the laser power. The reflected fraction of the laser power is not measured simultaneously but with a dedicated in situ reflectivity measurement setup, see section 4.2.3.

3.1.2. Existing UHV Adsorption Microcalorimetry Techniques

Adsorption microcalorimetry is not a standard surface science method and the number of experiments is still very limited. Therefore existing adsorption microcalorimetry techniques are reviewed briefly. More details can be found elsewhere [63].

Resistance Calorimetry

Resistance calorimetry is based on the measurement of the temperature dependence of the resistance of a conductive probe. Resistance thermometry can be a very accurate and sensitive

method. It serves as an equipment calibration standard for temperatures between 13.8033 and 1234.93 K [64]. Under special experimental conditions, very high sensitivities can be achieved. Especially for superconductors, the resistance changes strongly with temperature in the vicinity of the phase transition edge [65]. These transition edge sensors are capable of detecting single photons down to 0.3 eV with a resolution of 0.15 eV[66]. Recently, the proof-of-principle to detect the adsorption energy of a single molecule by resistive calorimetry was published, though energy dependent measurements are impeded as yet [67]. Besides transition edge sensors, other experiments tried to maximize their sensitivity by minimizing the heat capacity of their normal conductance measurement setup with the help of microstructure fabrication techniques [68–71], achieving thereby a resolution of down to 0.2 nJ.

An early adaption to UHV adsorption calorimetry was built by Wedler to measure gas adsorption on evaporated polycrystalline thin metal films [72]. Single crystal adsorption calorimetry was pioneered by Kyser and co-workers [73, 74]. Glass coated thermistors were mounted *inside* a Pt(111) single crystal. A serious drawback of this method was a short life-time of the detector (four to six weeks). The authors reported the coverage dependent heat of adsorption for carbon monoxide on Pt(111), for the first time directly measured. Coverages were estimated relative to the saturation coverage by Auger electron spectroscopy (AES), though it is not explained how the Pt(111) was exposed to CO. For a coverage increase $\theta = 0 \rightarrow 0.4$ monolayer, where $\theta = 0.64$ monolayer is specified to be the saturation coverage of CO on Pt(111), the heat of adsorption of (167 ± 42) kJ/mol was reported [73]. Saturating precovered samples with initial coverages of $\theta = 0.45$ monolayer and $\theta = 0.55$ monolayer yielded adsorption heats of (139 ± 12) kJ/mol and (115 ± 5) kJ/mol, respectively [74].

Deformation Calorimetry

Deformation calorimetry relies on the detection of sample deformations induced by temperature changes. Until now, there are two different approaches, which try to exploit these heat induced deformations due to adsorption.

The first method uses the bending of a bimetallic cantilever induced by heat transfer. The bending of the cantilever is detected by the displacement of a laser beam that is reflected on the cantilever surface. Resolutions of ~ 1 pJ were achieved [75–78]. Complications arise from the superposition of deformations by the heat of adsorption and by momentum transfer from impinging molecules, which can make contributions of the same order of magnitude as from the adsorption heat. Recently, the formation energies of tin nanoclusters on a polymer were reported as a function of cluster size using a bimetallic cantilever [79]. However, adsorption energy measurements on single crystal based surfaces have not been reported yet.

The second method uses the deformation of the single crystal itself. The temperature induced expansion of an ultrathin (300 nm) single crystal surface of 4 mm diameter results in the formation of ripples [80]. The extent of these ripples is determined by interferometry. The heat capacity of the ultrathin single crystal is only $10\,\mu$J/K. The resolution was estimated to be 2.1 nJ as an energy calibration was not implemented.

Radiative Calorimetry

Radiative calorimetry takes advantage of the change in emission of blackbody radiation induced by a temperature rise. The change in blackbody radiation is monitored by an infrared detector [24, 81, 82]. To achieve sufficiently large temperature changes, the heat capacity was minimized by using an ultrathin (200 nm) single crystal. Radiative calorimetry was combined with accurate molecular beam techniques, establishing single crystal adsorption calorimetry (SCAC) as an analytical tool for the first time. Accordingly, a careful calibration yields an accuracy of 5% in the estimated heats of adsorption and a detection limit of about 1% of a monolayer, refering to the number of surface atoms. Until today, the method does not allow for measurements below room temperatures due to pronounced reduction of blackbody radiation ($\Delta P \sim T^3 \cdot \Delta T$).

King *et al.* systematically investigated the adsorption energetics for a number of diatomic molecules and hydrocarbons: oxygen, NO, CO, ethylene and acetylene on Ni [83], Pd [84, 85], Rh [86], Fe [87] and Pt [88–90] single crystals of different faces. Also the heat of reaction for CO oxidation on Pt(111) was investigated. Reviews on these results can be found elsewhere [25, 91].

Pyroelectric Calorimetry

Pyroelectric calorimetry is based on the observation of a temperature rise by a pyroelectric detector in thermal contact with the sample. The temperature rise results in the formation of a surface charge, which can be detected as a voltage signal. This detection method provides high sensitivity at low temperatures, making it possible to considerably extend the range of the adsorbates and reaction intermediates probed. Temperature restrictions arise from the material dependent critical temperature of the pyroelectric detector, at which depolarization sets in. Pyroelectric adsorption calorimetry was pioneered by Kovar and co-workers [23, 92, 93] with a $LiTaO_3$ single crystal detector. The sample surface, a polycrystalline thin metal film, was evaporated on the detector. Preceding the application of pyroelectric detectors to adsorption microcalorimetry, the response of pyroelectric detectors were assessed for radiation detection by Simhony *et al.* [94–96], Coufal *et al.* [97–99] and Power *et al.* [100–102] showing linearity in energy, high sensitivity and fast response times. More details on pyroelectric sensors can be found elsewhere [103–105]. The first absolute heat of adsorption using pyroelectric calorimetry was reported by King and co-workers [106]. They used a $LiTaO_3$ detector of 300 μm thickness in thermal contact with a 2 μm thick metal single crystal.

Campbell *et al.* continuously refined this approach in recent years [26, 107–110]. In their detection method the transient temperature rise is measured by a 9 μm thick β-polyvinylidene fluoride (PVDF) pyroelectric ribbon coated on both sides with a metal for electric contacts. A face-to-face voltage is produced upon the heat transfer. The generated voltage is measured by a high impedance amplifier circuit. The advantages of using a β-PVDF ribbon are on the one hand a high flexibility, allowing an easy spring force contact to a single crystal sample, and on the other hand low heat capacity as the PVDF polymer can be processed in thicknesses of several micrometers. The higher sensitivity of the pyroelectric detection method allows for the use of thicker single crystals of 1 to $\sim$ 75 μm. Studies of Campbell *et al.* covered metal adsorption on metal and oxide single crystals [111–116], as well as the adsorption of larger molecules on

metal single crystals, e.g. benzene, naphthalene and cyclohexene on Pt(111) [117–119], thereby gaining insight into metal-carbon bond energies [120] and reaction energies [121, 122].

3.2. Effusive Molecular Beam Sources

A molecular beam is a spatially well defined, highly directed and collision-free flux of molecules [123–125]. Molecular beams are prepared by an expansion of gas from a high pressure reservoir (stagnation stage, typical pressures 10^{-6} to 1 bar) into a lower pressure region. The actual beam is cut out of this expansion by small solid angle apertures. The properties of such beams depend strongly on the pressure (and temperature) in the stagnation stages, and on the dimensions and distances of the components. Two types of beam formation can be distinguished: (i) supersonic expansion, where many collisions happen throughout the beam formation and (ii) effusive expansion, where the number of collisions during the expansion is negligible. The fundamental difference lies in the expansion conditions, which are determined by the ratio of the gas particles' mean free path λ in the gas reservoir and the dimensions of the opening d through which the gas expansion takes place [124]:

$$K_n = \lambda / d \ . \tag{3.1}$$

K_n is known as the Knudsen number. Beams operating at low Knudsen numbers (many collisions: supersonic expansion) and high Knudsen numbers (virtually no collisions: effusive expansion) have different characteristics. In this work, only an effusive beam source is used. Accordingly, the description of molecular beam sources focuses exclusively on effusive beam sources.

Effusive gas expansion occurs if the mean free path λ is larger than the expansion opening with a Knudsen number: $K_n \gg 1$. Under such conditions, the particles will leave the gas reservoir retaining their equilibrium dynamic properties (their velocity, angular and energy distributions). This type of effusion through an opening, and the resulting molecular flux, is known as Knudsen flow. The gas particles can expand through an orifice with diameter d or a channel with a diameter d and a length l. In channels collisions of the particles with the channel walls may occur which affects the angular distribution of the emerging molecular beam. In the extreme of infinitely long channels only particles with momentum solely parallel to the channels's long axis will pass. This effect is called the *tube focusing effect*. The resulting directionality of a molecular beam induced by a channel is quantified by the *peaking factor* κ. The peaking factor is defined as the ratio of the maximum molecular beam intensity I_{max}, in the direction parallel to the centerline axis of the channel and the total intensity of particles effusing out of the molecular beam source I_{total}. For channels, the peaking factor depends on the diameter-to-length ratio $\beta = \frac{d}{l}$ [124]:

$$\kappa = \frac{3}{4}\frac{l}{d} = \frac{3}{4}\frac{1}{\beta}. \tag{3.2}$$

The angular distribution of the effusing gas emerging from a perfect hole (infinite ratio $\beta = d/l$ of diameter d and length l of the hole) would be perfectly cosine.

The optimum collimation of a channel is obtained in the collision-free flow ($K_n \gg 1$). For $K_n \geq 1$, the channel works in a transparent mode, where the centerline intensity is proportional

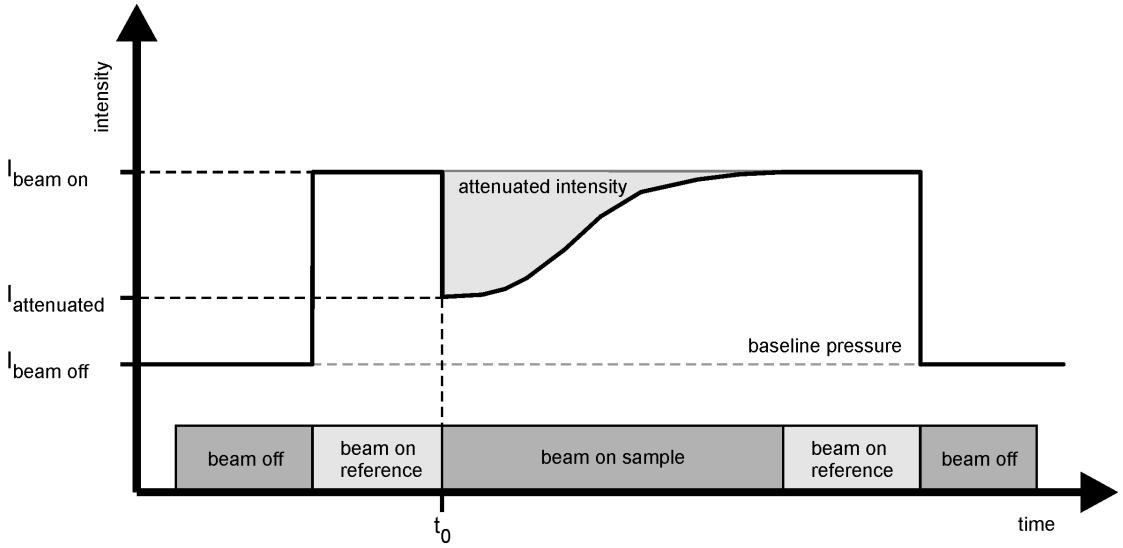

Figure 3.2.: Schematic of a sticking probability measurement

to the source pressure p_0. However, to obtain higher peak intensities, molecular beam sources can be operated at higher pressures than determined by $\lambda \gg d$. At higher pressures, where $K_n \leq 1$, the number of particle-particle collisions becomes as important as the number of collisions with the walls. Under this condition, the channel enters the opaque mode where the centerline intensity is proportional to $\sqrt{p_0}$ [124]. Another approach to increase the intensity is the superposition of the expansions of multiple channels by use of capillary arrays.

3.3. Sticking Probability Measurement

Two methods exist to measure the sticking probability S. The sticking probability is either derived by (i) measurement of the increasing coverage as a function of the exposure or (ii) monitoring the scattered fraction of a molecular beam impinging on the surface.

In the first case, the coverage can be determined by XPS, TDS or work-function measurements, for instance. The sticking probability S is derived from the exposure dependent coverage data by differentiation. The exposure is determined by the pressure and the exposure time. Large errors can be present due to improper calibration or pressure gradients in the chamber. Even with molecular beams, it can be difficult to control the exposure precisely, in small enough increments, if S is high. Therefore, this method often contains great uncertainties but it is the only method for systems where the sticking probability is much less than 1%.

The second method is based on monitoring the quadrupole mass spectrometer (QMS) intensity I_{sca} of the scattered fraction of the molecular beam pulse and compare it to the QMS intensity I_{imp} of the molecular beam pulse which is completely scattered by a non-sticking reference surface , as described in equation 2.16. This method was first described by King and Wells [45].

In the present setup, the sticking probability measurement is based on the King-Wells method [45], which has been adapted to a pulsed molecular beam exposure. The scheme of a stick-

ing probability measurement using the King-Wells method is illustrated in figure 3.2. A gas phase detector, e.g. a mass spectrometer, monitors the partial pressure of the adsorbate's mass. After opening the molecular beam, a continuous flux of molecules impinges on a non-sticking reference in front of the sample. Consequently, the background pressure in the chamber rises from the base pressure to an elevated pressure, corresponding to mass spectrometer signal intensities $I_{beam\ off}$ and $I_{beam\ on}$, respectively. After establishing the constant background pressure $I_{beam\ on}$, the non-sticking reference can be removed from the beam path and the sample becomes exposed to the molecular beam. A fraction of the molecules sticks on the sample, causing a pressure drop in the chamber which attenuates the corresponding mass spectrometer signal intensity $I_{attenuated}(t)$. Based on the observed pressure drop in the chamber, the sticking probability can be calculated as follows:

$$S(t) = 1 - \frac{I_{attenuated}(t) - I_{beam\ off}}{I_{beam\ on} - I_{beam\ off}} \tag{3.3}$$

If the flux of impinging gas-phase particles is known, the amount of adsorbed particles can be calculated, provided that desorption at this coverage, temperature and pressure conditions is negligible:

$$\theta(t) = \theta(t - \Delta t) + S(t) \cdot (\phi \cdot \Delta t), \tag{3.4}$$

where $\theta(t)$ is the accumulated coverage, ϕ the incoming molecular flux per time and consequently $(\phi \cdot \Delta t)$ the number of impinging molecules in the time interval Δt. If Δt is small, the sticking probability $S(t)$ can be assumed to be essentially constant over the exposure. The initial condition of the surface coverage $\theta(t_0)$ needs to be known. Typically $\theta(t_0) \approx 0$ as the sample is commonly cleaned prior to experiments.

Implications of a pulsed Molecular Beam

In the originally developed King-Wells-method a continuous flux of molecules onto the surface is applied. Since a pulsed molecular beam needs to be used for energy measurements, the classical King-Wells method was modified to determine the sticking probability in discrete steps. Consequently the sticking probability is not determined as a continuous function of time $S(t)$ but as a discrete function in dependence of the pulse number i:

$$S(t) \rightarrow S_i$$

Also the coverage becomes a function of the pulse number i:

$$\theta(t) \rightarrow \theta_i$$

Besides the discretization, equations 3.3 and 3.4 hold, where $I_{attenuated}(t) \rightarrow I_{attenuated,i}$.

Pulsing a molecular beam onto a surface results in temporary local pressure changes. By using a molecular beam, a local pressure on the order of 10^{-6} mbar can be generated on the sample. Consequently, a pressure variation of over four orders of magnitude takes place between the pulses, on the time scale of milliseconds. At high coverages, this pressure variation may result in desorption of molecules between pulses due to the fact that the saturation coverage can considerably vary as a function of pressure. Experimentally, e.g. for CO adsorption on

transition metal surfaces, a finite sticking probability can be observed for all coverages. Instead of saturating the surface, a steady state is established in which the adsorption during a gas pulse exactly balances the desorption between gas pulses, leading to an apparent infinite uptake of gas onto the surface in a quasi-saturation regime. Similar adsorption-desorption behavior in the quasi-saturation regime was previously observed in microcalorimetric studies on CO adsorption carried out on Pd, Pt and Ni single crystal surface [25].

3.4. Thermal Desorption Spectroscopy

Reversible adsorption of molecules on a surface can be studied by thermal desorption spectroscopy (TDS), also known as temperature programmed desorption (TPD). In TDS experiments, the sample is exposed to a gas in order to build up a defined surface coverage. Subsequently, the sample is heated, while the desorbing species are monitored by a mass spectrometer. TDS is one of the most commonly used surface science techniques to investigate gas-surface interactions.

The adsorption energy is determined indirectly, since the reverse process is actually monitored. In the Wigner-Polanyi model, it is assumed that the rate of desorption $r(\theta)$,where θ is the coverage, of a species from the surface is given by equation 2.12:

$$r(\theta) = \frac{\mathrm{d}\theta}{\mathrm{d}t} = \nu(\theta)\theta^n \exp\left(-\frac{E_{des}}{RT}\right),$$

where ν is the frequency factor, n is the order of desorption, R the gas constant, T the temperature and E_{des} is the desorption activation energy.

In general, the desorption order n is not known, and ν, E_{des} and n can all be a function of the surface coverage θ. This lack of knowledge is one of the main limitations in quantitative analysis of TDS data. However, the energetics of desorption can be estimated by different analysis methods [38–41, 126].

Three ideal cases of $n = 0, 1, 2$ can be distinguished, i.e. zero-order, first-order and second-order desorption. It should be mentioned here that in general the desorption order is not limited to integers:

- Zero-order desorption takes place if the desorption rate does not depend on the coverage. The spectra are typically asymmetric, and all show the onset of the desorption signal, the leading edge, at the same temperature. while the temperature of maximum desorption shifts to higher values with increasing initial coverage.

- First-order desorption spectra have symmetric line shapes, the peak temperature of which is independent of the initial coverage. According to Redhead [39], E_{des} can be calculated by:

$$E_{des} = RT_{max}\left(ln\left(\frac{\nu T_{max}}{\beta}\right) - 3.64\right) \tag{3.5}$$

  where β is the gradient of the linear heating ramp, R is the gas constant, and T_{max} is the temperature of the desorption peak.

- Second-order desorption is typical for associative desorption, which is the reverse process of dissociative adsorption. In this case, the peaks are symmetric, and the temperature at maximum desorption shifts to lower values with increasing initial coverage. Habenschaden and KÃ$\frac{1}{4}$ppers established leading-edge analysis for this case [40].

TDS spectra can be complex, with multiple peaks due to lateral interactions, phase transitions and different adsorption sites leading to different kinetic processes during desorption. Additionally, the desorption peaks may broaden due to diffusion on the surface.

Quantitative comparison of TDS data obtained by different setups may not be straight forward. Errors in the TDS spectra can be introduced either by not well defined surface states or the experimental conditions. The main issues regarding the experimental setup are:

- temperature inhomogeneity on the sample surface and the related position of the temperature probe,
- inaccuracy of the temperature probe,
- accumulation of desorbed molecules in the background gas, which is connected to the pumping speed of the UHV chamber,
- and imperfection of the linear heating ramp.

These possible sources of error should be kept in mind when comparing TDS data acquired by different experiments. Mismatches of data, e.g. temperature shifts, may result not only from different surface properties (contaminations, defect density, etc.) but also from the specific experimental conditions.

4. Experimental Setup

The experimental setup and its important details are concisely described in this chapter. The construction and calibration of the microcalorimeter experiment is a substantial part of this work.

In order to link the detailed knowledge of the structural properties of the catalyst to the energetics of the gas-surface interaction, a new microcalorimetric experiment was set up, combining the pyroelectric detection of adsorption and reaction heats with the capability to prepare well-defined supported model catalysts. Additionally, temperature-programmed desorption spectroscopy was integrated to compare the direct measurement of adsorption/reaction energies with the energetics of reverse desorption processes. The specific requirements are the following:

- *Sample preparation and characterization:* The tools for preparation and characterization of a variety of model supported catalysts have to be integrated. Particularly, the possibility to deposit several metals to prepare different metal oxides and/or metal nanoparticles is required. A sample transfer from the preparation chamber into the microcalorimetry detector should be provided.

- *In-situ reflectivity measurement:* The reflectivity of the sample is a crucial parameter for the calibration of the absolute value of deposited energy in this kind of setup. A method for in-situ measuring the reflectivity of the model supported catalysts prepared under well-defined ultra high vacuum (UHV) conditions has to be integrated.

- *Pulsed molecular beam:* The beam source should allow one to vary the beam flux over the largest possible range. The molecular beam must be well-collimated and pulsed with a variable modulation frequency. The pulsed molecular beam must be produced in a way that generates only low intensity vibrations in the UHV chamber since the pyroelectric heat detector possesses a high piezoelectric coefficient and hence is very sensitive to mechanical vibrations. The beam must be suitable for using a large variety of gases: both 'light' gases with high vapor pressure like CO or ethylene used in the studies of King et al. [86, 91], see section 3.1.2, as well as for large molecules with low vapor pressure ($> 10^{-2}$ mbar) like benzene applied in the experimental setup of Campbell *et al.* [117]. For more complex experiments requiring exposure to several reactants it is necessary to provide a possibility to dose more than one reactant via the molecular beam.

- *Variable temperature:* Microcalorimetric detection of adsorption heats has to be realized in a temperature range from 100 to 300 K, which requires high thermal stability on the time scale of hundreds of minutes.

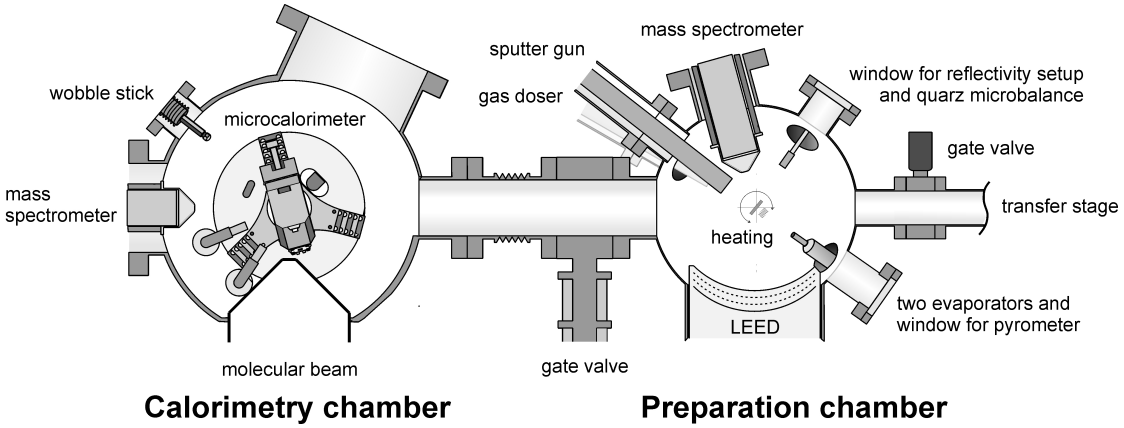

Figure 4.1.: Schematic of the microcalorimetry experiment

- *Vibration damping:* High sensitivity of the pyroelectric detector to the mechanical vibrations requires the best possible vibrational isolation of the microcalorimeter from the UHV chamber.

- *In-situ calibration:* Detectors to determine the absolute values of beam fluxes and absolute adsorption/reaction enthalpies must include (i) a beam monitor for measuring the absolute molecular beam flux and (ii) a photodiode for in-situ determination of the laser power which is crucial for the energy calibration. It should be possible to place all detectors at the same position with respect to the molecular beam to reduce systematic errors.

- *Samples:* The combination of direct energy measurement by microcalorimetry with temperature programmed desorption requires integration of two different samples. Single crystals of $1\,\mu$m thickness are used for microcalorimetric measurements. But it is difficult to achieve a constant uniform heating ramp for ultrathin samples. Therefore a second kind of sample of about 1 mm thickness has to be integrated on the manipulator to enable temperature programmed spectroscopy.

In the following, the new single crystal adsorption calorimetry setup is described. It allows the direct measurement of gas-phase adsorption and reaction enthalpies on well-defined supported model catalysts and thin oxide films. Based on the previously developed highly sensitive pyroelectric detector, the heat input to the sample is detected by a pyroelectric β-PVDF ribbon pressed against the back of the ultrathin single crystal. Figure 4.1 shows the UHV system, which is divided into two separate chambers:

- The preparation chamber contains all necessary tools for the preparation of various types of oxide films, which are grown on single crystal surfaces, as well as for deposition of the desired metals to form supported nanoparticles. The preparation can be carried out with two types of samples: (i) an ultrathin single crystal ($\sim 1\,\mu$m) for the microcalorimetric measurements and (ii) a thicker single crystal (~ 1 mm) for TDS experiments. An in-situ reflectivity measurement setup is additionally integrated into the preparation chamber which is necessary for the accurate quantitative calibration of the measured energies.

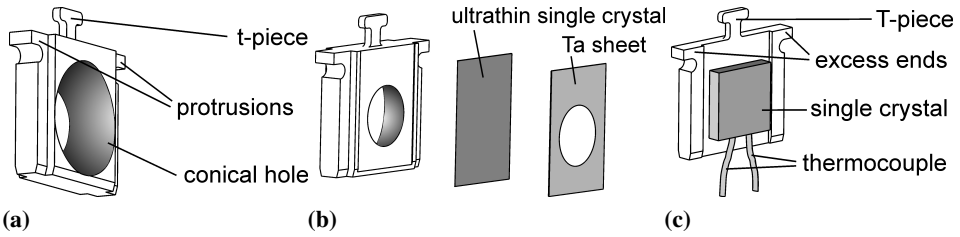

Figure 4.2.: Sample holders for (a,b) 1 μm and (c) 1 mm thick samples: (a) Backside view of the Mo sample holder; (b) Explosion view of the front side if the sample holder, sample and a Ta sheet; (c) Front view of the Mo sample holder and a 1 mm thick sample

- The calorimetry chamber contains a differentially pumped effusive molecular beam source, which can be chopped with variable frequency and provides modulation of the flux intensities. The sample and the heat detector can be cooled down by liquid nitrogen or pre-cooled Ar, enabling temperature variation between 100 and 300 K. Long-term temperature stability is reached on a time scale of several hours. For reduction of acoustic noise, which is inherent to the PVDF ribbon, the heat detector is mechanically decoupled and vibrationally isolated from the UHV chamber. In-situ calibration tools – a beam monitor for determining the absolute fluxes of the gas-phase molecules and a photodiode for measuring the laser light intensity – are additionally integrated into the chamber. All three types of detectors – the heat detector, the beam monitor and the photodiode – are mounted on a rotatable differentially pumped platform, which enables their precise positioning at the very same place with respect to the molecular beam and thus reduces the systematic errors. The gas-phase detection is realized by a non-differentially pumped quadrupole mass spectrometer.

The microcalorimetry machine also contains a third independent UHV section: a sample transfer stage. The transfer stage has sample holder mounts for three sample holders and is described in section 4.1. The sample holders can be moved from chamber to chamber by a transfer rod or stored in the transfer stage section, which can be separated by a gate valve. To introduce new samples into the UHV system, the transfer stage section incorporates additional flanges giving access to the sample holder mounts. Therefore the transfer stage section serves also as a convenient load-lock.

4.1. Samples and Transfer Stage

In the microcalorimetry experiment ultrathin samples are used which have to be transfered back and forth from the preparation chamber to the calorimetry chamber. Additionally, thicker single crystals are needed for reflectivity measurements and TDS experiments. Metal single crystals, either ultrathin ($\sim 1\,\mu$m) or ~ 1 mm thick, are mounted to molybdenum sample holders, with dimensions of 18×16 mm. Figure 4.2a shows the backside of a bare Mo sample holder. Figure 4.2b shows an explosion view of the corresponding front side of the Mo sample with an

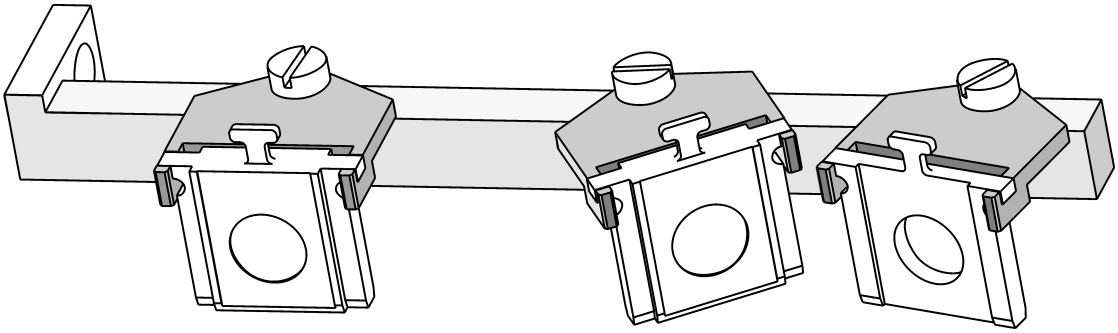

Figure 4.3.: Schematic representation of the transfer stage's three fork-like sample holder mounts, with sample holders

ultrathin sample and a Ta sheet present. The 50 μm thick tantalum sheet (12×16.5 mm) with a central hole of 8 mm diameter is used to mount the ultrathin sample to the sample holder. For the thick sample, thermocouple wires, type K, are spot welded to the crystal edge. In figure 4.2c the central hole in the molybdenum sample holder, not visible for the thick crystal, gives access to the back side of the sample for direct heating by electron bombardment. The central hole is conical for the sample holders of the ultrathin samples, which allows self-aligning contact with the calorimeter. The actual alignment will be explained later in section 4.3.1. The Mo sample holders feature a T-piece on the top. The T-piece enables the handling of the sample holders in the UHV chambers by wobble sticks (not shown). The wobble sticks are equipped with corresponding grippers. The sample holders exhibit diminutions on each side. These diminutions fit into corresponding guides of the sample holder mounts in the preparation and calorimetry chambers, described in section 4.2.1 and 4.3, respectively. The sample holders have protrusions on the sides of their upper edge. These protrusions match to the recesses of fork-like sample holder mounts in the transfer stage. Figure 4.3 shows the three sample holder mounts which are attached to a transfer rod (VAb GmbH) of 80 cm travel length. The sample holders hang on their protrusions in the fork-like sample holder mounts. The sample holder mounts have a limited rotation. Thereby the sample holders can be accessed from different angles with respect to the transfer stage, which is necessary as the wobble sticks approach the sample holder mounts from different angles in the preparation and microcalorimetry chambers. The transfer stage section is pumped by a 50 L/s turbo molecular pump (TMP) (Pfeiffer, TMH/U 071) and can be separated from the preparation chamber by a gate valve. Therefore it can be used as a load-lock.

4.2. Preparation Chamber

The preparation chamber (Tectra) is equipped with the experimental tools which are necessary for the preparation of oxide film supported metal nanoparticles on ultrathin ($\sim 1\,\mu$m) samples and thick (~ 1 mm) samples.

The preparation chamber is pumped by a 500 L/s turbo molecular pump (TMP) (Pfeiffer, TMU 521 P) and operates at a base pressure in the low 10^{-10} mbar range. Figure 4.1 shows the geometry of the preparation chamber and its equipment, namely a sputter gun (Omicron,

ISE-10), an electron bombardment heating, two metal evaporators (Omicron, EFM 3) along with a quartz microbalance (Sigma Instruments) for evaporation flux calibration, a combined LEED/Auger electron spectroscopy (AES) unit (SPECS, ErLEED) and a quadrupole mass spectrometer (QMS) (Hiden, Halo 201). The ionizer region of the QMS is shielded by a gold coated aperture with an opening of 4 mm for TDS studies. A gas doser is present, consisting of a 30 cm long tube fixed on a translation stage with a 10 μm opening to the gas supply system described in section 4.2.4. The gas doser can be used to locally expose the surface to gas-phase molecules without strongly increasing the background pressure in the chamber, e.g. for CO saturation of the surface. The sample is positioned with a rotatable xyz-manipulator (VAb GmbH) . The samples can be heated up to 1200 K by electron bombardment and cooled to $\sim$ 100 K by liquid nitrogen. Further, a pyrometer (Sensortherm, MP 25) is mounted at a viewport outside the chamber to facilitate a noncontact temperature measurements, which is necessary for the ultrathin sample. Details on the calibration of the pyrometer to metal surfaces are given in section 4.2.2. To characterize the samples, two additional methods are used besides LEED and AES: (i) temperature desorption spectroscopy (TDS), using the QMS and a computer controlled linear heating ramp, and (ii) an in situ reflectivity measurement setup, which is described separately in section 4.2.3. Details on standard surface science techniques can be found elsewhere [127–130].

4.2.1. Manipulator

The manipulator allows (i) positioning the sample with respect to the preparation tools mounted to the chamber, (ii) temperature control, and (iii) application of a bias voltage to the sample holder mount. The manipulator is mounted vertically and consists of a long cylinder with three translational degrees of freedom and a rotational degree of freedom around the cylinder's centerline. The rotational feedthrough of the manipulator is differentially pumped. Figure 4.4 shows the front and backside of the lower end of the cylinder where two electrically isolated sample holder mounts and a heating filament are installed. Each sample holder mount consist of two guides corresponding to the diminutions of the sample holders. Sample holders can be inserted in the sample holder mounts by a wobble stick. Tantalum springs are present in the guides to press the sample holder to the mount. Thereby the thermal contact is improved, which would otherwise suffer from the required production tolerance of the parts. The sample holder mounts are electrically isolated by sapphire plates allowing to apply a bias voltage for electron bombardment heating and evaporation. The upper sample holder mount incorporates a filament for sample heating by electron bombardment, by which the sample can be heated up to 1200 K. A reservoir inside the manipulator, which can be filled with liquid nitrogen, allows cooling of the sample down to $\sim$ 100 K. Sliding thermocouple connectors, type K, are present below each mounting site to contact the thermocouple wires of the $\sim$ 1 mm samples. The manipulator also holds a revolver with five dielectric mirrors (not present in figure 4.4) for calibration of the in situ reflectivity measurement setup, see section 4.2.3.

4.2.2. Pyrometer

The temperature of the ultrathin single crystals can be monitored by a noncontact method. The use of a thermocouple is not possible as the mounting of a contact probe would destroy the

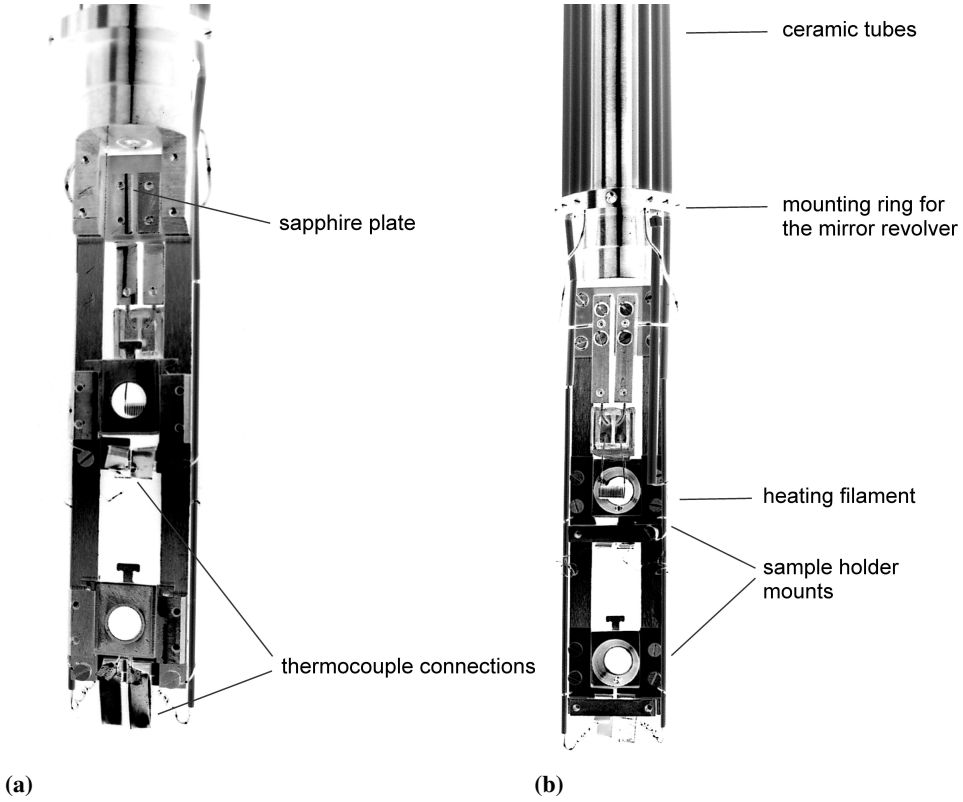

Figure 4.4.: The two sample holder mounts at the lower end of the manipulator; (a) front view, (b) rear view

ultrathin sample. Therefore, a pyrometer (Sensortherm, MP25) is used. Changes in the sample's blackbody radiation are detected in the spectral range in wavelength of 2.0 to 2.8 μm. A lens focuses the radiation at distances of 19 to 43 cm. The detection area at the sample position is variable between 1.0 to 2.3 mm The pyrometer output is a current of $0-20$ mA, which is recorded by an analog-to-digital converter via the voltage drop over a shunt of 500 Ω. A correct temperature estimation requires knowledge of the emissivity of the surface. For metals, the already low emissivity is also a temperature dependent property [131]. Unfortunately, the pyrometer only provides the option of a fixed emissivity for the measurement. To circumvent this limitation, the output of the pyrometer was calibrated by use of a $\sim$ 1 mm thick Pt(111) sample with a type K thermocouple connection. Figure 4.5a shows the thermocouple temperature as a function of the pyrometer response. The curve relates the pyrometer output to the sample temperature. Biasing contributions in the estimated pyrometer temperature originate from the irradiation of the bright heating filament. The contribution of the heating filament was assessed by variation of the filament current, resulting in a variation of the emitted radiation. Seven different filament currents between 2 and 6 A were evaluated. Firstly, the sample was heated to $\sim$ 1200 K. Then, the corresponding filament current was adjusted, resulting in a temperature drift. To enable temperature drifts also at high filament currents, the acceleration voltage of the

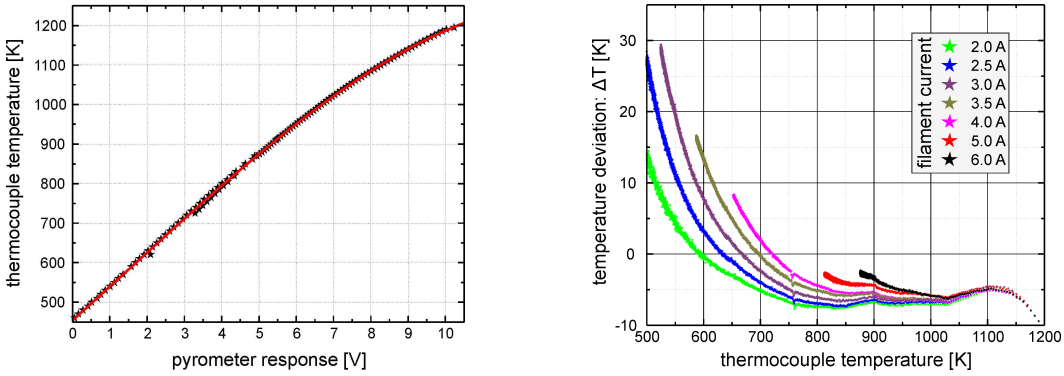

(a) **(b)**

Figure 4.5.: (a) Calibration curves for the pyrometer, using a Pt(111) surface and a thermocouple; (b) Contribution of the filament emission to the temperature measured with the pyrometer $T_{pyrometer}$ as a function of the more reliable thermocouple temperature $T_{thermocouple}$; The temperature deviation in the pyrometer temperature is displayed as the difference of these temperatures: $\Delta T = T_{pyrometer} - T_{thermocouple}$; the bias of the pyrometer temperature of the filament irradiation increases with increasing filament current.

electrons was switched off. The deviation ΔT of the pyrometer temperature $T_{pyrometer}$ and the thermocouple temperature $T_{thermocouple}$ was monitored as a function of the thermocouple temperature. The temperature deviation is defined as $\Delta T = T_{pyrometer} - T_{thermocouple}$. Figure 4.5b shows the corresponding deviations ΔT for different filament currents. At high temperature, above $600 - 800\,\mathrm{K}$, the difference is negative for all filament currents. At lower temperatures the difference is positive. An increase of the filament current shifts the onset of positive temperature differences to higher thermocouple temperatures. The temperature drift exhibits a cut-off at low temperature due to the remaining heating power of the filament. The negative difference at high temperatures evidences that the pyrometer calibration curve underestimates the sample temperature by $\sim 7\,\mathrm{K}$ with respect to the thermocouple temperature. The filament current dependency of the onset of positive temperature differences indicates that the detected blackbody radiation from the sample is increasingly dominated by the radiation of the heating filament present in the background, especially obvious at lower temperatures. Rotation of the manipulator by 5° changes the pyrometer temperature reading by 5 to 10 K. This change most likely originates from variation of the amount of background radiation deflected into the pyrometer's beam path.

4.2.3. In situ Reflectivity Measurement Setup

Accurate characterization of the reflectivity of the sample surfaces plays a crucial role in the energy calibration of the calorimeter by laser absorption. The setup enables measurement of the regular reflectivity of sample surfaces in UHV at a wavelength of $\lambda = 632.8\,\mathrm{nm}$. Figure 4.6 shows a schematic drawing of the in situ reflectivity measurement setup (figure 4.6a) and a

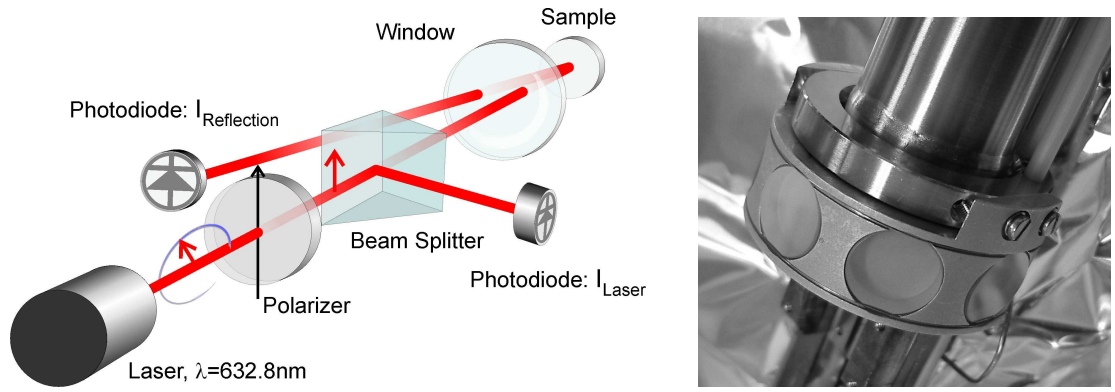

Figure 4.6.: The in situ reflectivity measurement setup. Shown is (a) a schematic of the setup and (b) the mirror revolver for calibration, which is attached to the mounting ring (figure 4.4), containing five dielectric mirrors of different reflectivities

picture of the mirror revolver attached to the manipulator(figure 4.6b).

A Helium-Neon laser (Lasos, 632.8 nm, 2 mW, cw) is mounted to a window pointing to the center of the chamber. After passing a polarization filter the laser beam is divided into two separate beams by a beam splitter (Linos). An adjacent photodiode (Silicon Sensor, PS95-4) monitors the laser power I_{Laser} and its fluctuations in one of the two laser beams. The laser beam is incident on the sample surface at an angle of about 5Â° relative to the surface normal. The reflected intensity $I_{Reflection}$ is measured by a second photodiode (Silicon Sensor, PS100-2). Monitoring of the laser power is necessary to account for possible fluctuations. Figure 4.7 shows the typical output behavior of the He-Ne laser. The initial longterm drift is a consequence of the warm-up of the lasing medium and the mirror alignment; the short term variations are caused by mode sweeping. To compensate these fluctuations in the analysis, these variations have to be taken into account. A polarization filter is necessary due to the fact that the laser is not stable

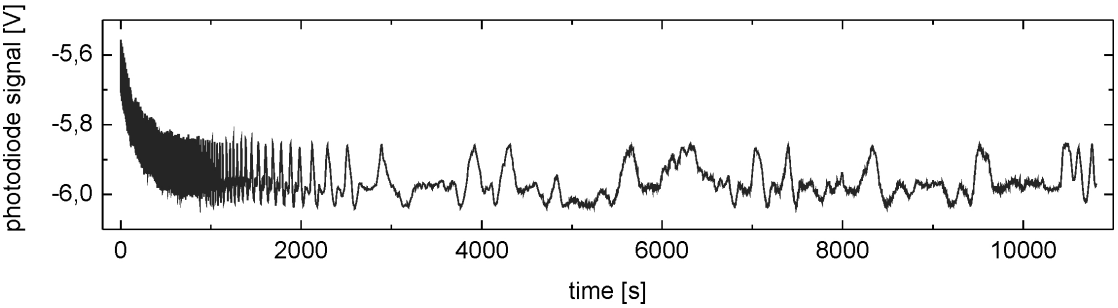

Figure 4.7.: Laser fluctuations during warm up; the longterm drift is a consequence of lasing medium issues and mirror alignment; the short term variations are caused by mode sweeping

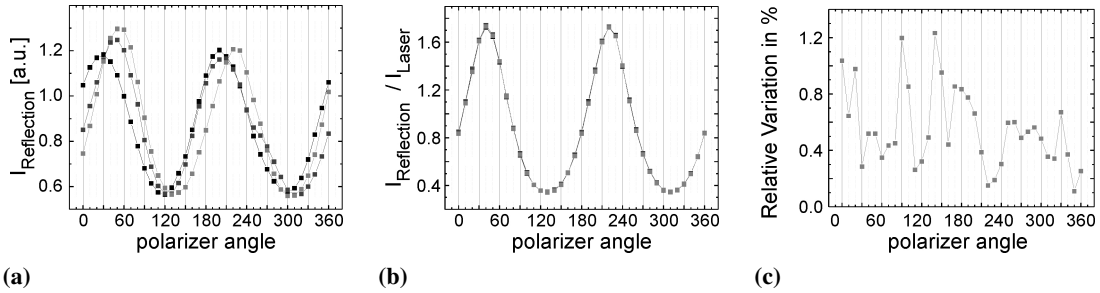

Figure 4.8.: As a function of polarizer angle is shown (a) the intensity of reflected light $I_{Reflection}$, (b) the intensity ratio of reflected laser power $I_{Reflection}$ and the monitored laser power I_{Laser} and (c) the relative variation of the intensity ratio: $\sigma_{I_{Reflection}/I_{Laser}}/\mu_{I_{Reflection}/I_{Laser}}$, where $\sigma_{I_{Reflection}/I_{Laser}}$ is the standard deviation and $\mu_{I_{Reflection}/I_{Laser}}$ is the mean of three independent measurements.

in its *random* polarization and that the implemented beam splitter has a polarization dependent transmission, $T_s \sim 35\%$ and $T_p \sim 65\%$ at 632.8 nm. The polarization filter fixes the polarization to a defined orientation with respect to the beam splitter. A possible relative polarization effect of the polarizer to the beam splitter was evaluated.

Figure 4.8a shows three independent measurements of $I_{Reflection}$ as a function of the polarizer angle relative to the beam splitter. An oscillation with the relative angle is present for all data sets. Further, phase shifts and amplitudes are obvious. Figure 4.8b shows the ratio $I_{Reflection}/I_{Laser}$ as a function of polarizer angle for the same three measurements. The intensity ratio is evidently compatible for all three measurements with respect to the polarizer angle. Phase shifts and amplitude variations are compensated by the laser power intensity I_{Laser}. Figure 4.8c shows the ratio of the standard deviation and the mean as a function of the polarizer angle. The relative variation of the intensity ratio features random fluctuations up to 1.2%. Therefore the intensity ratio is an appropriate parameter to estimate reflectivities being not significantly affected by fluctuations of laser power or polarization. The precision of a single reflectivity measurement is about 1%. For a better reflectivity estimation it is necessary to collect statistics. It has to be noted, that a substantial contribution to the variation of the intensity ratio originates most likely from changes in the alignment of different components. For calibration five dielectric mirrors (LayerTec) of known reflectivities (nominal: 40%, 60%, 75%, 85% and 97%) are mounted to the manipulator , see figure 4.6b. See chapter 5.2.2 for more details on the calibration of the in situ reflectivity measurement setup.

4.2.4. Gas Supply System

The gas supply system connects gas bottles to all devices of the preparation chamber and of the calorimeter chamber. Figure 4.9 shows a schematic of the gas supply system. Its design enables easy handling without the necessity to exchange gas bottles. Gas bottles can be attached to a

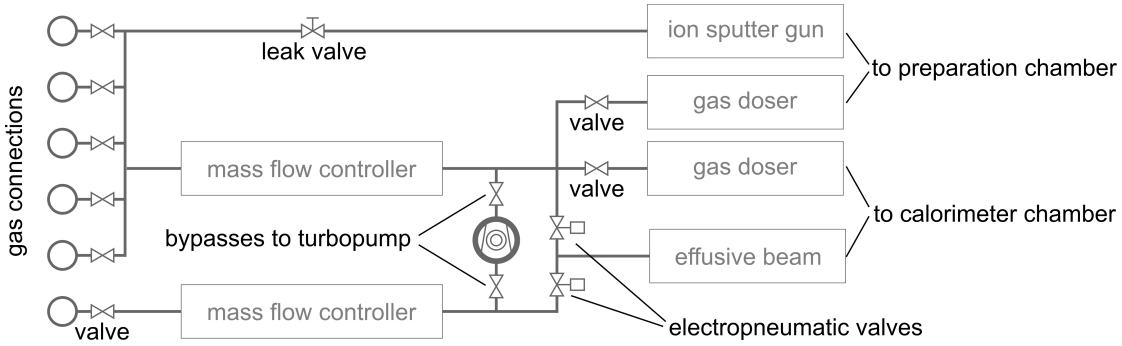

Figure 4.9.: Schematic of the gas supply system; for clarity the roughing pump lines are omitted

set of *swagelok* connections. Each connection has a separate valve to the gas system and to the roughing pump. Thereby the gas line can be cleaned from other residual gases before introducing a new gas. Each mass flow controller consists of an upstream flow control valve (MKS, 248 A, maximum flow rate of 10 sccm nitrogen), a capacitance manometer (MKS, Baratron 122) and a pressure controller (MKS, Type 250).

4.3. Calorimetry Chamber

The calorimetry chamber is designed for microcalorimetry measurements and sticking probability measurements. The chamber (Tectra) is pumped by a $500\,\mathrm{L/s}$ TMP (Pfeiffer, TMU 521 P) resulting in a base pressure of $\sim 2 \cdot 10^{-10}$ mbar.

Figure 4.10 shows an overview of the experimental arrangement. It includes a high-flux effusive molecular beam (1) with an integrated chopper and the tools for calibration purposes (for details see section 4.3.3 and 4.3.4). A differentially pumped rotatable platform (2) mounted in the center of the chamber carries three types of detectors: a microcalorimeter (3) for the measurement of adsorption/reaction heats, a UHV-compatible photodiode (4) for in-situ determinatoin of the absolute laser intensity and a beam monitor (5) for the measurement of the absolute molecular beam fluxes.

The microcalorimeter consists of two main parts: a sample holder mount (6) and a detector head (7), both mounted on a copper platform (8) (for further details on the microcalorimeter setup see section 4.3.1). The position of the sample holder mount (6) is fixed on the copper platform, the movable detector head (7) can slide along in order to approach the sample positioned in the sample holder mount (6) of the calorimeter and establish a thermal contact to the thin single crystal. In the working position the sample holder mount (6) with an inserted thin single crystal sample is placed in front of the molecular beam aperture (9) at a distance of 4 mm. The detector head (7) can be moved and pressed toward the sample by using a rotatable Allen wrench on a wobble stick (10) and a translation screw (11) mounted into the on the back side of the detector head. After the contact with the sample is established, the wobble stick (10) can be removed from the detector head, so that the entire calorimeter becomes mechanically decoupled from the chamber and remains only connected to the vibration damping stack (12) installed on the rotatable platform (2). The Cu platform and the entire microcalorimeter can be cooled down

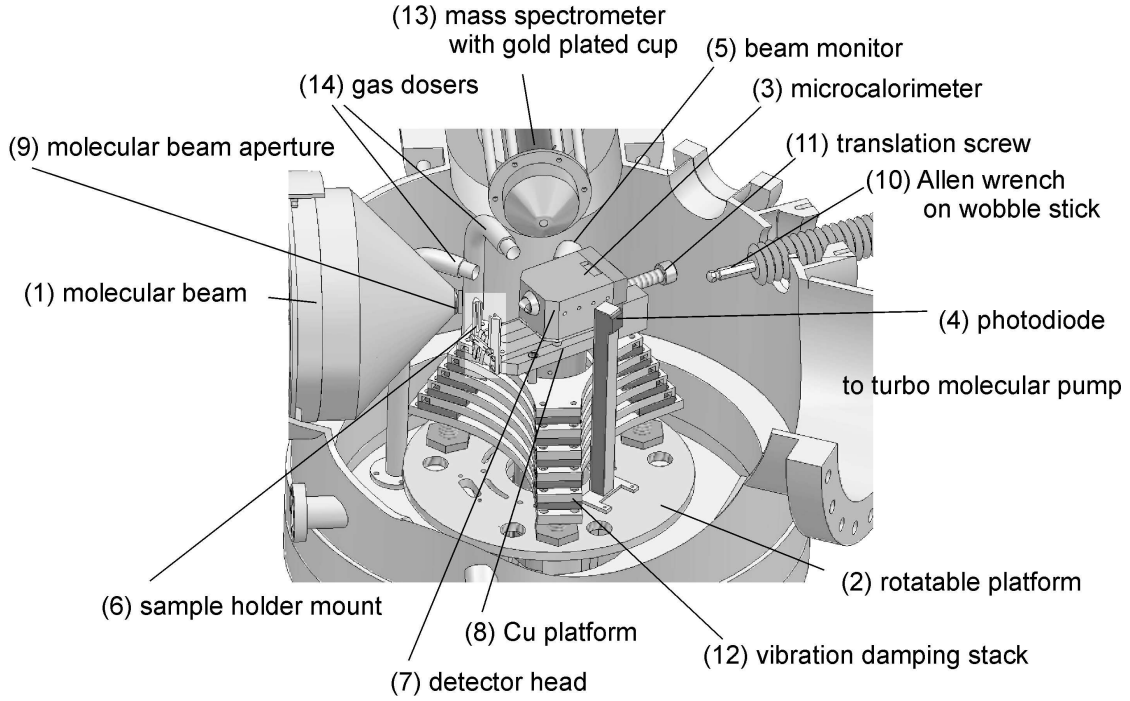

Figure 4.10.: Overview of the calorimetry chamber; a more detailed schematic of the calorimeter is shown in figure 4.12.

with liquid nitrogen or with a cooled gas to cryogenic temperatures. Prior to beginning of the measurement, the sample has to be shielded from the molecular beam to get a reference signal in the mass spectrometer for the sticking probability analysis. For this purpose, a gold flag (not shown in figure 4.10) can be positioned between the sample and the molecular beam aperture (9). For the measurement of the molecular beam flux and the laser intensity calibration the rotatable platform (2) can be rotated to bring the corresponding detectors - the beam monitor (5) and the photodiode (4) - in front of the molecular beam at a distance of 4 mm. This position is exactly the same as the position of the sample during the microcalorimetric measurement. Since only one coordinate - the rotation angle of the rotatable platform (2) - is varied to reach the working position, this procedure allows minimization of the systematic errors, which might otherwise occur due to misalignments of different types of detectors. For the sticking coefficient and reactivity measurements, a QMS (Hiden, HAL 301/3F PIC) (13) is integrated into the chamber and equipped with a gold plated aperture. Two gas dosers (14) are available, which allow to supply additional gas-phase particles to the chamber independently from the molecular beam source.

After the preparation the sample is transferred into the calorimetry chamber by the transfer stage and can be fixed either in the microcalorimeter or on a manipulator placed in the center of the chamber. The manipulator has one rotational and three translational degrees of freedom (the manipulator is not shown in figure 4.10) and contains a sample holder mounting with an electron bombardment heating as well as a separate filament which can be used for sample heating in the sample holder mount.

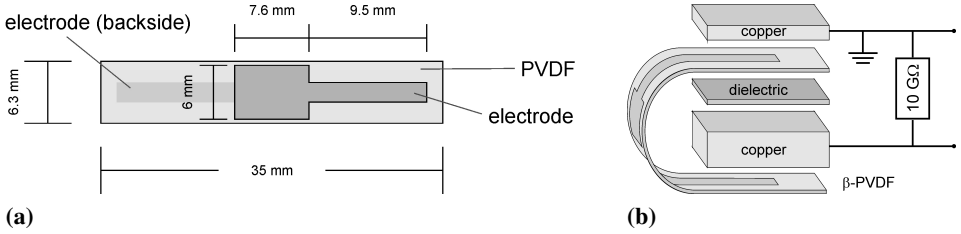

Figure 4.11.: (a) Typical dimensions of the PVDF ribbon, either $9\,\mu$m or $6\,\mu$m thick, partially covered with metal electrodes, either Al or Au/Cr; (b) Ribbon mounting and electrical connection to high impedance amplifier

4.3.1. Microcalorimeter

In this section, the microcalorimeter will be described. Details are given on the processing of the pyroelectric detector ribbon, its mounting and electrical connection, the according electronic signal processing, the temperature stability and control as well as details on the vibration damping.

The Pyroelectric β-PVDF Ribbon Detector

In the present microcalorimeter, a pyroelectric heat detector is used. The sensing element is a β-PVDF ribbon (Goodfellow: $9\,\mu$m, Al electrodes or Piezotech: $6\,\mu$m, Au/Cr electrodes) with metalized surfaces.

The electrodes are partially etched away where they will not contact the ultrathin sample. This procedure optimizes the sensitive area of the detector to the region of interest, reducing the noise contribution and enhancing the sensitivity. Another benefit is that the etching reduces the electric capacitance. Consequently, an induced surface charge yields a higher voltage pulse. The procedure of Al etching was described elsewhere [110] and is summarized here shortly.

The ribbon is painted on both sides with nail polish to create masked areas of the ribbon where the metal electrode is desired. The typical dimensions of the ribbon and the electrodes are shown in figure 4.11a. The aluminum is etched away by immersing the ribbon in 0.4 molar aqueous KOH solution and applying a bias of 5 V with respect to a reference electrode, whereas the gold/chromium electrode is etched by immersion in *aqua regia*. The partially etched ribbon is sandwiched between copper blocks along with isolating dielectric sheets to prevent short cuts. Figure 4.11b shows a schematic of the ribbon mounting and the according electric connection to the high impedance amplifier.

The Microcalorimeter

Figure 4.12 shows a schematic of the microcalorimeter integrated into this experimental setup. The pyroelectric β-PVDF ribbon (1) is mounted into a detector housing (2), such that the ribbon forms a protruding 180° arch, and is electrically connected to an amplifier circuit. In the following, the assembly of the ribbon (1) and the detector housing (2) will be denoted as the

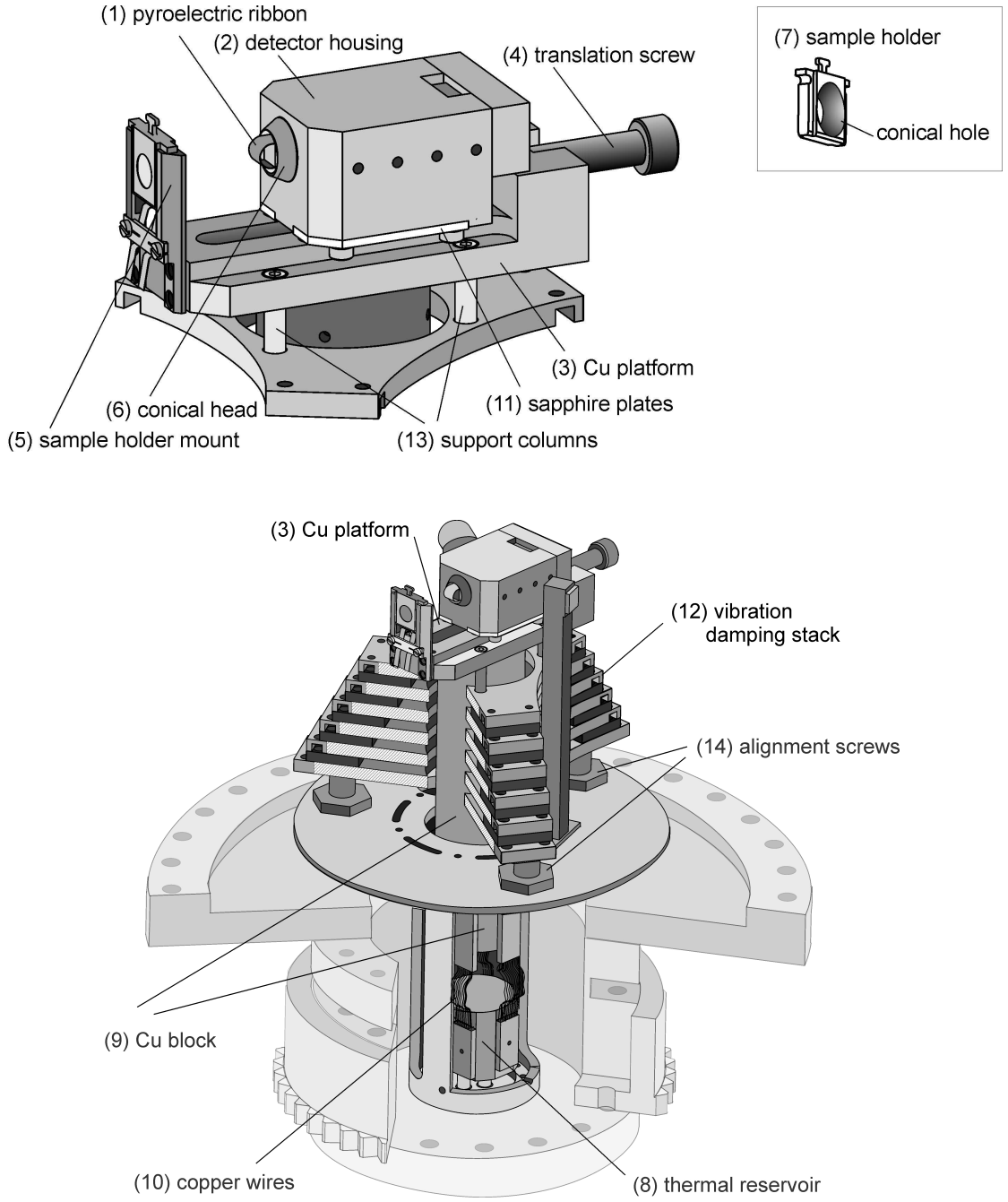

Figure 4.12.: Components of the microcalorimeter: (1) pyroelectric ribbon, (2) detector housing, (3) Cu platform carrying the detector housing and the sample holder mounting, (4) translation screw, (5) sample holder mount, (6) conical head of the detector housing, (7) back view of the sample holder, (8) thermal reservoir, (9) Cu block, (10) copper wires, (11) sapphire plates, (12) vibration damping stack, (13) support columns, (14) set screws.

detector head. Prior to the calorimetric measurement, the detector head is mechanically driven along the Cu platform (3) by using the translation screw (4) and the Allen wrench on a wobble stick (corresponding to (10) in Fig. 4.10) toward the sample holder mount (5) to make a gentle mechanical contact to the back side of the single crystal sample. When in contact with the sample, the highly flexible ribbon flattens, covering about $6 \times 6\,\mathrm{mm}$ of the sample, and allows for efficient heat transfer from the sample to the ribbon. In order to ensure the reproducibility of the contact between the ribbon and the single crystal sample, the detector housing and the sample holder are designed in such a way that their contact is self-aligning and reproducible with respect to the location and extent of compression of the PVDF ribbon. This is achieved by using a conical head (6) of the calorimetric detector and a corresponding negative conical form in the sample holder (7): the cone's outer diameter is designed to mate exactly with the conical hole in the back of the sample holder (see insert in figure 4.12). Once in contact with the sample, the ribbon is shielded from disturbing electromagnetic influences by the grounded sample.

Degradation of the polarization of β-PVDF occurs at $\sim 80^\circ\,\mathrm{C}$ [132, 133]. Therefore, the detector ribbon has to be shielded from thermal radiation and cooled during bake-outs at temperatures $\geq 80^\circ\,\mathrm{C}$.

Electronic Signal Processing

The temperature rise of the crystal induces a temperature change in the pyroelectric detector, causing the developement of a transient face-to-face voltage. The charge, which is generated by a transient heat input, is measured by a high impedance amplifier circuit [134]. Reduction of electromagnetic noise in the chamber is achieved by application of a guarding potential to the coaxial cables. A home-made differential preamplifier with a fixed amplification factor of 100 and a low-pass cut-off frequency of 10 kHz is directly connected to the chamber. A subsequent main amplifier incorporates an adjustable amplifier with an amplification factor between 1 and 1000 and an adjustable band-pass filter with a fixed low-pass cut-off frequency of 10 Hz and a variable high-pass cut-off frequency of 0.2 Hz, 2 Hz or 20 Hz. After the voltage is amplified, it is relayed to a computer, where it is recorded with a sampling frequency of 1 kHz.

The sensitivity varies somewhat from contact to contact due to changes in the thermal connection between the sample and the pyroelectric ribbon and is on the order of $\sim 1\,\mathrm{V/J_{dep}}$, where J_{dep} is the amount of deposited energy. The detector voltage output is calibrated directly after each adsorption measurement with pulses of He-Ne laser light of known intensity and length.

Temperature Stability and Control

Temperature stability of the microcalorimeter setup — including the detector head and the sample holder mount — is a highly important issue for the calorimetric measurement. A drift in the temperature during the calorimetric measurement must not affect the response of the pyroelectric detector.

A measure of the required temperature stability can be estimated as follow:

- The criterion for the temperature stability should be that the measurement of the temperature rise due to adsorption is perturbed by less than 1%.

The temperature rise of the 1 mum thick Pt sample (specific heat capacity of Pt: $0.133\,\mathrm{J g^{-1} K^{-1}}$ [135]) due to adsorption of gas in an area with diameter of 4 mm can be calculated straight forward. The adsorption of $\sim 1\%$ of a monolayer, refering to the number of surfacec atoms of Pt(111)), with a heat of adsorption of $150\,\mathrm{kJ/mol}$, results in a temperature rise of $\sim 0.01\,\mathrm{K}$. Taking into account typical pulse lengths of about 0.2 s, the temperature stability is required to be better than $0.005\,\mathrm{K/s}$ in order to disturb the adsorption by less than 1% with respect to the signal amplitude.

To achieve cryogenic temperatures and ensure the required temperature stability, the Cu platform (3) carrying the detector head, the sample holder mount and the sample holder, if present, is connected to a large Cu block (6). The Cu block itself can be temperature controlled through a thermal connection by thin copper wires (8) (Fig. 4.12) to a thermal reservoir (7). The thermal reservoir is a hollow Cu block, which can be cooled by flowing liquid nitrogen or pre-cooled gases through it via feedthroughs. The large mass of the copper block (6) amounting to about 2 kg provides sufficient temperature stability within hundreds of minutes. The tight contact between the sample holder and the conical detector head allow the sample to come quickly into thermal equilibrium with the whole calorimeter assembly. Particularly, the high thermal conductivity of the Ag translation screw was found to result in a fast temperature equilibration between the freshly cleaned sample and the pre-cooled detector head on a time scale of minutes. This characteristic, which allows the reduction of waiting time and thus the reduction of the associated surface contamination, is crucial to minimize the uptake of adsorbates from the background prior to the calorimetric measurement.

Vibration Damping

In order to attenuate the vibrational noise in the detector signal, the Cu platform (3) carrying the detector head and the sample holder mount is placed on a vibration damping stack (12) (Fig. 4.12). The stack consists of six stainless steel plates of 6 mm thickness, separated by Viton plates of 5 mm thickness. The change in material deflects acoustic waves due to the change in acoustic impedance. Further, the dimensions of the stainless steel plates are monotonously decreasing with each layer to shift the eigenfrequencies with respect to each other. The Cu platform is connected to the uppermost plate of the stack with four support columns (13). To preserve the damping quality of the Viton material that becomes stiff at low temperatures it is desirable to reduce the thermal contact between the cooled Cu platform and the vibration damping stack. For this purpose, the support columns connecting these two components were designed in the form of thin-walled stainless steel tubes providing low thermal conductance. The adjustment of the height of the microcalorimeter on the vibration damping stack to the non-variable height of the molecular beam aperture is realized by three alignment screws (14).

4.3.2. Molecular Beam Source

The molecular beam is designed to provide a constant, homogeneous and clean gas flux. In order to ensure a homogeneous spatial profile of the gas flux on the sample surface, the molecular beam was placed in the closest possible proximity to the sample surface with the distance between the sample and the molecular beam aperture amounting to 4 mm. This geometric arrangement allows

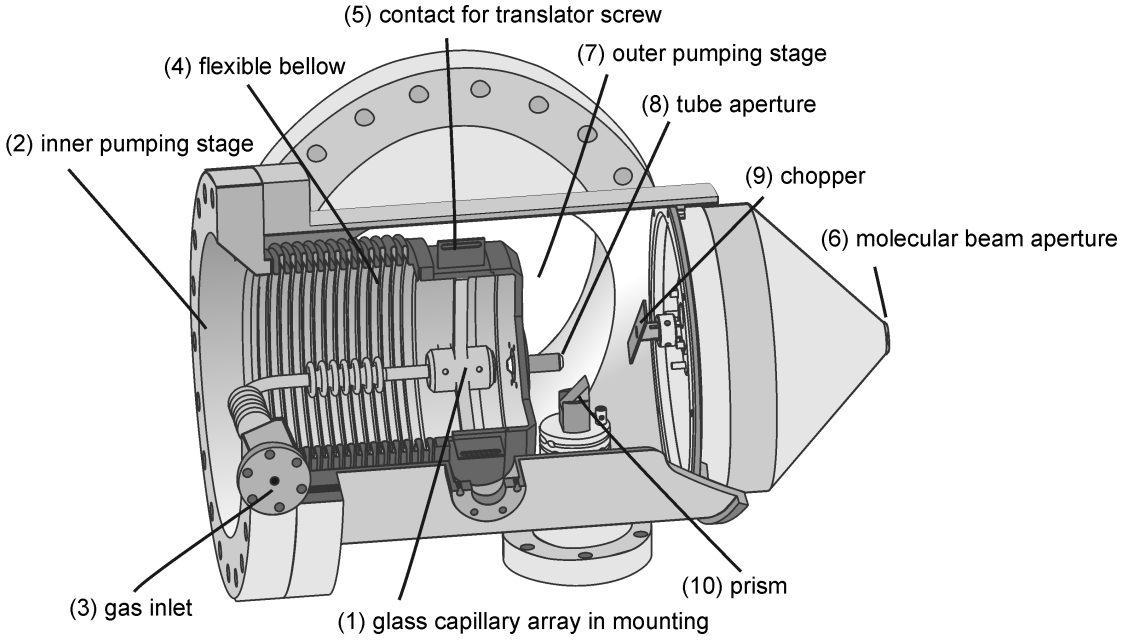

Figure 4.13.: Schematic of the effusive beam

minimization of the divergence of the gas flux which increases with the distance and could result in a non-homogeneous distribution of the flux intensity over the sample surface. Additionally, the experimental possibility of coupling laser light into the beam path is provided, which is necessary for the energy calibration described in section 4.3.3.

Effusive Molecular Beam

The molecular beam design is an adaptation of the recently published effusive beam design by Libuda *et al.* [136]. A cross section of the molecular beam is shown in figure 4.13. The molecular beam is produced by a differentially pumped source with a glass capillary array (GCA) (Galileo)(1), which is placed at a distance of $\sim 200\,\mathrm{mm}$ from the sample. The expansion capillary used in the effusive beam source has a length of 1 mm and a diameter of $50\,\mu\mathrm{m}$ resulting in a *peaking factor* (see equation 3.2) of 15. To process the GCA, it was sealed with lacquer, cut from a larger piece and milled into a disk of 10 mm diameter. After processing, the protective sealing was removed and the device was mounted in a tube using Teflon gaskets with an opening of 4 mm diameter. The GCA mounting is located in an inner pumping stage (2) which is differentially pumped by a $500\,\mathrm{L/s}$ TMP (Pfeiffer, TMU 521 P). The GCA is connected to a gas inlet (3) via a flexible stainless steel hose. The inner pumping stage has a flexible bellow (4) allowing directional adjustment by two translator screws (5). In order to maximize the pumping speed and to minimize the distance to the molecular beam aperture (6) the outer pumping stage (7) was constructed as an integral part of the calorimetry chamber. After exiting the inner pumping stage through a tube aperture (8) of 4 mm diameter the molecular beam enters the outer pumping stage (7), where it can be modulated by means of a chopper (9). The beam chopper is a rectangular

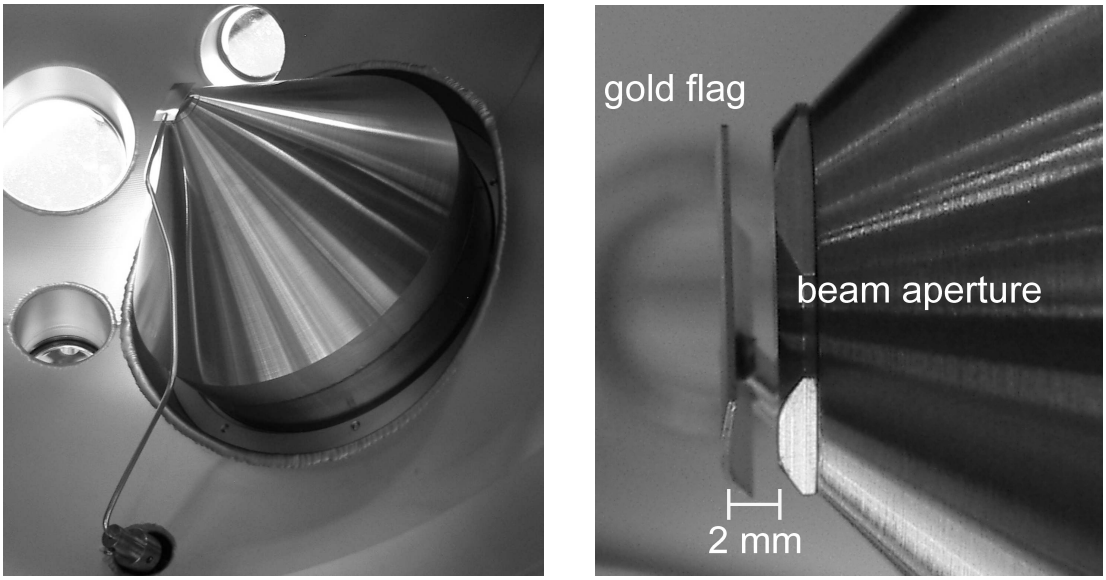

Figure 4.14.: The gold flag in front of the molecular beam aperture at a distance of about 2 mm

metal plate, which is driven by a UHV-compatible stepper motor (AML, B14.1). The chopper is remotely controlled (using a LabVIEW program) and allows arbitrary opening times of at least 150 ms. The chopper position, at which the chopper blade blocks the molecular beam, can be controllably set by utilizing a magnetic reed-switch and small magnets mounted to the ends of the chopper blade. For the calibration of the absolute values of adsorption energy, a laser beam can be coupled into the molecular beam path by using a prism (10). The prism is fixed on a translational feed-through, and can be positioned in the outer pumping stage either below the inner aperture (6) or in front of it. The former position is the working position for the adsorption experiments, when the beam of the gas molecules passes undisturbed through the entire beam path. The latter position is used during the energy calibration, when the laser light is guided into the molecular beam path (for more details to the calibration system see section 4.3.3). Finally, the molecular beam passes from the outer pumping stage to the calorimetry chamber through the molecular beam aperture (11) of 4 mm diameter, at 4 mm distance from the sample.

The required backing pressure for the GCA, typically of 10^{-3} to 10^{-1} mbar, is maintained by two independent mass flow control units, which can be switch to the backside of the GCA by electro-pneumatic valves. This allows fast changing of the gas of the molecular beam. The electro-pneumatic valves are computer-controlled and allow for automated pulsing sequences. See section 4.2.4 for more details on the gas supply system.

Gold Flag

The flux of molecules in the calorimetry chamber can be blocked from impinging on the sample by a sheet of gold. The gold flag can be positioned between the effusive beam aperture and the sample in the calorimeter. Figure 4.14 shows the gold flag in front of the molecular beam aperture at a distance of about 2 mm. An electro-pneumatic rotational motion moves the gold flag

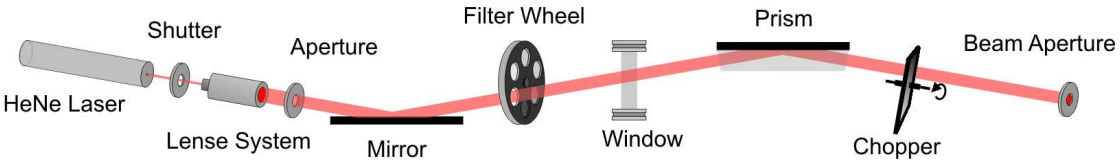

Figure 4.15.: Schematic of the Energy Calibration System

between the blocking and the unblocked position. The electro-pneumatic motion is computer-controlled and allows for automated pulsing sequences.

4.3.3. Energy Calibration System

The energy input of the calorimeter is calibrated by means of a laser beam. The laser pulse is identical to the molecular beam pulse in terms of width and length passes. Thereby the projection of the laser beam and the molecular beam coincide at the position of the sample. The energy calibration setup is schematically shown in figure 4.15. A He-Ne laser (Linos, 632.8 nm, 2 mW, cw) is the source for the absolute energy calibration of the pyroelectric calorimeter. The laser spot is widened and collimated by means of lenses and apertures. A motorized wheel with six different optical neutral density filters allows reproducible laser power attenuation. The laser beam is guided into the molecular beam through a window. Inside the molecular beam the laser beam is deflected in a prism, which is mounted on a translational feed-through. The prism on the translation stage is shown in figure 4.13. For the energy calibration, the prism can be positioned in the molecular beam path. It redirects the laser beam into the molecular beam path onto the sample. This procedure allows to pulse the laser beam onto the sample in the same geometry and with the same temporal profile as the molecular beam. To measure the laser power as well as the pulse timing a calibrated in situ photodiode can be positioned in front of the molecular beam by the rotation platform.

The laser power at the sample position is susceptible to changes due to variations in the alignment of the laser beam by the retractable prism. Therefore the laser power has to be determined at the sample position in the calorimetry chamber by an in situ photodiode (Silicon Sensor, PS95-4) for every energy calibration procedure. The photodiode response is amplified and converted to a voltage by a home-made current-to-voltage converter. In this manner, the calorimeter response during adsorption measurements can be directly compared to the signal from heating by laser pulse absorption of known energy.

4.3.4. Beam Monitor

Accuracy in the determination of the molecular flux and its spatial distribution requires reliable measurement of the beam intensity and its profile. For this purpose an accumulation detector was set up which is referred to as the beam monitor. More details on accumulation gauges can be found elsewhere [124, 125]. The beam monitor is based on a high accuracy ion gauge (Granville-Phillips, 370 Stabil-Ion) mounted on one end of a stainless steel tube of 490 mm length and a diameter of 14 mm. On the other end of the tube a hole of 1 mm diameter opens the tube volume to the UHV chamber. This hole acts as a probe to measure the local pressure.

The assembly is mounted to a translational feed-through to the rotatable platform allowing the detector to be positioned exactly in the sample position of adsorption/reaction experiments.

In the working position, the stainless steel membrane of the beam monitor is placed perpendicular to the incoming molecular beam (and parallel to the sample surface). The molecular beam passing the aperture hole causes a pressure rise inside the detector volume. After equilibration of the incoming flux and the outgoing effusive flux from the detector volume a constant pressure is established in the tube. The ion gauge was calibrated with nitrogen. After correction for the gas specific ionization gauge sensitivity the pressure can be directly converted to absolute beam fluxes by the following relation derived from kinetic gas theory [32]:

$$\frac{\mathrm{d}N_{out}}{\mathrm{d}t} = \frac{p}{\sqrt{2\,\pi\,M\,K_b\,T}}, \tag{4.1}$$

where N_{out} is the number of molecules passing the beam monitor aperture, p is the pressure in the detector volume, M is the mass of the molecule, k_B is the Boltzmann constant and T is the temperature of the detector. The high stability pressure gauge has an accuracy of 4% and a precision of 3%. Typically the background pressure in the detector is about $5 \cdot 10^{-9}$ mbar so that the minimum detectable pressure change is $1 \cdot 10^{-11}$ mbar. For Argon this corresponds to a resolution in flux density of $2 \cdot 10^{9}$ molecules $\mathrm{cm}^{-2}\mathrm{s}^{-1}$.

5. Microcalorimeter Calibration

In this chapter, the calibration of the adsorption microcalorimetry experiment is discussed. The discussion is divided into two sections: (i) the estimation of the number of adsorbing molecules or atoms per pulse, inducing a transient heat signal in the calorimeter and (ii) an energy calibration of the calorimeter signal.

5.1. Estimation of the Number of adsorbing Molecules per Pulse

For the estimation of the number of adsorbing molecules or atoms per pulse, two parameters are essential: the total number of molecules or atoms arriving at the surface and their coverage dependent probability to stick. The former value is determined by the molecular beam flux, the beam profile and the length of the beam pulse.

5.1.1. Calibration of the Effusive Beam Source

By means of the beam monitor the local pressure at the sample position, created by expansion of Ar, was probed at varying backing pressure conditions. For this measurement the beam monitor was placed in front of the molecular beam aperture in exactly the same position, where the sample is placed during the microcalorimetric experiment. The local pressure is converted into an actual flux of molecules using equation 4.1. Figure 5.1a shows the molecular beam flux as a function of backing pressure: (i) the local pressure on the right axis and (ii) the corresponding centerline intensity of the Ar flux on the left axis. The pressure dependence of the Ar flux intensity I_{Ar} is linear up to backing pressures p of about 10^{-1} mbar, where $I \propto p$. For higher pressures the proportionality changes to $I \propto \sqrt{p}$, indicating that the particle-particle collisions become as important as collisions with the walls of the expansion tubes. The highest flux was about $1.5 \cdot 10^{15}$ molecules $\mathrm{cm}^{-2}\ \mathrm{s}^{-1}$. In principle, there is no lower limit to the beam intensity. However, the components of the source pressure regulation limit the range of controllable values to about $5 \cdot 10^{12}\,\mathrm{molecules} \cdot \mathrm{cm}^{-2} \cdot \mathrm{s}^{-1}$. Fluctuations of the molecular beam flux could not be detected and are therefore below 0.2%. It should be noted that the effusive beam expansion starts from low pressure conditions with nearly non-interacting gas phase particles so that this type of expansion is essentially gas independent. This calibration is directly applicable for argon. For other molecules or atoms the flux has to be multiplied by a constant c_M accounting for the difference in mass of Ar M_{Ar} and the expanding molecules or atoms $M_{molecule}$: $c_M = \sqrt{M_{Ar}}/\sqrt{M_{molecule}}$.

Variable time modulation of the molecular flux by means of chopper allows to produce arbitrary beam pulse lengths of at least 150 ms. The pulse length is verified by laser pulses which can be detected by the in situ photodiode. No variation of the pulse length was observed within the

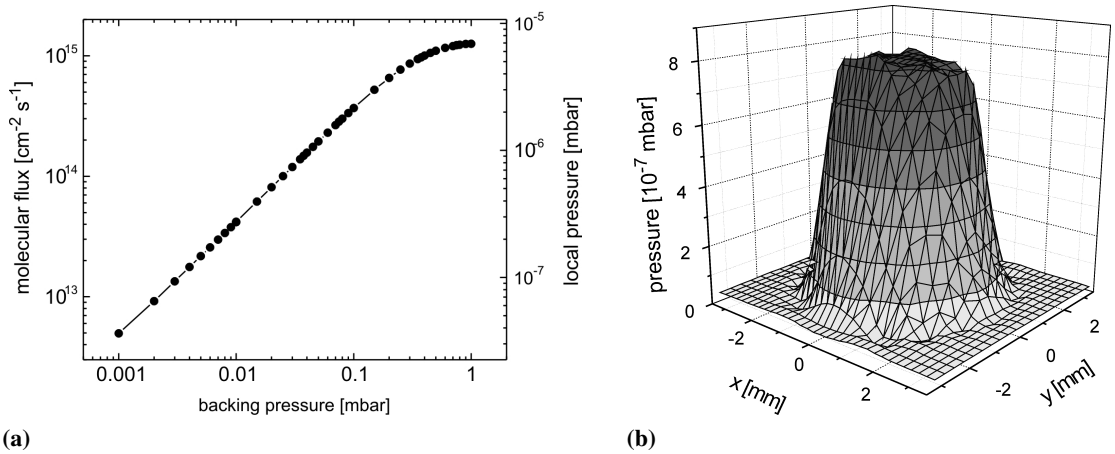

Figure 5.1.: Calibration of the molecular beam source: (a) molecular flux as a function of backing pressure and (b) the beam profile of the molecular beam

time resolution of 1 ms. The upper limit for the relative error of the pulse length was estimated to be 0.7%.

The intensity profile of the molecular beam was scanned by changing the position of the beam monitor with respect to the molecular beam aperture. Figure 5.1b shows a two-dimensional beam profile at a gas source pressure of (0.0375 ± 0.0001) mbar. The relative variation of the beam intensity, while scanning over the central plateau, was 1.1%, being lower than the stated precision of 3% by the manufacturer. Taking into account a convolution of the intensity profile with the beam monitor's aperture of (1.00 ± 0.05) mm diameter (checked with an optical microscope), the profile shown in figure 5.1b is confined homogeneously in an area of (4.0 ± 0.1) mm diameter, resulting in a relative uncertainty of 5% in the beam profile area.

The observations in figure 5.1a and 5.1b attest a homogeneous and stable flux of gaseous species on the sample surface.

5.1.2. Sticking Probability

The determination of the sticking probability is based on the King-Wells method which is described in section 3.3. The King-Wells method relies on an accurate measurement of the change in the partial pressure of the adsorbate. The analysis can be complicated by two additional contributions: (i) the change of the baseline pressure due to accumulation of adsorbates in the chamber and (ii) the change in the scattering geometry of the molecular beam introduced by the retraction of the gold flag from the beam path.

Correction of the Baseline Intensity

The sticking probability measurement on the sample can be superimposed with adsorption on the chamber components, e.g chamber walls, copper wires, etc. Experimentally, this phenomenon is reflected in a growing partial pressure of the adsorbate in the UHV chamber. This becomes

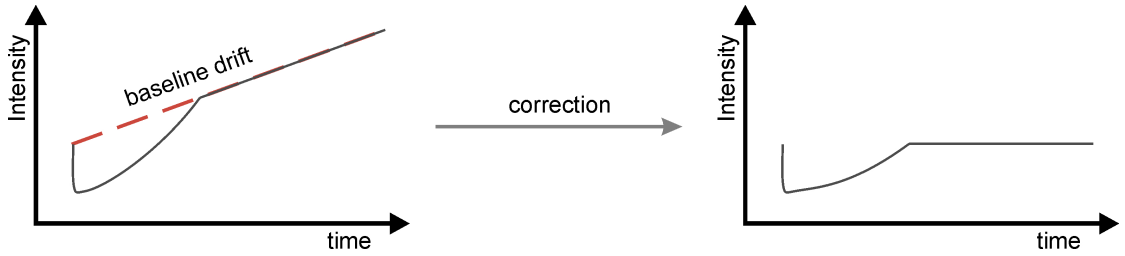

Figure 5.2.: An example of a possible baseline drift during a sticking probability measurement and the corresponding correction by subtraction of a linear component. The linear component is derived from the range where the sample is already saturated.

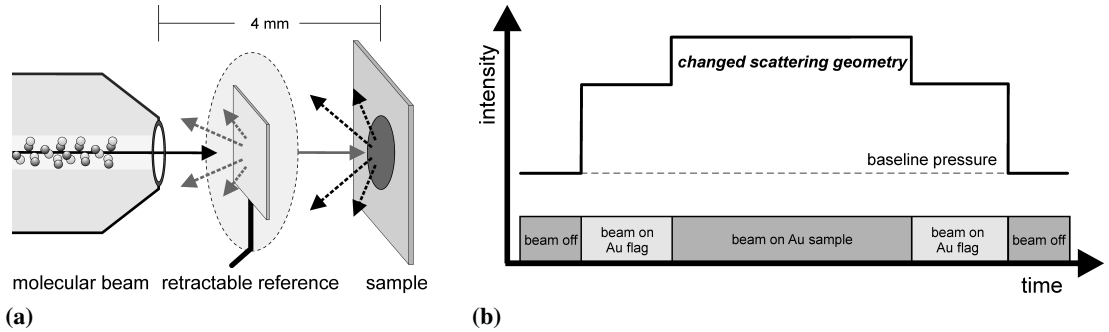

Figure 5.3.: Schematic of (a) the impact of the gold flag on the scattering geometry, introducing a substantial change and (b) the possible effects of the change in the scattering geometry on the QMS intensity of the scattered molecular beam

specifically obvious after saturation of the sample surface. Therefore the baseline of the sticking probability measurement needs to be corrected if it is not constant. Figure 5.2 shows a schematic of the baseline pressure drift and its correction. Firstly, the baseline drift is estimated in the range of the signal where the sample has already been saturated. The slope of the baseline is estimated by a linear fit. Secondly, the derived slope is subtracted from the raw data. Afterward, the sticking probabilities can be calculated according to section 3.3.

Correction of the Change in Scattering Geometry

The sticking probability is derived by comparison of the beam intensity scattered by the sample to the beam intensity scattered by a reference, a gold flag in the present case (see section 3.3). Figure 5.3a illustrates the scattering geometry, indicating also the distance of 4 mm from the molecular beam aperture to the sample. The gold flag is positioned approximately at 2 mm distance to the beam. During the sticking probability measurement the gold flag is retracted from the molecular beam path. It was observed with a non-sticking sample that the mass spectrometer intensity of the scattered molecular beam changes significantly upon retraction. This change in mass spectrometer intensity can be attributed to a significant change in the scattering geometry

where the gold flag is 2 mm distant from the molecular beam aperture and the sample is 4 mm away, indicating an anisotropic distribution of scattered molecules in the calorimetry chamber.

The change in scattering geometry can be assessed by comparison of QMS signal intensities of the molecular beam scattered by the gold flag with the scattering from a gold sample. Figure 5.3b shows a schematic of the evolution of the QMS signal intensity during the experiment. Initially, the gold flag is positioned in front of the sample. After the beam is switched on, molecules impinge on the gold flag and are scattered into the chamber. A constant background pressure establishes. Retracting the gold flag results in a change of the observed QMS signal intensity due to the change in scattering geometry. The change in scattering geometry has to be accounted for in the calculation of the sticking probability. During a typical adsorption experiment only the gold flag is present as the gold sample is replaced by a model surface. The QMS signal intensity of the molecules scattered by the gold flag has to be scaled to result in the correct reference intensity at the sample position. This is done by the intensity ratio $r_{geometry} = I_{sample}/I_{flag}$, where I_{sample} is the QMS signal intensity of the molecular beam impinging on the sample and I_{flag} the QMS signal intensity of the molecular beam impinging on the gold flag. Typical values of $r_{geometry}$ are around 1.46.

For CO adsorption on Pt(111), relative variations of 1.5% at high sticking probabilities ($S \approx 0.7$) – corresponding to low surface coverages – and 30% for low sticking probabilities ($S \approx 0.3$)– corresponding to high surface coverages – were found.

5.2. Energy Calibration of the Calorimeter

Absolute energy calibration requires determining the contact sensitivity of the pyroelectric detector, which is measured as a voltage produced by the pyroelectric ribbon per unit of absorbed energy (typically $\mathrm{V/J}$). This sensitivity has to be calibrated for each new contact between the ribbon and the sample in order to account for differences in the heat transfer. For energy calibration pulses of laser light of identical length as the molecular beam pulses are incident onto the sample. The fraction of the laser light that is absorbed by the sample depends on the sample's reflectivity, which has to be determined in a separate experiment. These two parameters – the laser power and the sample reflectivity – are used to calculate the absolute amount of the absorbed energy per laser pulse. Subsequently, the absorbed energy can be related to the voltage produced by a pyroelectric detector. Therefore, precise quantification of the absorbed energy requires accurate in-situ measurement of the laser power and the sample reflectivity.

5.2.1. Laser Power Measurement

The laser intensity can be measured in-situ by irradiation of the in situ photodiode (Silicon Sensor, PS95-4). Figure 5.4 shows a typical photodiode response to an incident laser light pulse. The according pulse length was derived to be 266 ± 1 ms. After warm up, the variation of the laser power with time shows a standard deviation of about 0.1%. The length of the pulse remains constant within the time resolution given by the rise time of the photodiode of 1 ms. The signal amplitude is (-83.69 ± 0.03) mV, corresponding to a laser power of $(39.52 \pm 0.01)\,\mu$W.

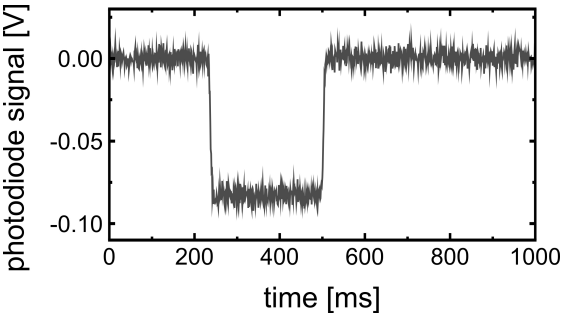

Figure 5.4: Photodiode response to a laser pulse of $(266 \pm 1)\,\mathrm{ms}$ length. The signal amplitude is $(-83.69 \pm 0.03)\,\mathrm{mV}$, corresponding to a laser power of $(39.52 \pm 0.01)\,\mu\mathrm{W}$. The displayed signal is an average of 20 measured signals.

The sensitivity of the in situ photodiode is characterized by a separate absolutely calibrated *reference photodiode* (Thorlabs, FDS1010). The reference photodiode was calibrated at the Physikalisch-Technische Bundesanstalt (PTB). The absolute sensitivity of the reference photodiode was determined to be $350.30 \pm 0.49\,\mathrm{mA/W}$ at $632.8\,\mathrm{nm}$. The stated error refers to a 95% confidence level and corresponds to a relative error of about 0.1%. For calibration the reference photodiode is fixed in the calorimeter sample holder mount, facing the molecular beam. The laser beam intensity and the background intensity is recorded with long exposure times. After determining the laser power, the rotatable platform is used to bring the in situ photodiode in the same position. Thereby the sensitivity of the in situ photodiode including the current-to-voltage converter was found to be $472.2 \pm 0.4\,\mu\mathrm{W/V}$. The relative error is 0.1%.

The laser power incident on the sample can be varied by a filter wheel containing six filters. Transmission coefficients T_i, for $i = 1$ to 6, are determined by comparison of the transmitted laser power I_i, relative to the filter with the highest transmission I_{max}:

$$T_i = \frac{I_i}{I_{1=max}} \tag{5.1}$$

Transmission coefficients of 1.000, 0.285, 0.104, 0.079, 0.068 and 0.053 including an uncertainty of ± 0.001 were found. By using these filers the laser power can be varied in the range between $\sim 1\,\mu\mathrm{W}$ and $\sim 30\,\mu\mathrm{W}$. The corresponding minimum pulse energy, which can be deposited into the sample with the laser power of $1\,\mu\mathrm{W}$ and a beam modulation time of 150 ms, amounts to 150 nJ. Further attenuation of the laser power is possible by introducing additional neutral density filters in the laser beam line.

5.2.2. Reflectivity Measurement

The capability of in situ reflectivity determination is an important prerequisite for the accurate determination of adsorption heats. Maintaining UHV conditions during optical characterization is important as the sample surfaces may change when they are exposed to air. For instance, the reformation of FeO/Pt(111) to FeO_2/Pt(111) under oxygen pressure was reported recently [137].

For the reflectivity measurements the ratio of the reflected intensity $I_{Reflection}$ and the laser intensity I_{Laser} serves as a measure for the reflectivity R:

$$R \propto \frac{I_{Reflection}}{I_{Laser}} \tag{5.2}$$

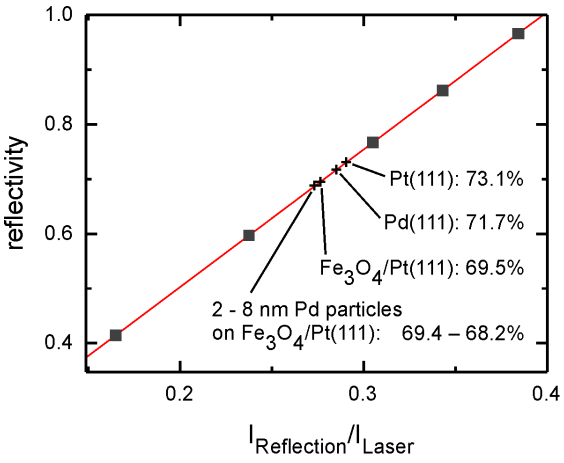

Figure 5.5: The calibration curve showing the dependence of the reflectivity of the calibration mirrors on the photodiode intensity ratio $I_{Reflection}/I_{Laser}$ (black squares). The positions of the reflectivities for different samples are indicated by star symbols.

The dependency of the intensity ratio on the reflectivity is calibrated by means of five mirrors of known reflectance: $(41.4 \pm 0.4)\%$, $(59.7 \pm 0.9)\%$, $(76.7 \pm 1.1)\%$, $(86.2 \pm 0.2)\%$, $(96.6 \pm 0.1)\%$. Figure 5.5 shows the linear dependency of the photodiode intensity ratio on the reflectivity of the surface. Values obtained with this setup for different model surfaces investigated in this study are indicated as well.

The reflectivity at 632.8 nm was determined for Pt(111), Pd(111), thin film Fe_3O_4 on Pt(111) and Fe_3O_4/Pt(111) supported Pd particles of different sizes. The respective reflectivities are $(73.1 \pm 0.1)\%$, $(71.7 \pm 1)\%$, $(69.6 \pm 1)\%$ and $(69.4 \pm 1)\%$ to $(68.2 \pm 1)\%$ at 298 K. The reflectivity of the Pd particles and the Fe_3O_4/Pt(111) will be discussed in section 7.1.4.

The reflectivity of pristine Pt(111) at a wavelength of 632.8 nm, corresponding to a photon energy of ~ 1.95 eV, was determined at 298 and 120 K. A significant temperature dependence was found. The reflectivity increases from $(73.1 \pm 0.1)\%$ to $(74.1 \pm 0.3)\%$ going from 298 K to 120 K. This temperature dependence may be related to two effects: (i) a change of the dielectric function and (ii) a change of the electronic interband transitions [138].

- The complex dielectric function $\varepsilon(\omega)$, where ω is the frequency, is related to the reflectivity R by:

$$R(\omega) = \left| \frac{\sqrt{\varepsilon(\omega)} - 1}{\sqrt{\varepsilon(\omega)} + 1} \right|^2 \tag{5.3}$$

  The temperature dependence of the dielectric function becomes most obvious in the relation to the plasma frequency ω_p for vanishing wave vector $\vec{K}$:

$$\varepsilon(\omega, \vec{K} = 0) = 1 - \left(\frac{\omega_p}{\omega} \right)^2 \tag{5.4}$$

  Consequently a shift of the plasma frequency ω_p results in an increase or decrease of the dielectric function at the frequency ω. The plasma frequency is defined as:

$$\omega_p = \frac{ne^2}{\varepsilon_0 m^*} \tag{5.5}$$

where n is the electron density, ε_0 the vacuum permittivity and m^* the effective mass of the electron. Both, the electron density n and the effective mass m^* are temperature dependent quantities.

- Interband transition are optical excitations of electrons to other bands. The wave vector k remains essentially unchanged. The excitation has a threshold energy analog to the excitation of an electron across the band gap of an insulator. With increasing temperature the band gap tends to decrease and consequently the resonance shifts to lower energies. Further, the thermally excited electrons induce a broadening of the resonance due to smearing of the electrons' Fermi-Dirac distribution.

The obtained value at room temperature coincides within 3% with most of the published data on the reflectivity of Pt, either bulk material or evaporated films. Yu *et al.* reported $\sim 75\%$ for an electron gun grown Pt film [139], for Pt(111) King *et al.* reported $(71.5 \pm 0.5)\%$ [82] and Campbell et al. reported 76% [108]. Only Weaver *et al.* found a substantially lower reflectivity of 67% on a polycrystalline Pt sample [140].

The necessity to characterize the reflectivity of model catalyst systems may be obvious. However, the observed temperature dependence of the reflectivity underlines the importance of the in situ determination of the optical reflectivity. It should be emphasized, that already the temperature dependent variation in the absorptivity $A = 1 - R$ leads to a relative change of 1.4% of the heat of adsorption. Therefore the in situ characterization of the surface reflectivity is a major step to minimize the uncertainty of the energy calibration. The precision of a reflectivity measurement depends on two aspects: (i) random variations by the setup and (ii) the quality and reproducibility of the surface. For the Pt(111) surface at room temperature, the reflectivity was determined by repeated measurements with a relative statistical error of 0.1% (error of mean).

5.2.3. Calibration of the Calorimeter Response

For calibration the molecular beam is substituted by the laser beam in the same geometry by inserting the prism into the beam path. Light of known power and same pulse length as the molecular beam are pulsed onto the sample, introducing a defined energy input by light absorption. The dissipation of the thermal energy from the sample to the pyroelectric ribbon is affected by their microscopic contacts which are unique for each approach of the ribbon and the sample. Consequently, the energy calibration of the calorimeter is necessary for each new contact of the pyroelectric ribbon and the sample.

Response to transient Temperature Changes

Single crystal adsorption calorimetry is based on the monitoring of a transient temperature rise caused by energy deposition. In the present case the energy may stem either from light adsorption or gas particle adsorption. Figure 5.6 shows examples of calorimeter responses for different absorbed energies. The displayed signals are averages of 20 measured signals. The linear rise of the signal coincides with the time of the energy input by the laser pulse. The signal amplitude of the calorimeter response signal is a measure for the amount of charge generated by the pyroelectric ribbon. Figure 5.7 shows the signal amplitudes as a function of absorbed energy. A

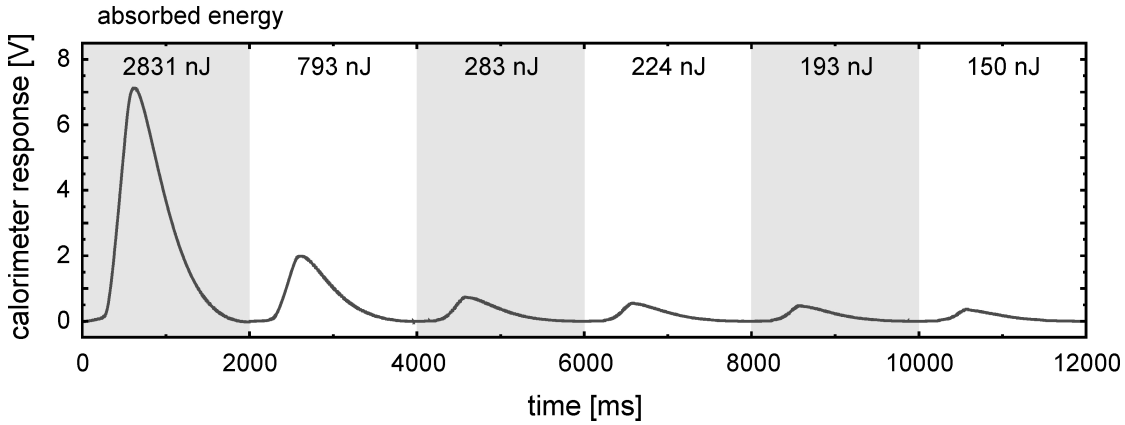

Figure 5.6.: Calorimeter response to absorption of a $(266 \pm 1)\,\mathrm{ms}$ laser pulse of different power on Pt(111). The resulting absorbed energy input is display. The laser power is varied by using neutral density filters. The signals are averages of 20 signals.

Figure 5.7: The amplitudes of the calorimeter response signals, shown in figure 5.6, are plotted as a function of absorbed energy. The amplitude shows a linear dependency on the absorbed energy. For this particular contact of the calorimeter to the sample the sensitivity is estimated to be $(2.523 \pm 0.004)\,\mathrm{V}/\mu\mathrm{J}$ with an offset of $(17 \pm 2)\,\mathrm{mV}$

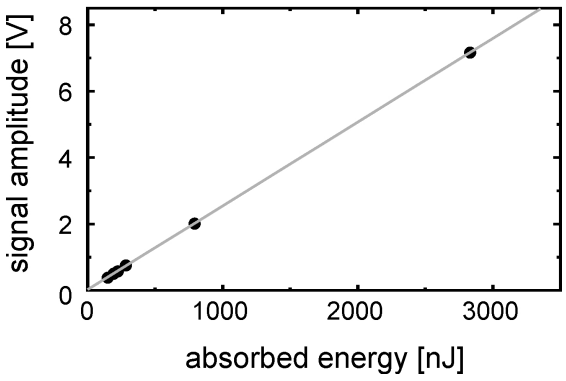

linear dependency of the signal amplitude on the absorbed energy is evident. The sensitivity of the calorimeter is determined by the slope of an according linear fit. The present offset relates to noise contributions in the calorimeter response. Typically sensitivities of 1 to $5\,\mathrm{V}/\mu\mathrm{J}$ can be achieved, depending on the thermal contact of pyroelectric ribbon and sample. The pulse-to-pulse standard deviation in energy, based on the standard deviation of the calorimeter signal amplitudes, was evaluated at an absorbed energy per pulse of 245 nJ at room temperature. After collecting calorimeter signals of 100 pulses the standard deviation of the signal amplitudes was determined and multiplied by the sensitivity of $1.9\,\mathrm{V}/\mu\mathrm{J}$. The resulting pulse-to-pulse standard deviation in energy is about 15 nJ. The signal amplitudes are regularly determined with lower statistics of typically 20 pulses. The absorbed energy during the calibration ranges from about 150 to 3500 nJ. Corresponding pulse-to-pulse standard deviation were found between 4 and 16 nJ. To relate the pulse-to-pulse standard deviation to other types of microcalorimeters the sensitive area of $0.126\,\mathrm{cm}^2$ has to be considered. The energy dependent pulse-to-pulse standard deviation in energy of 15 nJ corresponds to a pulse-to-pulse standard deviation of $120\,\mathrm{nJ}/\mathrm{cm}^2$ re-

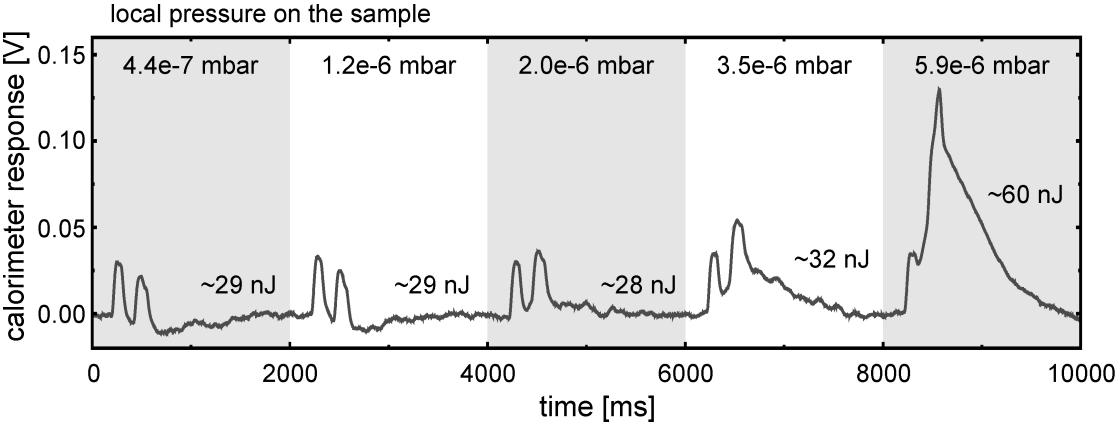

Figure 5.8.: Calorimeter response and the corresponding energy equivalent to argon impinging on Pt(111) at different molecular fluxes resulting in the stated local pressure changes. Energy equivalents of the induced signal are given. The two peaks of about 30 mV, which are present in every signal, originate from high frequency cross talk of the UHV stepper motor operating the beam chopper. The energy estimation is an extrapolation out of the calibration range and should be considered accordingly with reduced reliance.

ferring to the energy density. A resolution of $120\,\mathrm{nJ/cm^2}$ corresponds to an equivalent amount of $4 \cdot 10^{-4}$ monolayers ($1.5 \cdot 10^{15}\,\mathrm{cm^{-2}}$) of CO on Pt(111) with a heat of adsorption of $130\,\mathrm{kJ/mol}$. Similar pulse-to-pulse standard deviations of 13 to 19 nJ were found by Campbell and coworkers, using etched $\beta-$PVDF ribbons in their calorimeter [110]. It should be emphasized that the extrapolation of the energy calibration, especially for lower energies, may not be necessarily valid. Reliable conclusions can only be drawn within the calibration range.

The variation in the determined energy result in a relative uncertainty of $15\,\mathrm{nJ}/E_{dep}$, e.g. $\leq 10\%$ for deposited energies E_{dep} of $\geq 150\,\mathrm{nJ}$. The lower detection limit in energy is set by the calibration range.

Response to transient Pressure Changes

The microcalorimeter detector is sensitive to pressure changes due to its piezoelectricity. Therefore the intensity of the molecular beam source was varied to estimate potential contributions to the calorimeter response signal. Figure 5.8 shows the microcalorimeter signal produced upon scattering of argon pulses from Pt(111) at room temperature. It should be noted that Ar does not adsorb on Pt(111) at this temperature. The local pressure generated by the molecular beam pulse on the sample is varied between $4.4 \cdot 10^{-7}$ and $5.9 \cdot 10^{-6}\,\mathrm{mbar}$. Two peaks of about 30 mV are visible at low pressures. These peaks originate from high frequency cross talk of the UHV stepper motor operating the beam chopper. Energy equivalents were calculated according to calorimeter signal amplitudes and the known calorimeter sensitivity. It has to be mentioned here that the energies stated in figure 5.8 are estimated from linear extrapolation of the energy calibration. Linearity has not been verified below 150 nJ. The estimated energies should be

considered accordingly with reduced reliance in the actual energy values. The local pressure shows no effect on the amplitude of the calorimeter signal amplitude below $2.0 \cdot 10^{-6}$ mbar. Above $2.0 \cdot 10^{-6}$ mbar detectable contributions become obvious. The adsorption experiments in the following studies of this work used beam intensities that correspond to a local pressure of $4.4 \cdot 10^{-7}$ mbar on the sample.

5.3. Summary of relative Calibration Errors

The relative errors of subsequent measurements are of vital importance for the significance of determined adsorption energies. The errors can be divided into parameters determining the number of adsorbates per pulse and parameters determining the deposited energy. Further, the presented errors are split up into precision and accuracy, i.e. statistical errors and systematic errors. The precision of the measured value can be improved by the accumulation of statistics. The accuracy is a systematic error and remains constant. Systematic error are difficult to estimate, especially in the absence of absolute standards as e.g. in the case of the sticking probability.

Table 5.1 summarizes the estimated values contributing to the overall errors of a single calorimetric measurement. The statistical errors are added in quadrature due to the virtue of being essentially independent. The systematic errors are summed, as they need not be normally distributed, resulting in an upper limit. The accuracy is mainly limited by the uncertainty in the beam monitor sensitivity of 4%. The accuracy of the sticking coefficient is unknown as no measurement standard exists.
However, the precision of the sticking probability is deduced from the variation of the sticking probabilities for CO adsorption on Pt(111).

The error of the calorimetrically determined energy is set by the pulse-to-pulse standard deviation of 15 nJ. An upper limit of 10% is set by the lower calibration limit of 150 nJ. This energy corresponds to the adsorption of 0.3% of a monolayer (corresponding to $1.5 \cdot 10^{15}\,\mathrm{cm}^{-2}$) of CO on pristine Pt(111) with a heat of adsorption of 130 kJ/mol. Typically, 1% of a monolayer is initially adsorbed per pulse, yielding detected energies around 500 nJ and a relative statistical error of 3%. The statistical error of the heat of adsorption is $6.3 - 32.0\%$ for a single measurement and can be improved by collecting further statistics. The systematic error is about 5%. It should be noted that statistics of adsorption experiments improve foremost the contributions of the calorimeter signal amplitude and the sticking probability.

However, in the case of supported model catalysts the ability to prepare identical surfaces is limited. Therefore, additional contributions from variations in the prepared surfaces will contribute to the statistical error of the determined heats of adsorption.

Table 5.1.: Summary of relative calibration errors; divided into the errors concerning the determination of the number of adsorbates and the errors of the energy measurement

Number of Adsorbates	precision	accuracy	origin
beam monitor	1.1%	4%	Standard deviation of 46 measrurements; accuracy as stated by the manufacturer
molecular beam stability	$\leq 0.2\%$		Upper limit, set by the detection limit of the beam monitor;
beam profile area	5%		The beam diameter was determined to be (4.0 ± 0.1) mm
pulse length	$\leq 0.7\%$		Upper limit derived from the timing resolution of 1 ms
high sticking probability ($S \approx 0.7$)	1.5%		Standard deviation for CO adsorption on Pt(111),
low sticking probability ($S \approx 0.3$)	30%		six measurements
total errors	$5.4 - 30.4\%$	4%	
Energy Measurement			
photodiode	0.1%	0.1%	Error of mean, 62000 measurements; accuracy stated by calibration lab.
laser power stability	0.1%		Standard deviation, 120000 measurements
neutral density filter	1%		Error of mean, 62000 measurements
reflectivity	0.1%	1.2%	Error of mean for Pt(111), 29 measurements; accuracy determined by reference
pulse length	$\leq 0.7\%$		Upper limit derived from the timing resolution of 1 ms
calorimeter signal amplitude	typically 3%		Standard deviation for deposited energies around 500 nJ. An upper limit of 10% is set by the lower calibration limit of 150 nJ, see text.
total errors	$3.2 - 10.1\%$	1.3%	
Overall Errors	$6.3 - 32.0\%$	5.3%	

Part II.

Adsorption Energy Measurements

6. Heats of Adsorption of CO and Benzene on Pt(111)

In this chapter, the experiments of CO and benzene adsorption are described. These studies were carried out on Pt(111) single crystals to test the microcalorimeter and compare the obtained adsorption energies with data available from previous microcalorimetric work of King et al. and Campbell et al.. For this purpose CO adsorption on Pt(111) as well as benzene adsorption on Pt(111) was investigated at room temperature as a detailed function of coverage. Additionally, CO adsorption at 120 K was studied, which was not possible by single crystal adsorption calorimetry up to date.

6.1. CO Adsorption on Pt(111) at 298 and 120 K

CO adsorption on Pt(111) has persistently attracted attention in surface science because of its apparent simplicity giving access to fundamental gas-surface interaction dynamics. As a consequence, a broad spectrum of information is available in the literature. However, the understanding of the CO interaction with Pt(111) and its dynamics on the surface is not yet complete.

6.1.1. Introduction

The large amount of publications on CO adsorption process and the state of the adsorbed CO species adsorbed on Pt(111) allows only reviewing an incomplete selection of publications. The following section is focused on relevant aspects of CO interaction with Pt(111) and summarizes briefly experimental results on the sticking probability, diffusion, adsorption sites, electronic structure, order-disorder transition, adsorption energy, and the complementary theoretical studies.

Sticking Probability

The sticking probability of CO on Pt(111) was investigated by molecular beam experiments in a large range of temperatures from 90 to 500 K by the King-Wells method [43, 141–144] and by the flash filament method [145, 146] where the sticking probability is determined by the derivative of the coverage versus exposure curve. The characteristic sticking probability indicates a mobile precursor-mediated adsorption process. Initial sticking probabilities are reported in the range from 0.65 to 0.9 at room temperature [43, 141–146]. In most cases, the initial sticking probability and the saturation coverage are found to increase with decreasing temperature and is rationalized in the scope of a precursor-mediated adsorption mechanism. The effect of

the precursor state on the CO adsorption kinetics gradually decreases with increasing substrate temperature [142].

Diffusion

The mobility of chemisorbed CO on the surface was investigated as a function of temperature and coverage in order to elucidate diffusion barriers on the surface as well as intermolecular repulsive forces. A broad range of experimental methods was applied, including helium scattering [147], time-resolved infrared reflection absorption spectroscopy (IRAS) [148, 149], time-resolved high-resolution electron energy loss spectroscopy (EELS) [150–152], laser induced thermal desorption (LITD) [153–156], low energy electron microscopy (LEEM) [157] and helium-3 spin echo spectroscopy [158–160]. CO diffusion on Pt(111) follows a simple Arrhenius law over a wide temperature range, in accordance with equation 2.19. The mobility of the CO molecules on Pt(111) is reported to be about $10^{-9}\,\mathrm{cm^2 s^{-1}}$ at room temperature. Diffusion activation barriers E_{diff} are reported in the range from 131 to 521 meV, i.e. 12.6 to 50 kJ/mol.

Recent efforts by ^{3}He spin echo spectrometry revealed that the mobility of CO increases with increasing coverage up to 0.3 ML, referring to the amount of Pt surface atoms [158].

Coverage-dependent Population of Adsorption Sites

The coverage- and temperature-dependent population of adsorption sites was studied by EELS [146, 150, 161, 162], IRAS [163–166] and X-ray photoemission spectroscopy (XPS) [167]. The population of adsorption sites refers to a state of equilibrium for mobile CO molecules diffusing on the Pt(111) surface. At temperatures below $\sim 150\,\mathrm{K}$ CO was found to populate mainly on-top sites on Pt(111) up to a coverage of $\theta = 0.25\,\mathrm{ML}$, where ML refers to monolayer which is defined by the number of Pt surface atoms: $1.5 \cdot 10^{15}\,\mathrm{cm^{-2}}$. No migration from on-top sites to bridge sites was observed at this temperature. At higher coverages, bridge sites are also populated up to the saturation coverage of $\theta_{max} \approx 0.5\,\mathrm{ML}$. Elevated temperatures induce the migration of a significant fraction of the adsorbed CO molecules from on-top sites to bridge sites, already below $\theta = 0.25\,\mathrm{ML}$. Based on the temperature dependence of the site population the difference in binding energies of on-top and bridge site was determined to be 39 to 65 meV, i.e. 4 to 6 kJ/mol.

Order-Disorder Transition

The long-range order of the CO adsorbate phase on Pt(111) was investigated by LEED as a function of coverage and temperature [168–170]. At coverages θ below about 0.3 ML, a $\sqrt{3} \times \sqrt{3}/R30^\circ$ structure was observed at 300 K down to 170 K [168]. However, the broadness of the LEED spots indicated a high degree of disorder. At saturation coverage, the adsorbate structure exhibits a order-disorder transition at 270 K with a $c(4 \times 2)$ structure below 270 K. Above 270 K, the order of the adsorbate phase, determined by the maximum intensity in a (0, l/2) LEED spot of the $c(4 \times 2)$ structure, decreases exponentially with increasing temperature [170]. The $\sqrt{3} \times \sqrt{3}/R30^\circ$ structure, forming below $\theta = 0.3\,\mathrm{ML}$, is associated with the population of on-top sites [169]. Above $\theta = 0.3\,\mathrm{ML}$, the $c(4 \times 2)$ structure builds up at low enough temperatures,

populating the bridge sites. Ertl *et al.* associate the appearance of disorder with the occupation of three-fold hollow sites [168].

Influence of Adsorption on the Electronic Structure

The electronic structure of Pt(111) was investigated by XPS as a function of CO coverage [171]. The spectra of the Pt $4f_{7/2}$ core level showed a shift of about $0.40 \pm 0.05\,\mathrm{eV}$ toward lower binding for the Pt(111) surface states. The deposition of CO resulted in a shift of the Pt $4f_{7/2}$ surface core-level to higher binding energies. At saturation coverage, the shift amounts to about $1.3\,\mathrm{eV}$ with respect to the clean surface. This shift is attributed to Pt atoms that have transfered charge to chemisorbed CO molecules.

Heat of Adsorption

The heat of adsorption of CO on Pt(111) was investigated as a function of coverage by means of TDS [43, 146, 168, 172–174], equilibrium adsorption isotherms [43, 175, 176], desorption isotherms [167] and single crystal adsorption calorimetry [144]. The thermal desorption spectra showed a symmetric desorption peak at about $500\,\mathrm{K}$ for low coverages. For higher coverages, an additional shoulder appears with a desorption peak at about $450\,\mathrm{K}$. The desorption peak shifts to lower temperatures for increasing coverage, being about $380\,\mathrm{K}$ for saturation coverages. The TDS experiments reported adsorption energies in the range of 100 to $145\,\mathrm{kJ/mol}$. Consistent results in the range of 125 to $146\,\mathrm{kJ/mol}$ were obtained by equilibrium adsorption isotherms. Desorption isotherm experiments determined the adsorption energy to be $(136 \pm 10)\,\mathrm{kJ/mol}$. Direct measurement of the heat of adsorption by single crystal adsorption calorimetry reported a significantly higher adsorption energy of $(187 \pm 11)\,\mathrm{kJ/mol}$ at low coverage [25].

Theoretical Studies

Quantum mechanical calculations of the geometry and energetics of CO adsorption on Pt(111) have a long history. A first comprehensive picture was developed by Blyholder [29]. Therein, binding occurs via a charge transfer from the 5σ orbital of CO to the metal and a backdonation from the metal into the antibonding $2\pi^*$ orbital of CO. Although experimental evidence favors adsorption at low coverage at the on-top site, calculations based on density functional theory, as recently discussed at length by Feibelman *et al.* [177], consistently produced a preference for the threefold hollow sites. This discrepancy is known as the *CO adsorption puzzle*. Recently, Lazic *et al.* reported another attempt to solve the *CO adsorption puzzle* by use of a new Van der Waals-density functional of nonlocal correlation [178]. In this calculation the adsorption site was predicted in accordance with the experimental findings to be the on-top site. Obviously, the theoretical description of CO adsorption on Pt(111) is still improving and accurate experimental data are vital benchmarks to evaluate the correctness of the theoretical description.

6.1.2. Heats of Adsorption determined by Microcalorimetry

Experimental

Prior to the adsorption experiment, the ultrathin Pt(111) crystal was cleaned by several cycles of sputtering by argon ions at room temperature, followed by annealing to $\sim 1200\,\mathrm{K}$ for 5 minutes. After cleaning, the ultrathin Pt(111) was checked by LEED. Finally, the sample was flashed to $\sim 800\,\mathrm{K}$.

The applied beam intensity was $\sim 9.7 \cdot 10^{13}\,\mathrm{CO\ molecules \cdot cm^{-2} s^{-1}}$. The number of impinging molecules per pulse is calculated taking into account the pulse length of 266 ms and the beam profile area of $0.126\,\mathrm{cm}^2$. The beam pulse intensity is given by:

$$\sim 9.7 \cdot 10^{13}\,\mathrm{cm^{-2} \cdot s^{-1}} \times 0.266\,\mathrm{s} \times 0.126\,\mathrm{cm}^2 = \sim 3.2 \cdot 10^{12}$$

being the absolute amount of CO molecules impinging on the sample surface per pulse. The number of CO molecules per pulse corresponds to a fraction of 0.017 per Pt surface atom.

Results and Discussion

Energy Measurement

The amount of deposited energy by the adsorbed molecules was determined for each pulse. The deposited energy has to be divided by the number of adsorbed molecules to yield the heat of adsorption.

Figure 6.1a shows typical microcalorimeter signals for CO adsorption on Pt(111) at 298 K, during the initial adsorption phase (time $< 6\,\mathrm{s}$), and after 100 pulses (time $> 200\,\mathrm{s}$). Already without energy calibration it is obvious that the signal amplitude decreases by more than a factor of five on the saturated surface. By means of an accurate energy calibration, as described in section 5.2, the energy deposited per single molecular beam pulse, further denoted as deposited energy, can be derived from the signal amplitude. Correspondingly, figure 6.1b shows the deposited energies as a function of the pulse number at 298 (light gray data points) and 120 K (dark gray data points). To prevent misunderstanding, it should be noted again that deposited energy is not the heat of adsorption, or adsorption energy, which takes into account the number of adsorbed molecules. The data in figure 6.1a were obtained in a single measurement, whereas the energies presented in figure 6.1b are averages of six and nine independent measurements at 298 and 120 K, respectively. The error bars represent the statistical errors of the mean. At the beginning of the exposure the initial detected energy on the clean Pt(111) surface is about 500 nJ and decreases with increasing exposure. After 50 to 60 pulses the deposited energy converges to a quasi-equilibrium of about 100 nJ.

For quantitative calibration of the energy value, the adsorption signals are compared to the absorption signals induced by light pulses. Figure 6.2 shows the detector response from a typical pulse train for (i) CO molecules, (ii) laser pulses, and (iii) the absolute differences of the adsorption and the absorption signals $|I_{adsorption} - I_{absorption}|$. In both cases the length of the pulse was 266 ms. Figures 6.2a and 6.2b show calorimeter signals of adsorption on a clean Pt(111) surface and on an nearly saturated Pt(111) surface in the quasi-equilibrium, respectively. The quasi-equilibrium establishes, where the number of desorbed molecules between gas pulses balances

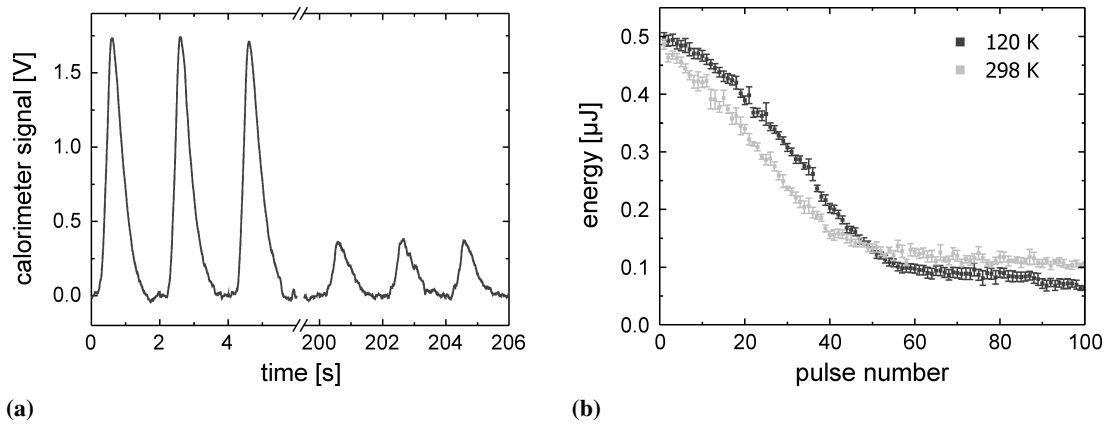

Figure 6.1.: Calorimetric measurement of CO adsorption on Pt(111) at 298 and 120 K; (a) exemplary calorimetric signals for CO adsorption at 298 K at low coverage (time < 6 s) and at high coverage (time > 200 s); (b) the derived energies deposited per single pulse at 298 and 120 K as a function of pulse number; the energies are averages of six and nine independent measurements, respectively; the error bars represent the according statistical error of the mean

the number of adsorbed molecules per pulse. The presented signals are normalized for convenient comparison of line shapes. Nearly identical line shapes of the calibration signal and the actual adsorption signal are crucial for accurate energy calibration, a condition that is reasonably fulfilled in the presented dataset. The differences of the two normalized signals, shown as (iii) in figure 6.2a and 6.2b, exhibit relative fluctuations of up to $\sim 4\%$ and $\sim 13\%$, respectively. The correspondence of adsorption and absorption signals indicate that the energy deposition by CO adsorption and by laser light absorption results in a nearly identical heat transfer to the detector.

Sticking Probability

The calculation of the heat of adsorption requires the estimation of the number of adsorbed molecules per pulse. Therefore, the sticking probability has to be determined for each pulse simultaneously. Figure 6.3a shows the mass spectrometer signal at mass 28 amu, corresponding to CO at 298 K during the initial adsorption phase (time < 6 s) and after 100 pulses (time > 200 s).

The mass spectrometer signal is used to calculate the sticking probability of CO on the sample surface via the modified King-Wells method, which is described in section 3.3. The averaged sticking probability data at 298 (six runs, light gray) and 120 K (nine runs, dark gray) are displayed in figure 6.3b as a function of pulse number. The error bars represent the according statistical errors of the mean. The initial sticking probability on the clean sample amounts to (0.710 ± 0.005) at 298 K and decreases to a constant value of (0.31 ± 0.02) after about 60 CO pulses. At 120 K, the initial sticking probability is slightly higher, at (0.722 ± 0.003), and stays systematically higher with increasing coverage than the sticking probability at 298 K. Finally, the sticking probability at 120 K converges to a constant value of (0.28 ± 0.01) after about 60

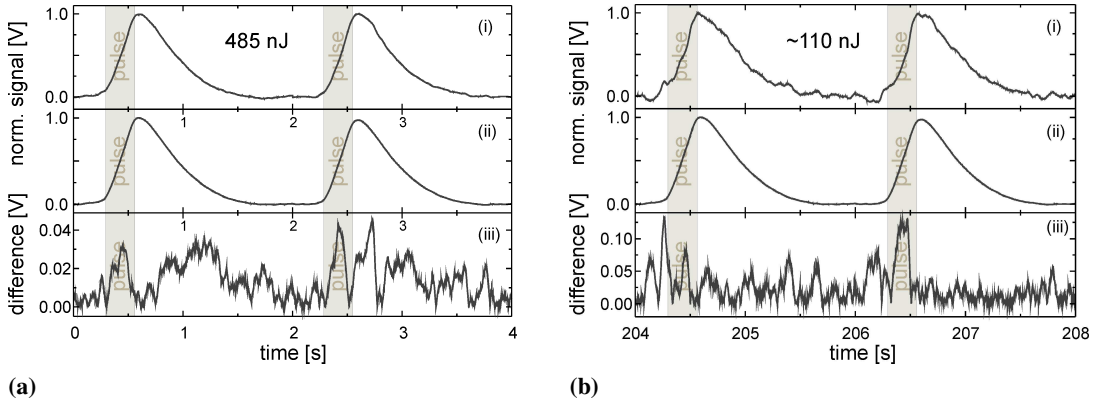

Figure 6.2.: Comparison of the normalized signals for (i) CO adsorption and (ii) laser light absorption; the absolute difference plot (iii) shows relative fluctuations up to 4% for (a) the initial adsorption (deposited energy $485\,\mathrm{nJ}$) and fluctuations up to 13% for (b) the adsorption at the quasi-equilibrium (deposited energy $\sim 110\,\mathrm{nJ}$)

CO pulses. The absolute value of the CO sticking coefficient in the high-coverage regime is subject to larger systematic error since the absolute number of adsorbing molecules is small. Consequently, the nominator, i.e. the QMS intensity of the scattered fraction of the molecular beam pulse, and denominator, i.e. the QMS intensity of the fully scattered molecular beam pulse, in equation 3.3 are close and more sensitive to deviations of the denominator from the true value than at conditions where the denominator is much larger than the nominator. Accordingly, the determination of high sticking probabilities is less affected by this problem. However, the determined low sticking probabilities at high coverage coincides quite well for both measured temperatures. The sticking coefficient allows to calculate the absolute number of CO molecules that are adsorbed on the surface per single pulse. The CO coverage on the surface can be calculated by integration of the number of CO molecules adsorbed per pulse. Figure 6.4a shows the sticking probabilities at 298 and 120 K as a function of CO surface coverage. Initially, the sticking probabilities at 120 and 298 K are very similar. However, for increasing CO coverages the sticking probabilities at 120 K lies systematically higher than at 298 K. Particularly for coverages of 0.2 to $0.4 \times 1.5 \cdot 10^{15}\,\mathrm{cm}^{-2}$, the deviation ranges from 6 to 13%. The coverages, where the quasi-equilibrium establishes in the sticking probability, are very close for both temperatures, around $0.5 \times 1.5 \cdot 10^{15}\,\mathrm{cm}^{-2}$

The coverage dependence of the sticking probability indicates precursor mediated adsorption at 298 and 120 K. The higher sticking probability at the lower temperature can be rationalized on the basis of a longer life-time of the mobile precursor state at low temperature. This enables the precursor to reside longer in the vicinity of the surface and to probe larger numbers of surface sites to find the site where it can adsorb. The adsorption-desorption equilibrium is reached at a CO coverage of $\sim 7.0 \cdot 10^{14}\,\mathrm{cm}^{-2}$ and $\sim 8.2 \cdot 10^{14}\,\mathrm{cm}^{-2}$ at 298 and 120 K, respectively. The observation of an increased saturation coverage with decreasing temperature is in agreement

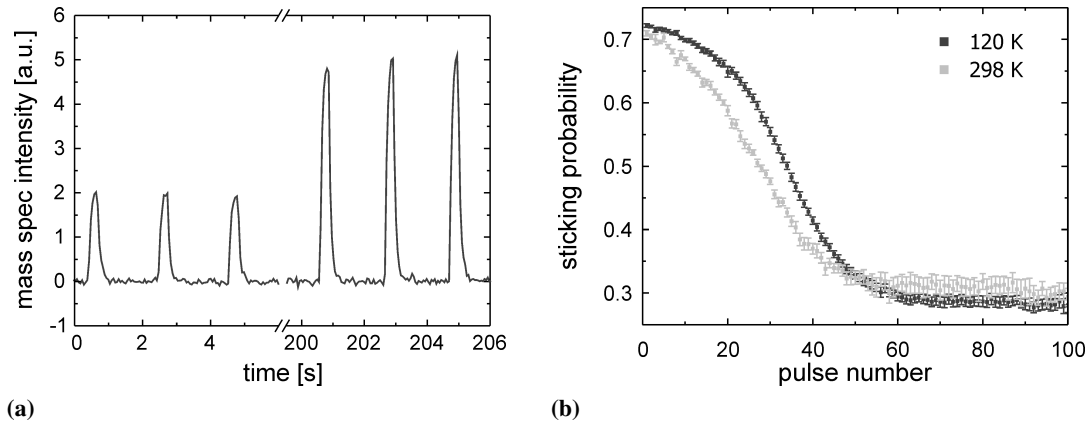

Figure 6.3.: (a) Mass spectrometer signal of the gas pulses during the adsorption experiment at low (left hand side) and at high coverage (right hand side) and (b) the resulting sticking probability as a function of pulse number at 298 K (light gray) and 120 K (dark gray); the sticking probabilities are averages of six and nine independent measurements for 298 K and 120 K, respectively; the error bars represent the statistical error of the mean

with previously reported studies [142, 143]. Liu *et al.* explained the excess at low temperatures by "some extra CO adsorbed weakly on the surface after saturation" [143].

For CO adsorption, there is no classical saturation regime in the sticking probability using pulsed molecular beams and the sticking probability never becomes zero. This observation can be explained by a dynamic adsorption-desorption equilibrium. This equilibrium can be rationalized by the previously reported pressure dependence of the saturation coverage of CO on Pt(111) [179]. The pressure on the surface changes from 10^{-6} mbar, while the molecular beam impinges on the surface, to 10^{-10} mbar during the time when the molecular beam is interrupted. Therefore, CO molecules are likely to desorb between molecular beam pulses and a small fraction of CO adsorbs again after resuming of the molecular beam.

Heat of Adsorption

By dividing the measured energy input by the absolute number of adsorbed molecules the heat of adsorption was obtained at 298 and 120 K.

Using a surface temperature that is different from the molecular beam source has an impact on the measured adsorption energy E_{ads}. The internal energy E_{int} of the impinging molecules is not in equilibrium with the surface. The adsorbed fraction of the molecular beam pulse N_{ads} equilibrates with the surface and adds an additional energy ΔE_1:

$$\Delta E_1 = N_{ads} \cdot \Delta E_{int} \tag{6.1}$$

A fraction of the deflected (non-sticking) molecules N_{sca} can also partially or fully equilibrate with the surface, if the molecules were inelastically scattered or adsorbed in short-living trapped

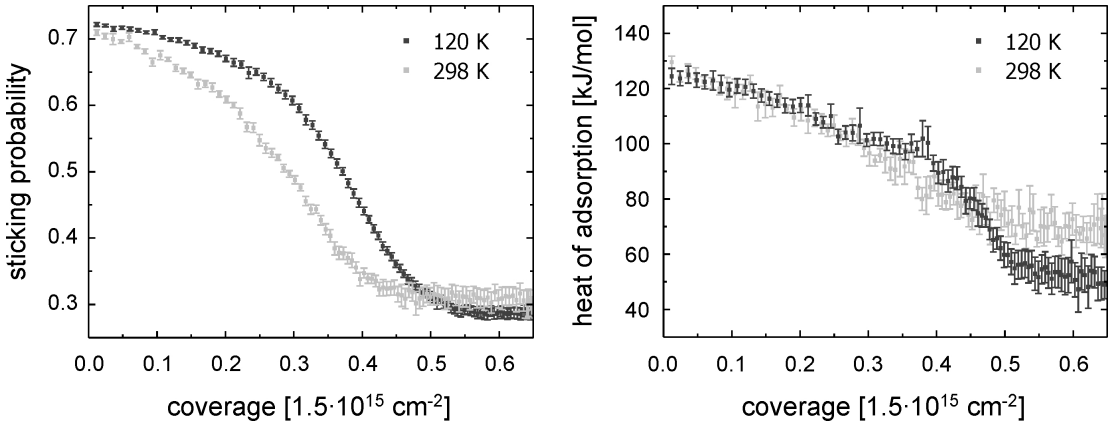

Figure 6.4.: (a) Sticking probability and (b) Heat of adsorption plotted as a function of coverage. The data at 298 (light gray) and at 120 K (dark gray) are averages of six and nine independent, respectively; the error bars represent the according statistical error of the mean

states, correspondingly [180, 181]. Here, not only the internal energy is affected but also the average kinetic energy E_{kin} after the scattering process:

$$\Delta E_2 = N_{sca}(\alpha_1 \Delta E_{int} + \alpha_2 \Delta E_{kin}), \tag{6.2}$$

where α_1 and α_2 specify the efficiencies of the according equilibration processes. An upper limit for the change in the internal energy ΔE_{int} can be estimated by the specific heat capacity of $29.1\,\frac{\mathrm{J}}{\mathrm{mol\cdot K}}$ for CO in the gas phase, corresponding to about $0.3\,\mathrm{meV/K}$ per molecule [182]. Therefore, the expected additional energy input is about $0.06\,\mathrm{eV}$ per molecule. These contributions to the adsorption energy will be accounted for in the calculation of the heat of adsorption at 120 K. Assuming that the internal energies of all impinging molecules, implying $\alpha_1 = 1$, equilibrate to the surface temperature of 120 K yields an additional contribution of at most $6\,\mathrm{kJ/mol}$ to the determined adsorption heats. Further, assuming that also the kinetic energy of all deflected CO molecules, implying $\alpha_2 = 1$, equilibrates to the surface temperature adds about 15 meV per molecule, or at most $2\,\mathrm{kJ/mol}$, to the heat of adsorption.

Figure 6.4b depicts the heat of adsorption as a function of coverage at 120 K and 298 K. The coverage dependence of the heats of adsorption show monotonous, almost linear, declines with a steeper decline for CO coverages higher than about 0.35 to 0.4 ML. Finally, a quasi-equilibrium is established at a coverage of about 0.5 ML.

The possible physical reasons for the decreasing adsorption energy with increasing coverage are (i) the change of the surface's electronic structure by the adsorbate and the related competition for the *d* electrons as well as (ii) intermolecular repulsion between the adsorbates via dipole-dipole interactions. The adsorption heats converge in an adsorption-desorption equilibrium as a result of a pressure dependence of the saturation coverage. Consequently, some

adsorbates desorb between molecular beam pulses and a steady state is establishes, in which the adsorption during a gas pulse exactly balances the desorption between gas pulses. Similar adsorption-desorption equilibria were reported by previous microcalorimetric studies on single crystal surfaces [84, 117].

The initial heats of adsorption determined at 120 K and 298 K were found to coincide within the error margins, being (124 ± 3) kJ/mol and (130 ± 3) kJ/mol, respectively. Further, the heats of adsorption coincide markedly well up to a coverage of 0.3 ML (referring to $1.5 \cdot 10^{15}$ cm^{-2}). The mean difference of the heats of adsorption is zero and has a standard deviation of 3 kJ/mol, which matches with the variations of the initial heats of adsorption. At coverages from 0.3 to 0.45 ML, the heat of adsorption at 120 K is systematically higher than at 298 K. On average, the adsorption heat at 120 K exceeds the room temperature adsorption heat by about 6 to 8 kJ/mol. However, in a coverage region between 0.37 to 0.39 ML, this excess rises to 14 to 22 kJ/mol. In the adsorption-desorption equilibrium the heats of adsorption are (70 ± 7) kJ/mol at 298 K and (59 ± 5) kJ/mol at 120 K being similar within the error margins. It should be noted here that the heat of adsorption in the adsorption-desorption equilibrium suffers from a low signal-to-noise ratio, as can be seen by the larger error margins.

The determined initial heats of adsorption at 298 K of (130 ± 3) kJ/mol is in good agreement with previously reported values of 100 to 146 kJ/mol obtained by TDS, equilibrium adsorption isotherms and desorption isotherms. Only the previously reported value by single crystal adsorption calorimetry is significantly higher, being (187 ± 11) kJ/mol [25]. The apparent discrepancy can be attributed to the data evaluation. King *et al.* used a reflectivity r of 0.66 to calculate the heat of adsorption on Pt(111) [25], instead of 0.73 as determined in this work by the in situ reflectivity measurement setup. Consequently the derived heat of adsorption by King *et al.* is scaled by the absorptivity $a_r = 1 - r$. For a proper comparison, the absolute value of the heat of adsorption can be corrected by multiplication with the appropriate ratio of absorptivities:

$$\frac{a_{r=0.73}}{a_{r=0.66}} = \frac{1 - 0.7303}{1 - 0.66} = 0.792$$

Scaling the initial heat of adsorption derived by King *et al.* by this correction factor yields:

$$0.792 \times (187 \pm 11)\,\text{kJ/mol} = (149 \pm 9)\,\text{kJ/mol}$$

resulting in a better agreement of the microcalorimeter experiments and previous, indirectly derived heats of adsorption and the here determined value.

The observed difference in the heat of adsorption at coverages between 0.3 and 0.45 ML may be rationalized on the basis of previous studies on CO adsorption on Pt(111). The enhanced heat of adsorption at 120 K at coverages from 0.3 to 0.45 ML may be caused by the difference in the order of the adsorbate layer. At 120 K, an ordered c(2x4) phase is formed in contrast to an unordered adsorbate phase at 298 K [168]. The ordered phase can have a lower free energy and can release a higher amount of heat into the surface as compared to the unordered phase.

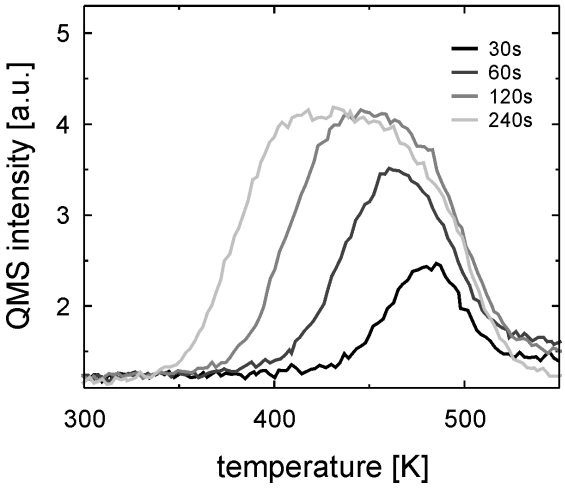

Figure 6.5: CO/Pt(111) TDS spectra obtained as a function of coverage with a temperature ramp of $5\,\mathrm{K/s}$ at mass $28\,\mathrm{amu}$. The coverage was varied by the CO exposure time ranging from 30 to $240\,\mathrm{s}$. The onset of the desorption signals shifts to lower temperature with increasing coverage. For the smallest coverage, the temperature of the desorption peak is about $485\,\mathrm{K}$.

6.1.3. Determination of the Desorption Energy by TDS

CO adsorption on Pt(111) is a reversible process. Therefore TDS can be applied to determine the adsorption energy. TDS experiments with different coverages were performed in the preparation chamber. The clean Pt(111) surface was exposed to CO by the gas doser in front of the $1\,\mathrm{mm}$ thick sample. The coverage was varied by the exposure time in a range from 30 to $240\,\mathrm{s}$. During TDS experiments, the desorption was monitored by QMS at a mass of $28\,\mathrm{amu}$ with a temperature ramp gradient of $5\,\mathrm{K/s}$.

Figure 6.5 shows the desorption traces obtained for different CO coverages on Pt(111). The onset of the desorption signals shifts to lower temperature with increasing coverage. For the smallest investigated coverage, the temperature of the desorption peak is about $485\,\mathrm{K}$. The shift of the onset indicates a decreasing heat of adsorption with increasing coverage which is in qualitative agreement with the dependency of the heats of adsorption on the surface coverage obtained by adsorption microcalorimetry. By Redhead analysis the desorption energy can be estimated using the desorption peak temperature of the TDS data with the smallest coverage, see equation 3.5. The frequency factor ν is assumed to be $10^{13}\,\mathrm{s}^{-1}$. The resulting desorption energy is $124\,\mathrm{kJ/mol}$ for a peak temperature of $485\,\mathrm{K}$. The coverage for the $30\,\mathrm{s}$ is not known in absolute terms and could be lower. Eventually, a lower coverage would result in a further shift of the desorption peak temperature. The desorption peak temperature in the low coverage limit will always be lower than the temperature where the desorption signals reach the background pressure level. This temperature, where the background pressure level is reached, is convoluted with the pumping speed of the chamber. However, the estimation of an upper limit of the desorption energy is possible. The according upper limit of a desorption peak temperature of the data shown in figure 6.5 is about $520\,\mathrm{K}$. Consequently, an upper limit of the desorption energy is estimated to be $133\,\mathrm{kJ/mol}$. The desorption energy at the lowest coverage, $124\,\mathrm{kJ/mol}$, is close to the initial heat of adsorption of $(130 \pm 3)\,\mathrm{kJ/mol}$, which was obtained by adsorption microcalorimetry at $298\,\mathrm{K}$. Also the upper limit of the desorption energy, $133\,\mathrm{kJ/mol}$, is in agreement with the

calorimetrically determined heat in the low coverage regime.

6.2. Benzene Adsorption on Pt(111) at 298 K

Benzene adsorption on Pt(111) was extensively studied since this adsorption system represents the simplest case of the interaction of an aromatic hydrocarbon with the well-defined Pt(111) single crystal surface.

Adsorption energy measurements so far suffered from a serious constraint. At elevated temperatures and low coverage, benzene adsorbed on Pt(111) can decompose [183, 184]. Therefore, desorption-based methods such as TDS, molecular beam relaxation spectroscopy and equilibrium adsorption isotherms cannot be applied at low coverage. Even at higher coverages, where a fraction of adsorbed molecules desorbs intact, the TDS and molecular beam relaxation spectroscopy line shapes are likely complicated by the competition of desorption and dissociation. This effect strongly complicates the data analysis and precludes the accurate evaluation of desorption energies. Even at saturation coverages, only 45% of the adsorbed benzene desorbs intact [185], whereas the remaining benzene dehydrogenates rendering impossible also the use of equilibrium adsorption isotherms. Consequently, the adsorption energy of benzene on clean Pt(111) can only be assessed accurately by microcalorimetry. In the perspective of this experiment benzene, as a low vapor pressure substance, serves for the verification of the capability of the experimental setup to measure the heat of adsorption for larger molecules.

6.2.1. Introduction

Previously reported results on benzene adsorption on Pt(111) are briefly reviewed below.

Sticking Probability

The sticking probability of benzene on Pt(111) was measured by means of the King-Wells-method at 200 K by Xu *et al.* [186] and at 300 K by Ihm *et al.* [117]. Similar initial sticking probabilities were reported in both studies, stating values of 0.95 to 0.98. The sticking probability was found to remain constant with increasing coverage up to saturation of the Pt(111) surface, indicating a very mobile precursor state. Assuming that benzene is bound parallel to the surface, with a van der Waals radius of 7.2 Å, the saturation was estimated to correspond to about 0.9 carbon atoms per Pt surface atom, yielding $2.25 \cdot 10^{14}$ benzene molecules cm^{-2} [183]. Abon *et al.* determined the value for the saturation coverage to be $1.7 \cdot 10^{14}$ benzene molecules cm^{-2} by combination of AES and TDS [184].

Diffusion

Surface diffusion has not been investigated in detail yet. Only a low temperature scanning probe microscopy (STM) study exists [187]. From the distribution of molecules on the surface it was concluded that benzene hops only a few lattice sites before having lost all its momentum parallel to the surface at 4 K.

Coverage-dependent Population of Adsorption Sites

Structural information on the benzene/Pt(111) system was obtained by EELS [184], a diffuse LEED study [188], angle resolved photoemission spectroscopy (ARUPS) [189], near-edge X-ray absorption fine structure (NEXAFS) [190] and STM [187]. The symmetry of the benzene molecules was found to be distorted on the Pt(111) surface by ARUPS [189]. Contradicting reports about a change in the C-C bond lengths exist. A diffuse LEED study found that the C-C bond lengths become unequal upon adsorption, going from 1.397 Å to bond lengths of 1.45 ± 0.10 and 1.63 ± 0.10 Å[188]. This finding contrasts with an equal bond length of 1.40 ± 0.02 Å of adsorbed benzene, determined by NEXAFS [190]. Vibrational spectroscopy could not find significant evidence for different adsorption sites at temperatures between 200 and 300 K [184]. The polarization dependence of the π^* and σ^* resonances in the monolayer coverage spectra showed that benzene lies flat on Pt(111). This finding was later confirmed by STM, where three distinct types of images for isolated benzene molecules could be resolved. These sites are assigned to two stable sites, bridge and hollow, and a less stable on-top site, by theoretical calculations [191]. The preferred binding site of benzene on Pt(111) remains under debate.

Influence of Adsorption on the Electronic Structure

The work function change of Pt(111) upon benzene adsorption was investigated by a contact potential difference study [184]. With increasing coverage Abon *et al.* found a decreasing work function with a difference of up to $\Delta\phi = -1.52\,\mathrm{eV}$ at saturation.

Adsorption Energy

The adsorption energy of benzene on Pt(111) was investigated as a function of coverage by TDS [183–186, 192] and microcalorimetry [117]. The TDS studies monitored the molecular desorption of benzene. Multilayer desorption was found at $\sim 190\,\mathrm{K}$. Molecular desorption at high benzene coverage starts at 250 to 350 K. The desorption peaks were observed (i) at $\sim 500\,\mathrm{K}$ for low coverage and (ii) at ~ 310 to $\sim 400\,\mathrm{K}$ with a shoulder 100 K above the desorption peak temperature for high coverage. Recently, the TDS data was compiled by Ihm *et al.* and partly analyzed by means of a Redhead analysis, assuming a frequency factor of $10^{13}\,\mathrm{s}^{-1}$ [117]. The estimated adsorption energies range from 121 to 133 kJ/mol. By single crystal adsorption microcalorimetry an initial heat of adsorption of 197 kJ/mol was found at room temperature [117]. Close to the saturation of the surface an adsorption-desorption equilibrium was reported, similar to the CO adsorption experiments, which is described in section 6.1. The heat of adsorption in the adsorption-desorption equilibrium regime was determined to be $(68 \pm 5)\,\mathrm{kJ/mol}$.

Theoretical Studies

A density functional theory calculation exists for benzene on Pt(111) by Saeys *et al.* [193]. The preferred adsorption site at low coverage was determined to be the bridge site with an adsorption energy of 117 kJ/mol. The molecule's second important site was found to be the hollow site with an adsorption energy of 75 kJ/mol.

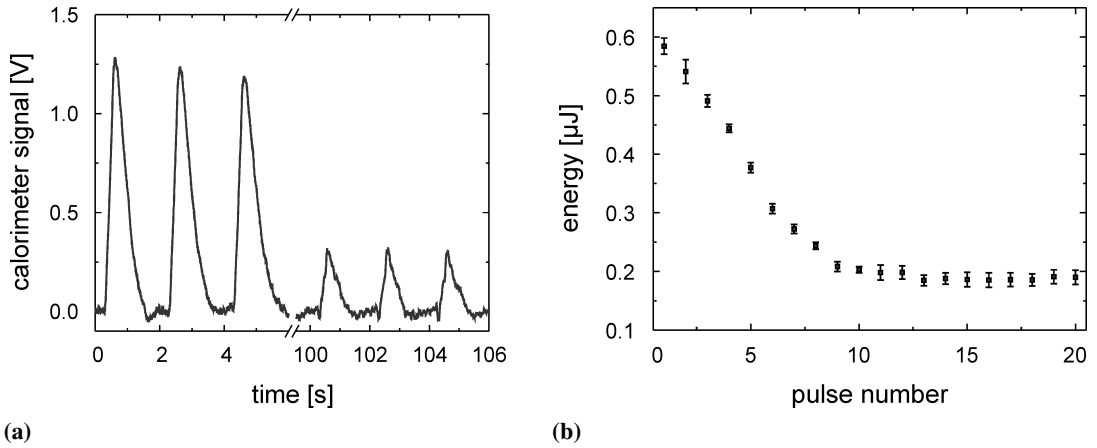

Figure 6.6.: Calorimetric measurement of benzene adsorption on Pt(111) at 298 K; (a) exemplary calorimetric signals for CO adsorption at 298 K at low coverage (time < 6 s) and at high coverage (time > 100 s); (b) the deposited energies for each pulse at 298 K as a function of pulse number; the energies are averages of five independent measurements; the error bars represent the according statistical error of the mean

6.2.2. Heat of Adsorption determined by Microcalorimetry

Experimental

Prior to the adsorption experiment the ultrathin Pt(111) crystal was cleaned by several cycles of sputtering by argon ions at room temperature followed by annealing to ~ 1200 K for 5 minutes. Additionally, in order to remove carbonaceous deposits from the surface, the sample was kept at elevated temperatures around 600 K in oxygen atmosphere of 10^{-6} mbar. After cleaning the ultrathin Pt(111) was checked by LEED. Finally, the sample was flashed to ~ 800 K.

The total applied beam intensity was $\sim 1.1 \cdot 10^{14}$ benzene molecules $\mathrm{cm}^{-2}\mathrm{s}^{-1}$. The number of impinging molecules per pulse is calculated with the pulse length of 266 ms and the beam profile area of $0.126\,\mathrm{cm}^{-2}$:

$$\sim 1.1 \cdot 10^{14}\,\mathrm{cm}^{-2}\mathrm{s}^{-1} \times 0.266\,\mathrm{s} \times 0.126\,\mathrm{cm}^{-2} = \sim 3.6 \cdot 10^{12}$$

The number of benzene molecules per pulse corresponds to a fraction of 0.019 per Pt surface atom.

Results and Discussion

Energy Measurement

Figure 6.6a shows a typical microcalorimeter signal for benzene adsorption on Pt(111). The calorimeter signal during the initial adsorption phase and near the saturation coverage are depicted on the left-hand side ($t < 6$ s) and the right-hand side ($t > 100$ s), respectively. Figure 6.6b

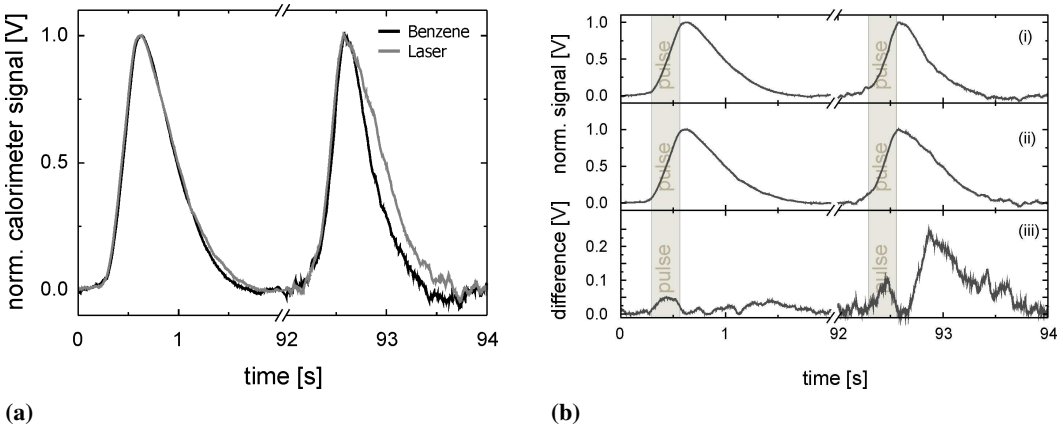

Figure 6.7.: Comparison of the normalized calorimeter signals for benzene adsorption; (a) shows the normalized calorimeter's adsorption signal at low (time: 0 to 2 s, deposited energy: about 600 nJ) and high coverage (time: 92 to 94 s, deposited energy: about 180 nJ). The adsorption signals are superimposed with normalized laser absorption signals corresponding to deposited energies of 760 nJ and 184 nJ. At low coverage the adsorption and absorption signals coincide, whereas a significant difference is present at high coverage; (b) shows (i) the normalized adsorption signals at high and low coverage and (ii) the respective normalized laser light absorption of 760 nJ and 184 nJ and (iii) the absolute difference of (i) and (ii); the absolute difference plot shows random fluctuations up to 5% for the initial adsorption and a significant deviation of the signal shape at high coverage. This deviation of up to 24% indicates an additional energy dissipation mechanism as compared to the laser absorption.

presents the derived energies released per applied pulse as a function of the pulse number. The energies were calculated by the same procedure as described in section 6.1.2. The data in figure 6.6a were obtained in a single measurement; the energies presented in figure 6.6b are an average of five measurements where the error bars represent the statistical errors of the mean. At the beginning of the exposure the initial detected energy on the clean Pt(111) surface is about 600 nJ and decreases with increasing pulse number. After 10 pulses the deposited energy converges to a quasi-equilibrium value of about 200 nJ.

The line shape of the adsorption signals of benzene at low and high coverage were compared to line shape of the laser light absorption. Figure 6.7a shows the superposition of normalized laser light absorption signals and benzene adsorption signals at low and at high benzene coverage on the left hand and right hand side, respectively. The adsorption signal at low coverage nearly coincides with the laser calibration signal whereas at high coverage the adsorption signal shows a significant difference from the calibration signal. This difference is more obviously seen in figure 6.7b which shows the absolute difference $|I_{adsorption} - I_{absorption}|$ of the normalized signals. Fluctuations up to 5% for the initial adsorption signal and up to 24% for the adsorption-desorption equilibrium signal are present. The difference of 24% at high coverage is specifically present after the molecular beam pulse ended, indicating an enhanced energy dissipation as

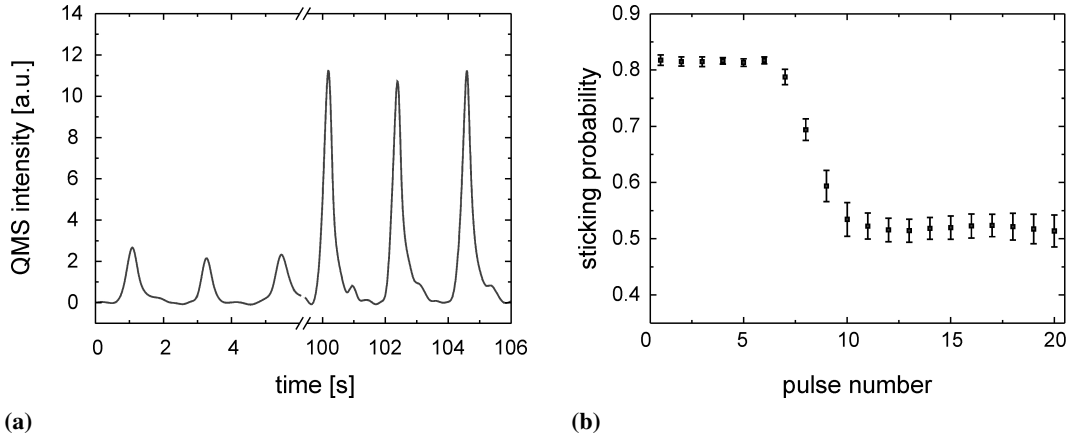

Figure 6.8.: Sticking probability measurement for Benzene on Pt(111); (a) shows the QMS signal for the adsorption on initially clean Pt(111) (time $< 6\,\mathrm{s}$) and in the adsorption desorption equilibrium (time $> 100\,\mathrm{s}$; (b) the derived sticking probabilities are shown as a function of pulse number

compared to laser light absorption. This observation can be explained by desorption of benzene molecules, which can carry away a fraction of the energy deposited during the benzene pulse. This effect was already reported by Ihm *et al.* [117], ascribing a transiently adsorbed state to this process. TDS studies showed benzene desorption to start at temperatures between 290 and 310 K at high coverage. Consequently, the energy may dissipate by desorption. Further, a pressure dependent transiently adsorbed state of benzene was reported by Lee *et al.*, though not on Pt(111) but on Pd(111). Their NEXAFS study of benzene on Pd(111) revealed that going beyond the saturation coverage, where the C/Pd ratio is ~ 1, results in the formation of a tilted benzene species which is only stable at elevated pressure, $\sim 5 \cdot 10^{-8}$ mbar, even at temperatures as low as 100 K [194]. Subsequent evacuation resulted in immediate disappearance of $\sim 75\%$ of the tilted benzene species. In the work here presented, pressures of about $4 \cdot 10^{-7}$ mbar were produced on the surface during benzene adsorption. Therefore, not only desorption but also pressure dependent population of adsorption states may contribute to the observed energy dissipation after the molecular beam pulse ended. However, the derived energies should not be affected, as the energy dissipation takes place only after the molecular beam was interrupted. Therefore, the energy dissipation was not accounted for in the energy determination.

Sticking Probability

Figure 6.8a shows the time evolution of the mass spectrometer signal at the mass 76 amu, corresponding to the mass of benzene molecules, which was recorded simultaneously with the calorimetric measurement.

This trace is used to calculate the sticking probability of benzene on the sample surface via the modified King-Wells method described in section 3.3. The derived sticking probabilities are displayed in figure 6.8b as a function of the pulse number. The coverage increments can

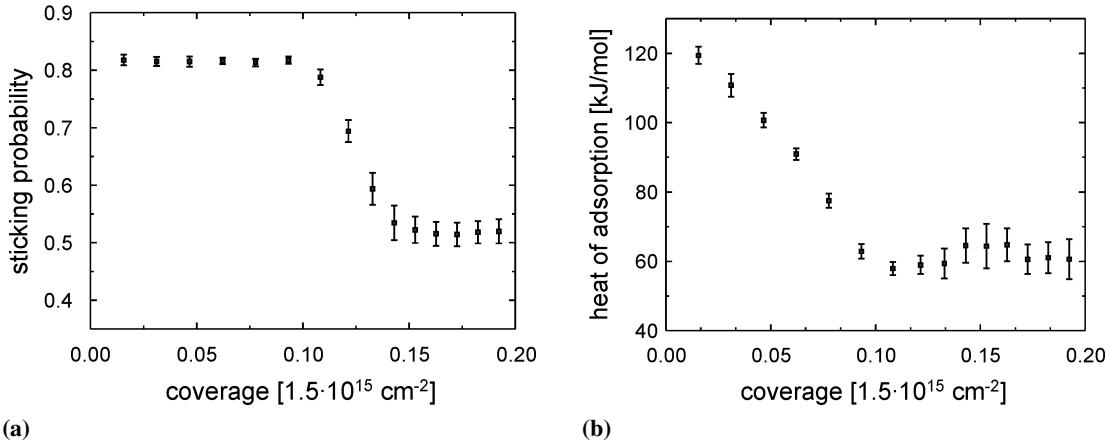

Figure 6.9.: (a) The sticking probability and (b) heat of adsorption of benzene on Pt(111) plotted as a function of coverage; the sticking probability and the heat of adsorption are averages of five independent measurements; the error bars show the according statistical error of the mean

be calculated by multiplying the coverage dependent sticking probability and the number of molecules per pulse and the total coverage was calculated by integration of the coverage increments. Desorption between pulses, which was observed at high coverages, was not accounted for. Figure 6.9a shows the sticking probability as a function of the accumulated coverage. The sticking probability is initially constant, being (0.82 ± 0.01), and starts to decrease at a benzene coverage of $1.5 \cdot 10^{14}\,\mathrm{cm}^{-2}$. An adsorption-desorption equilibrium establishes after about 11 benzene pulses at a coverage of $2.25 \cdot 10^{14}\,\mathrm{cm}^{-2}$, where the sticking probability is (0.50 ± 0.03). The coverage dependence of the sticking probability shown in figure 6.9a exhibits a plateau nearly until the saturation coverage is reached, evidencing a mobile precursor-mediated adsorption. The initial sticking probability here obtained is significantly lower than previously reported values of the initial sticking probability of 0.95 to 0.98 [117, 186]. However, the coverage dependency of the sticking probability is in qualitative agreement with previous studies. Also the coverage where the adsorption-desorption equilibrium is established is in good agreement with the reported value of $2.3 \cdot 10^{14}\,\mathrm{cm}^{-2}$ for the saturation coverage, assuming a carbon-to-platinum atom ratio of 0.9 [117].

Heat of Adsorption

The heat of adsorption was derived from the determined deposited energy and the according number of adsorbed molecules per pulse. Figure 6.9b shows the heat of adsorption of benzene on Pt(111) as a function of coverage. The measured initial adsorption heat amounts to initially $(119 \pm 3)\,\mathrm{kJ/mol}$ at 298 K, which continuously decreases nearly linearly to a constant value of $61\,\mathrm{kJ/mol}$, which was reached at a benzene coverage of about $1.5 \cdot 10^{14}\,\mathrm{cm}^{-2}$.

The decreasing heat of adsorption with increasing coverage may be explained by three contributions: (i) a change of the surface's electronic structure, (ii) repulsive lateral interactions

between the adsorbed benzene molecules and (iii) adsorbed species that depend on the surface coverage, i.e. different adsorption sites and possible tilting of the benzene at high coverage, as found for instance on Pd(111) [194].

Previously, the heat of adsorption was studied by adsorption microcalorimetry. The calorimetric study by Ihm *et al.* determined a value of 197 kJ/mol for the initial heat of adsorption. The significantly higher initial adsorption energy of 197 kJ/mol reported by Ihm *et al.* is difficult to rationalize. The magnitude in the difference can not be understood by the stated systematic errors and may point to the necessity to put more effort into the precise analysis of systematic errors.

6.3. Conclusion

First adsorption measurements were performed on a Pt(111) single crystal. The determined energetics of CO adsorption and benzene adsorption coincide well with heats of adsorption determined by indirect methods.

CO Adsorption on Pt(111)

The heat of adsorption for CO on Pt(111) was determined as a detailed function of coverage at 298 K and for the first time below room temperature, at 120 K. The heat of adsorption at 120 K was compared to the heat of adsorption at 298 K and also to the indirectly determined adsorption energies by thermal desorption spectroscopy. A series of six and nine independent CO adsorption experiments were performed on freshly cleaned Pt(111) at 298 K and 120 K, respectively. The heat of adsorption was derived from the simultaneous measurement of the deposited energy and the sticking probability. Initial sticking probabilities were determined, being (0.710 ± 0.005) at 298 K and (0.722 ± 0.003) at 120 K. These values coincide with the range of previously reported initial sticking probabilities of 0.65 to 0.9. The observed calorimeter signals for CO adsorption and laser light absorption are similar in shape, indicating a similar heat input and dissipation.

Initial adsorption energies were found between (130 ± 3) and (124 ± 3) kJ/mol by microcalorimetry at 298 K and 120 K, respectively. Up to a coverage of about 0.30 ML the adsorption heats coincide very well. However, at CO coverages between from 0.3 to 0.45 ML a small difference in the heats of adsorption at 298 and 120 K was observed. The low temperature adsorption energy exceeds the room temperature adsorption heat by about 6 to 8 kJ/mol on average with a stronger excess of 14 to 22 kJ/mol between 0.37 to 0.39 ML, referring to the number of Pt surface atoms. The excess may be relate to the temperature induced order-disorder transition. The onset of an adsorption-desorption equilibrium, evident by the development of a constant heat of adsorption, coincides with the expected saturation coverage of about 0.5 ML.

For thermal desorption spectroscopy the Pt(111) was precovered with various CO coverages. The initial adsorption energies at 298 and 120 K coincide with the desorption energy derived by Redhead analysis from the TDS data (124 to 133 kJ/mol). Other studies also reported initial adsorption heats between 100 and 146 kJ/mol. Previously, the heat of adsorption was determined by radiative single crystal adsorption calorimetry at room temperature. The reported

adsorption energy of $(187 \pm 11)\,\mathrm{kJ/mol}$ is significantly higher than the here derived value of $(130 \pm 3)\,\mathrm{kJ/mol}$. The higher adsorption energy is probably biased by a wrong reflectivity value for Pt(111) of 0.66 in this study instead of 0.73 as determined in the present work. Correcting the reflectivity yields $(149 \pm 9)\,\mathrm{kJ/mol}$.

The adsorption energy was determined to decrease with increasing coverage. This observation is in agreement with TDS results for different coverages. where the desorption peak temperature decreased with increasing CO coverage.

Benzene Adsorption on Pt(111)

The heat of adsorption of benzene on Pt(111) was determined as a function of coverage at 298 K. Five independent benzene adsorption experiments were performed on freshly cleaned Pt(111). The observed line shapes of the calorimeter signals for benzene adsorption and laser light absorption are compatible at low coverages. However, near the saturation coverage, the line shapes are different, indicating that the deposited energy dissipates faster after the molecular beam was interrupted due to partial benzene desorption.

The derived initial sticking probability of (0.82 ± 0.01) is lower than previously reported values laying between 0.95 and 0.98. However, the coverage dependency of the sticking probability is in qualitative agreement with the previous measurements. The initial heat of adsorption is $(119 \pm 3)\,\mathrm{kJ/mol}$. A significantly higher value of $197\,\mathrm{kJ/mol}$ was reported by microcalorimetry. The magnitude in the difference can not be understood by the stated systematics.

The onset of an adsorption-desorption equilibrium, evident by the development of a constant heat of adsorption, is present at a coverage of $2.25 \cdot 10^{14}\,\mathrm{cm}^{-2}$. The latter value is in good agreement with the previously reported value of $2.3 \cdot 10^{14}\,\mathrm{cm}^{-2}$ for the saturation coverage.

Concluding, the first measurements with CO and benzene on Pt(111) single crystals verified the correct operation of the new UHV microcalorimeter experiment. Sticking probabilities were obtained as a detailed function of coverage. The adsorption heats are in good agreement with values reported previously by indirect methods and lower than results obtained by the other two single crystal adsorption microcalorimeters.

7. Size Dependent Heat of Adsorption for CO on Pd Particles supported on Iron Oxide

The completed and properly working adsorption calorimeter experiments enables the determination of adsorption energies on supported model catalysts. In this chapter, the study of the heat of adsorption for CO on Fe_3O_4 supported Pd model catalyst is described. The interaction energetics was investigated as a function of mean particle size and a pronounced correlation was observed.

The energetics of interaction of gaseous molecules, particularly carbon monoxide, with well-defined metal nanoparticles were previously addressed indirectly in non-isothermal TDS experiments [22] and in isothermal modulated molecular beam studies [21], where the adsorption energies were obtained by modeling the desorption process. However, these indirect methods did not provide a clear trend in the changes of the adsorption energy with particle size, the TDS studies found a decrease of the adsorption energy by about 10 kJ/mol on the 2.5 nm sized Pd particles as compared to extended single crystal surface, whereas the kinetic model used for analysis of the molecular beam experiments predicted a pronounced increase of the adsorption energy by about 35 kJ/mol on particles smaller than 4 nm. A detailed introduction to CO adsorption on oxide supported Pd particles will be given in section 7.2.1.

For the first time, the new UHV microcalorimeter experiment enables the direct determination of the heats of adsorption for CO as a function of Pd particle size. The model surfaces employed in this study consist of Pd nanoparticles supported on a well-ordered thin Fe_3O_4 film, which was grown on an ultrathin Pt(111) single crystal. Additionally, CO adsorption on Pd(111) was studied as a reference for the majority of (111) facets present on the nanoparticles.

7.1. Pd Particles on Fe_3O_4/Pt(111): Properties and Preparation

Thin well-ordered oxide films on metal substrates form the basis of oxide supported model catalysts [8, 195, 196]. Epitaxially grown, they provide atomically flat and well-defined surfaces. The advantage of using thin oxide films grown on metal substrates is that the electrons can still tunnel to the metal substrate due to the limited thicknesses of the isolating oxide film. therefore, all kinds of surface science techniques involving electrons — such as LEED, STM, photoelectron spectroscopy and high resolution EELS — can be applied to characterize the morphological and electronic structure of the model catalysts in great detail.

The interaction of the oxide film and the deposited metal is important for the growth and nucleation of the particles [196]. If the metal-support interaction is strong, the shape of the particles, and possibly their electronic structure, maybe affected.

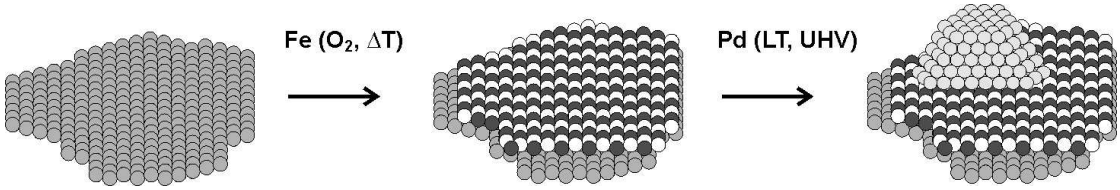

Figure 7.1.: Scheme of the preparation of the Pd/Fe_3O_4/Pt(111) model catalyst surface; in the first step an iron oxide film is grown on the bare Pt(111) surface; subsequently Pd is deposited on the oxide and form particles upon heating

Thin oxide films can be grown by surface oxidation of metal single crystals or by successive deposition and oxidation of metal on an appropriate substrate. The latter approach was used in the following. Figure 7.1 illustrates the preparation scheme of the Pd/Fe_3O_4/Pt(111) model catalyst. First, the iron oxide film was epitaxially grown on clean Pt(111) surface by iterative physical vapor deposition and oxidation. Afterward, Pd is deposited on the iron oxide film by physical vapor deposition. Therefore the oxide acts as a support for the Pd nanoparticles.

The preparation as well as the geometric and electronic properties of the pristine Fe_3O_4 film and the supported Pd particles will be discussed below.

7.1.1. The Fe_3O_4 film on Pt(111)

The growth of iron oxide films on Pt(111) was extensively studied in recent years [197–212]. Three different iron oxide films were found to form on Pt(111): (i) FeO, (ii) Fe_3O_4, and (iii) Fe_2O_3 can be obtained on the Pt(111) surface, depending on the growth conditions, amongst others film thickness, oxygen partial pressure, and temperature [210]. According to these studies, the first deposited monolayer of iron is fully covered by an oxygen overlayer after oxidation, forming a polar iron and oxygen bilayer similar to the rock salt-structure found in bulk FeO in the (111) direction [197, 199]. On this ultrathin FeO film the Fe_3O_4 grows in a *Stranski-Krastanov* like mode — i.e. Fe_3O_4 grows in flat three-dimensional islands [203, 206]. The Fe_3O_4 islands coalesce with increasing coverage, forming a closed Fe_3O_4 oxide with broad, flat terraces. The thin Fe_3O_4 film has the structure of bulk Fe_3O_4 (*magnetite*, with mixed iron oxidation states: Fe^{2+} and Fe^{3+}). The crystallographic bulk and surface structure of the Fe_3O_4 film was investigated by numerous methods, including photoelectron spectroscopy [201, 202, 204, 206], AES [201], STM [203, 206, 207], high resolution TEM [208], LEED [187, 201, 205], X-ray photoelectron diffraction [206], TDS [209, 211], high resolution electron energy loss spectroscopy (HREELS) [211] and IRAS [211]. Figure 7.2 shows a previously reported STM image of the Fe_3O_4 surface (figure 7.2a) [211], a LEED pattern (figure 7.2b) and a bulk structure model (figure 7.2c) [210]. The iron oxide film exhibits atomically flat terraces and the LEED pattern shows a (2×2) structure indicating long range order of the Fe_3O_4 film. Figure 7.2c shows a proposed structure model for bulk Fe_3O_4. The Fe_3O_4 thin film was shown to have the same crystal structure as bulk Fe_3O_4. The bulk phase of Fe_3O_4 magnetite is a ferrimagnet and has an inverse spinel structure where the oxygen anions form a close-packed fcc sublattice with Fe^{2+} and Fe^{3+} cations located at the interstitial sites. One cation site is tetrahedrally coordinated to the oxygen which is occupied only by Fe^{3+} ions. The other site is octahedrally coordinated to the oxygen,

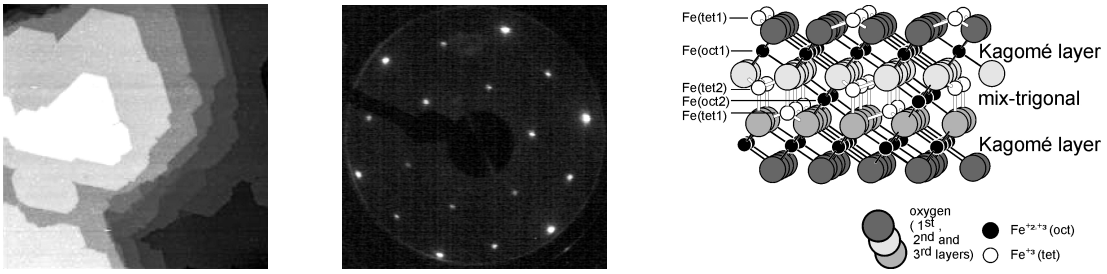

(a) **(b)** **(c)**

Figure 7.2.: (a) STM image, 300×300 nm [211]; (b) LEED-pattern (70 eV); (c) structure model of the Fe_3O_4 film [210]

being occupied by equal numbers of Fe^{2+} and Fe^{3+} ions [210]. At about 120 K, Fe_3O_4 shows a metal-insulator transition with a change in the electric conductivity by two orders of magnitude, the so-called Verwey transition [213]. This significant increase in conductance for temperatures higher than 120 K is attributed to electron hopping between Fe^{2+} and Fe^{3+} ions. These electrons are frozen out below the transition temperature. The surface termination of the Fe_3O_4 film has not been determined unambiguously until now. Based on experimental results, different surface termination were proposed. The results of STM and dynamic LEED investigations by Weiss *et al* were modeled best by a surface termination with tetrahedral coordinated Fe^{3+} (see figure 7.2c). Shaikhutdinov *et al.* proposed a termination with octahedral Fe^{3+} based on TDS and IRAS of adsorbed CO studies as well as high resolution EELS [211].

7.1.2. Iron Oxide supported Pd Nanoparticles

The epitaxially grown Fe_3O_4 film described above acts as a support for the deposition of the Pd metal, as displayed in figure 7.1. The growth behavior and morphology of metals deposited on (oxide) surfaces is controlled by the interaction energy $\gamma_{interface}$ between the oxide and the metal, and by the surface free energies of the metal γ_{metal} and the oxide γ_{oxide}; those properties govern whether the deposited metal will wet the oxide surface, be covered by the oxide and get integrated into it, or if it will agglomerate to three-dimensional particles. Pd on Fe_3O_4 is known to form nanoparticles [214, 215], indicating Volmer-Weber-growth ($\gamma_{oxide} < \gamma_{metal} + \gamma_{interface}$). Therefore, the growth of Pd nanoparticles on Fe_3O_4 is a spontaneous process and occurs as soon as the metal is deposited on the oxide, provided that the atomic mobility is high enough.

The morphology of the Pd particles on the Fe_3O_4 support was investigated previously by STM [214–216] and IRAS [215], utilizing CO as a surface probe. On Fe_3O_4, Pd forms hexagonally shaped particles, which are terminated by a large (111) terrace on top and (111) as well as (100) facets at the particle sides. The (111) top facets account for $\sim 40\%$, the side (111) facets for $\sim 30\%$ and the (100) side facets for $\sim 30\%$ of the total Pd surface [215]. In previous STM studies, the mean particle size of the Pd/Fe_3O_4 model catalyst was characterized as a function of Pd deposition thickness [214, 216]. Figure 7.3 shows a series of STM images of the Pd/Fe_3O_4 model catalyst surface for different deposition thicknesses of Pd. Due to a convo-

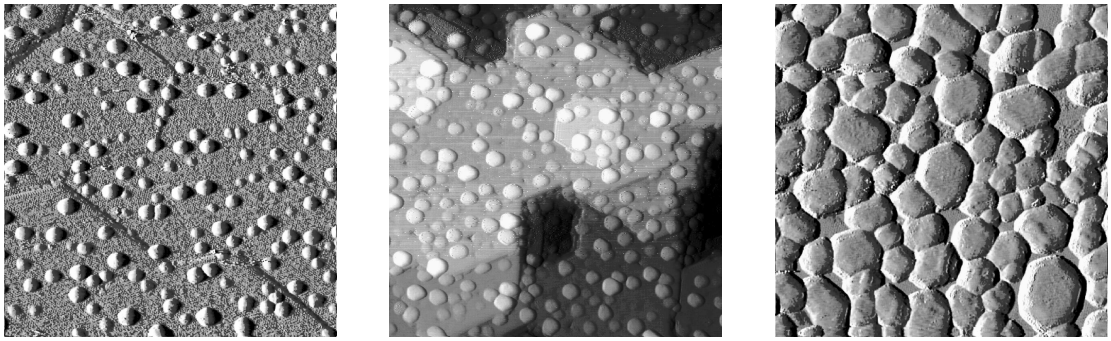

(a) Pd coverage: 0.3 Å **(b)** Pd coverage: 4 Å **(c)** Pd coverage: 7 Å

Figure 7.3.: Previously obtained STM images of Pd particles on a Fe_3O_4 film of $100 \times 100\,\mathrm{nm}$ size, figures (a)-(c) show preparations with different amounts of Pd covering the Fe_3O_4 surface [216]

Table 7.1.: Structural data of the Pd/Fe_3O_4 model catalyst as determine by STM [216]

Pd deposition thickness [Å]	0.3	4.0	7.0
nominal Pd coverage [$\mathrm{atoms \cdot cm^{-2}}$]	$2.1 \cdot 10^{14}$	$2.8 \cdot 10^{15}$	$4.9 \cdot 10^{15}$
island density [$\mathrm{cm^{-2}}$]	$1.7 \cdot 10^{12}$	$3.8 \cdot 10^{12}$	$1.0 \cdot 10^{12}$
average number of Pd atoms per island	~ 120	~ 740	~ 4900
number of Pd surface atoms per island	~ 65	~ 240	~ 870
average particle size [nm]	1.8	4	8

lution of the tip shape with the particle, the precise identification of the particle shape and size is difficult in the low particle size limit [196]. Therefore the average number of Pd atoms per particle was estimated from the total number of deposited Pd atoms and the average island density assuming a hemispherical particle shape. Figure 7.3a shows an STM image with the lowest investigated Pd deposition thickness of 0.3 Å. The nucleation of the Pd particles occurs in a well-distributed fashion over the Fe_3O_4 terraces. The average number of Pd atoms per particle is estimated to be about 120. Increasing the Pd deposition thickness to 4.0 Å, shown in figure 7.3b, results in an increased particle nucleation density and formation of crystalline aggregates with a rather flat top of near hexagonal shape. The hexagonal shape indicates that Pd particles grow in the (111) orientation and that their sides are terminated either with (111) or (100) facets. The average number of Pd atoms per particle is 740. Figure 7.3c shows an image for a Pd coverage of 7.0 Å. Pronouncedly larger aggregates ($\sim$ 4900 Pd atoms/island) are formed retaining a hexagonal form and a high degree of crystallinity. The properties of the Pd particles are summarized in table 7.1 according to the Pd deposition thickness.

The reduction of the lattice constant with decreasing Pd particle size was observed by X-ray absorption spectroscopy and transmission electron microscopy (TEM) [217–219]. The Pd particles in these studies were supported on thin oxide film or embedded in a matrix (either solid argon or a polymer). The lattice constants for the Pd particles were reported to contract by 3 to

5% for particle dimension of about 1.2 to 1.4 nm, with respect to the Pd bulk lattice constant of 389 pm with the nearest neighbor distance of 275 pm. Pd particles prepared on silicon under non-UHV conditions also exhibit the effect that the lattice constant of small particles was reduced with respect to the bulk [220]. The reduction of lattice constant with decreasing particle size was also observed experimentally for various other metals, such as: Pt [221], Ta [222], Cu [223, 224], Ni [223], Ag [224] and Au particles [225].

Theoretical calculations focusing on the average bond length in Pd clusters are consistent with the experimental observations and predict the bond lengths to increase with size, exhibiting linear scaling with the average coordination number [226–228]. Similar results were obtained by calculations focusing on Au particles by Huang *et al.* [229].

By UPS and XPS studies, it became evident that also the electronic structure of nanoparticles strongly depends on the particle size. For supported clusters, shifts toward higher binding energies are typical for decreasing particle size, for which also the lattice constant was found to decrease. The core-level binding energy of metals such as Au, Ag, Pd, Ni and Cu were found to increase significantly for decreasing particle size [230–235]. Shifts were also observed in the valence photoemisison spectra on Al_2O_3 supported Pd particles, where the binding energy of the Pd 4*d* electrons increases with decreasing particle size [236]. Further analysis of the XPS data related the initial state contribution of the change in binding energy to the lattice strain that is present for particles because of the observed lattice constant reduction for small particles as compared to the bulk [237]. The strain induced shift of the core level binding energies shifts is not exclusively related to particles but was also observed for bimetallic system, consisting of metallic thin films grown on metal single crystal surfaces [30, 238]. Here, strain was induced by the lattice constant mismatch of the two metals.

7.1.3. Preparation of Pd Model Catalysts

Preparation of the Fe_3O_4

The Pt(111) crystal surface is cleaned by repetitive argon ion sputtering at room temperature (typically: 1 keV at an ion current of 30 μA for 45 minutes) and subsequent annealing at 1200 K for 3 minutes. Carbon that may have segregated to the surface during the cleaning process was removed by heating in oxygen atmosphere (720 K at $p_{O_2} = 10^{-6}$ mbar O_2). The cleaning of the Pt surface was check by LEED, AES, TDS and optical reflectivity.

The preparation of iron oxide films on the clean Pt(111) surface was studied in detail by Weiss and coworkers [210] and is described briefly in the publication by Lemire *et al.* [211]. In accordance with this procedure, first a FeO monolayer film was grown on the clean Pt single crystal. Subsequently, Fe_3O_4 starts to grow on the FeO film in a *Stranski-Krastanov* like growth mode. The Fe_3O_4 film was prepared as follows:

1. **FeO film preparation:** At room temperature, 1 Å of Fe (where 1 Å corresponds to $7 \cdot 10^{14}$ atoms $\cdot$ cm^{-2}) was deposited on the clean Pt(111) surface at a deposition rate of ~ 1 Å/min. Prior to the metal deposition, the evaporator flux was calibrated by means of a quartz microbalance. The sample was biased to the evaporant's positive potential to prevent acceleration of metal ions. After the metal deposition, the oxygen pressure was adjusted to 10^{-6} mbar or 10^{-7} mbar for the ultrathin or the thick sample, respectively. The

temperature was raised to 1000 K for 2 minutes. Finally, the oxygen was pumped off at 500 K during the cool down.

2. If LEED showed a characteristic FeO pattern, the sample was flashed to 600 K.
3. **Fe_3O_4 film preparation:** Successively, 24 Å of Fe were deposited on the FeO monolayer film in increments of 4 Å per deposition cycle. A deposition cycle consisted of:
   a) Deposition of 4 Å of Fe at $\sim$ 130 K (deposition rate: $\sim$ 1 Å/min)
   b) Oxidation of the deposited Fe at 875 K for 3 minutes in oxygen atmosphere at a pressure of 10^{-6} mbar or 10^{-7} mbar for the ultrathin or the thick single crystal, respectively.
   c) Pump down of the oxygen atmosphere at a sample temperature of 500 K during the cool down.
4. Finally, the sample is flashed to 800 K and checked by LEED.

The resulting Fe_3O_4 film had a thickness of about 10 nm, which was determined by TEM in collaboration with the Inorganic Chemistry Department of the Fritz-Haber-Institute [239].

Pd Particle Preparation

Pd nanoparticles were grown on the Fe_3O_4 film by physical vapor deposition (PVD) and subsequent annealing. Before Pd deposition, the Fe_3O_4 thin film was annealed at 800 K in UHV to desorb potentially present adsorbates. Then the desired amount of Pd was deposited by PVD at 115 K (the sample was biased to the potential of the evaporant, 800 V; deposition rate $\sim$ 0.3 Å/min). The evaporator was calibrated prior to the metal deposition by means of the quartz microbalance. Finally, the sample is annealed at 600 K for 1 minute.

7.1.4. Determination of the Reflectivity for Pd/Fe_3O_4

The reflectivity of the sample surface is a crucial parameters in the accurate determination of the deposited energy by the microcalorimeter. All Pd/Fe_3O_4/Pt(111) systems were prepared on a thick Pt(111) sample and characterized by the in situ reflectivity measurement setup.

Influence of the Fe_3O_4 Film Thickness on the Reflectivity

The optical reflectivity of the Fe_3O_4 film on Pt(111) was investigated at a photon energy of $\sim$ 1.95 eV ($\lambda = 632.8$ nm) as a function of the deposited amount of iron that is subsequently oxidized and annealed. As the iron is deposited at $\sim$ 120 K the reflectivity measurements are also carried out at this temperature. Figure 7.4a shows the reflectivity as a function of iron deposition thickness. The reflectivity at 120 K initially amounts to $\sim$ 74% for the first deposition cycle, coinciding with the reflectivity of pristine Pt(111) at 120 K. Further deposition and oxidation of iron results in a linear decrease of the reflectivity with a gradient of (-0.19 ± 0.06) %/Å. In total, 24 Å of iron were deposited and oxidized, corresponding to a thickness of the Fe_3O_4 film of about 10 nm, as determined independently by TEM[239]. The prepared iron oxide film shows

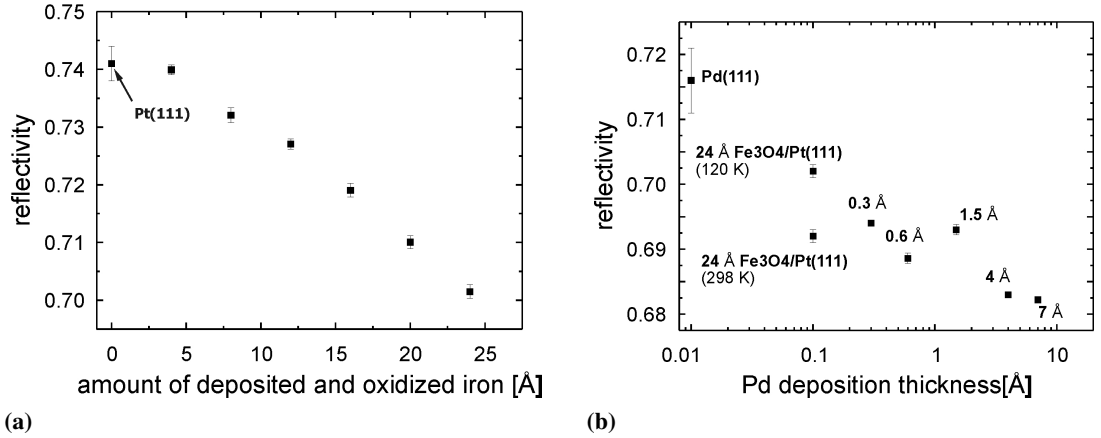

Figure 7.4.: Reflectivity of (a) the Fe_3O_4/Pt(111) as a function of the deposited and oxidized amount of iron determined at 120 K and (b) the supported Pd particles on the Fe_3O_4/Pt(111) as a function of the deposited amount of Pd determined at 298 K, Pd(111) is arbitrarily set to a Pd coverage of 0.01 Å.

a reflectivity of $\sim 70.2\%$ at 130 K. At room temperature the reflectivity was determined to be $\sim 69.2\%$. The difference of about 1% is likely to be related to the underlying Pt(111) as Fe_3O_4 was reported to be mainly transparent at the according photon energy [240]. Optical properties of magnetite Fe_3O_4 were investigated by Schlegel *et al.* using naturally grown single crystals. A reflectivity of $\sim 20\%$ at a photon energy of ~ 1.95 eV was reported, stating an accuracy of 1%. Also an absorbance of 17000 cm^{-1} was derived. Accordingly, the initial light intensity is attenuated by about 1.7% after passing through a 10 nm thick Fe_3O_4 film.

Determination of the Reflectivity for the Pd/Fe_3O_4/Pt(111) Model Catalysts

The reflectivity of various amounts of Pd deposited on the Fe_3O_4 film was studied at room temperature. Figure 7.4b shows the reflectivity as a function of Pd deposition thickness along with the reflectivity derived for the Pd(111) surface. Pd(111) is arbitrarily displayed at a Pd deposition thickness of 0.01 AA. Considerable efforts were required to clean the Pd(111) surface before the determined reflectivity converged to a reproducible value. The reflectivity was determined on two Pd(111) samples, being $(71.6 \pm 0.5)\%$. The error is significantly higher than on the Pt(111) and is related to local surface roughness present on the Pd(111) samples. The determined reflectivity is close to previously reported values for Pd crystals or evaporated Pd films of about 30 nm thickness , ranging between 70.6% and 72.9% [140, 241–244].

For Pd deposition on the Fe_3O_4 film, the measurements yielded a decreasing reflectivity for an increasing amount of Pd. This observation may be rationalized by an increasing fraction of multiple scattering events in the Fe_3O_4 film as it becomes covered by Pd. For the three lowest Pd deposition thicknesses, 0.3, 0.6 and 1.5 Å, the reflectivities coincide within less than 1% with the bare Fe_3O_4 film on the Pt(111) at room temperature of 69.2%. However, a trend to lower reflectivities is evident. The trend is more pronounced for the higher Pd deposition thicknesses

of 4 and 7 Å where the reflectivity is found to be 68.3% and 68.2%, respectively. It is important to bare in mind that the growth of the iron oxide layer may be affected by fluctuations in the metal flux from the evaporator of up to 20%. Taking into account the impact of the amount of deposited and oxidized iron on the reflectivity of ~ 0.2 %/Å, a fluctuation of 4 to 5 Å in the iron deposition thickness may result in reflectivity variations of $\sim 0.8\%$. To exclude this effect as an origin for the above mentioned variations in reflectivity at low Pd deposition thicknesses, more statistics, namely sample preparations, are needed. In the following, the derived reflectivity values are used in the according energy calibrations.

7.2. CO Adsorption on Fe_3O_4 supported Pd Particles at 298 K

The energetics of carbon monoxide adsorption on Fe_3O_4 supported Pd particles and Pd(111) were investigated. The average size of the supported particles was varied by the deposition thickness of Pd, in particular 0.3, 0.6, 1.5, 4 and 7 Å. The average particle size ranges from 1.8 nm to 8 nm as derived from STM images for 0.3, 4 and 7 Å [216].

7.2.1. Introduction

In this section, a brief overview is provided about previous studies on CO adsorption on supported Pd particles and Pd single crystals. A detailed review on surface studies on supported model catalysts can be found elsewhere [8].

The CO-Pd Bond

The bonds of a free CO molecule constitutes of bonding molecular orbitals (3σ, $1\pi_x$, and $1\pi_y$) with six electrons in total. Four further valence electrons are located in the 4σ and in the 5σ molecular orbital of the CO. The 5σ molecular orbital is the highest occupied molecular orbital (HOMO) in free CO.

A comprehensive model of CO adsorption on 4d metals was introduced by Blyholder [29]. Upon adsorption of CO on a Pd surface, charge can be transfered from the 5σ HOMO to a lower energy level of the Pd. This electron donation results in the formation of a σ bond between the carbon atom in the CO and the Pd surface. A fraction of the transfered charge is donated back into the $2\pi^*$ molecular orbital, being the lowest unoccupied molecular orbital (LUMO). This back donation yields a π bond [29, 245]. The $2\pi^*$ molecular orbital has a binding character for the CO-Pd bond and an antibonding character for the inner molecular C-O bond. The electron donation and the resulting back donation depends on the Pd surface's actual density of states, which is related to the morphology, as discussed in section 7.1.2.

Sticking Probability

The Pd particles comprise (111) and (100) facets. On Pd(111), the initial sticking probability was determined previously by the King-Wells method [13], reporting an initial sticking probability of (0.98 ± 0.05) at temperatures between 300 and 650 K. On Pd(100), the sticking probability of CO was studied as a function of coverage by the King-Wells method [85] and by TDS

[246]. The initial sticking probabilities at room temperature were found to be 0.82 by the King-Wells method and 0.6 by TDS. The coverage dependence showed a typical precursor-mediated behavior.

The sticking probability was determined on freshly prepared Fe_3O_4 supported Pd particles [247]. The formal initial sticking probabilities for Pd deposition thickness ranging from 0.1 to > 12 Å were found to be between 0.09 to 0.68. It should be kept in mind that only a small fraction of the surface ($\sim 20\%$) is covered by Pd particles and that the majority of the impinging molecules hit the oxide support. Taking this fact into account, the sticking probabilities exceed the values expected for the case where only molecules can be adsorbed that hit the Pd particles directly. This observation is an evidence for a capture zone effect [52], where in addition to the molecules directly impinging on the active particles, other molecules can be trapped on the Fe_3O_4 support and reach the particles via diffusion.

Diffusion

Mitsui *et al.* investigated the diffusion of single CO molecules on Pd(111) by STM [248]. A diffusion activation energy barrier of (118 ± 5) meV was determined, resulting in fast equilibration of adsorbed CO species on Pd particles at the energetically most favorable positions at room temperature.

Coverage-dependent Population of Adsorption Sites

The population of CO adsorption sites on Pd was investigated by STM [249], LEED [246, 250–254], IRAS [250, 251, 253, 255], and photoelectron diffraction [256]. Pd particles expose (111) as well as (100) facets and exhibit edge and corner sites. On Pd(100), CO was found to adsorb only on bridge sites, regardless of coverage [250, 251]. At 300 K, the saturation coverage of CO of 0.5 monolayer forms a $c(2\sqrt{2} \times \sqrt{2})R45^\circ$ overlayer structure [246]. On Pd(111), a variety of ordered adsorption overstructures were reported [252, 253]. These coverage dependent rearrangements are characteristic for adsorption on Pd(111) [257]. At low coverages, CO does not form a closed adsorbate structure, but agglomerates in islands of an inner $(\sqrt{3} \times \sqrt{3})R30^\circ$ structure; the island formation ends at a coverage of $1/3$ monolayer, where CO forms a closed $(\sqrt{3} \times \sqrt{3})R30^\circ$ overstructure in which CO is bound in fcc hollow sites [252]. On further increase of the CO-coverage, an ordered $c(4 \times 2)$-2 CO overstructure is formed with a CO coverage of 0.5 monolayer, being the maximum equilibrium coverage under UHV conditions studies at 300 K.

The particular adsorption sites are still under debate. First, the stretching frequency of CO on Pd(111) at room temperature was interpreted as an indication that CO is adsorbed in bridge sites [255]. Later results from diffraction and STM studies were interpreted as CO adsorption in a combination of fcc and hcp hollow sites [256]. Recently, Rose *et al.* suggested on the basis of STM studies that, additionally to CO bound to threefold hollow sites, structures with bridge-bonded CO and CO adsorbed in hollow sites can coexist [249].

Influence of Adsorption on the Electronic Structure

It is known that the electronic structure of extended metal surfaces changes upon CO adsorption [30, 258]. This effect was observed e.g. by Sandell et al. for the adsorption of CO on Al_2O_3/NiAl(110) supported Pd particles of different mean sizes [234]. At 90 K, it was shown by XPS that the binding energy of Pd 3*d* electrons increases by about 1 eV for large Pd particles due to CO adsorption and even more for smaller particles. The effect was less pronounced when the sample was heated to 300 K and may be related to the desorption of about 60% of the CO coverage [234].

Heats of Adsorption

As already mentioned, Pd particles expose (111) as well as (100) facets and exhibit edge and corner sites. On Pd(111), the adsorption energy was assessed by isothermal desorption [13], by TDS [22, 259–261] and adsorption isotherms [257, 262–265]. Initial value were reported in a range between 126 and 149 kJ/mol. For Pd(100), the initial adsorption energy was studied by the single crystal adsorption calorimetry [25, 85], by TDS [246] and by adsorption isotherms [262, 265]. The obtained values lie between 151 and 163 kJ/mol. Dramatic effects of low-coordination defect sites (like step edges) on CO adsorption energy, such as observed for Pt(111) [43], were not seen on Pd(111) [262, 266].

A number of studies already tried to determine the adsorption energy of CO on Pd particles as a function of particle size. However, no experimental setup was capable to measure the heat of adsorption directly, until now. Therefore, only indirect observations based on kinetic modeling of the desorption process exist. Previously, Pd particles were investigated on different supports. This review will concentrate on two efforts, investigating MgO supported Pd particles by molecular beam relaxation technique [21] and Pd particles supported on Al_2O_3/NiAl by TDS [22]. More details on other studies can be found elsewhere [8].

Duriez *et al.* studied the heat of adsorption for CO on MgO supported Pd particles as a function of average particle size (1.2 to 12 nm) [21, 267–269]. They applied a molecular beam relaxation method where the initial desorption energy is derived from the temperature dependency of the adsorbate's life time τ. This derivation is based on a kinetic model, where an assumption of the frequency factor ν and its coverage dependency needed to be made. The life time τ was determined from the exponential decay of the equilibrium coverage after switching off the beam. Temperatures were varied between 100° and 300° C. This method is accurate for simple adsorption-desorption processes. However, for particle sizes below 4 nm, the decay of the equilibrium coverage was never a true exponential showing a more complex adsorption-desorption kinetics [21]. Here, average life times $\bar{\tau}$ were determined from the changes in the surface coverage, which was estimated at nearly zero coverage. It was concluded that particles larger than 4 nm behave like extended Pd surfaces and that their initial adsorption energy is independent of size. For particles smaller than 4 nm the desorption energy was found to be increased by 33 kJ/mol with respect to larger particles.

Stara and Matolin studied the CO adsorption on Al_2O_3/NiAl supported Pd particles in a size range from 2.5 to 27 nm and Pd(111) by TDS [22]. Major differences were found in the desorption spectra. For small particles a double peak structure was observed where as the single crystal

spectra exhibited only a single peak. Desorption energies were derived by Redhead analysis and at low coverage also the method of Chan *et al.* [270] for all peaks. Again, an assumption about the frequency factor ν had to be made. The desorption energy for Pd(111) and large Pd particles nearly coincide, being, 135 to 137 kJ/mol and 137 to 138 kJ/mol, respectively. For small particles (2.5 nm) the desorption energy, which was derived from the higher temperature desorption peak, was found to be between 126 and 128 kJ/mol. At the same time, a reduction of adsorption capacity was observed for 2.5 nm particles with an increasing number of adsorption-desorption cycles. Based on simultaneously observed CO_2 desorption, the authors rationalized this effect by the partial dissociation of CO leaving carbon on the surface. The change in the CO adsorption capacity may also be caused by temperature induced restructuring of the particles. This problem could be present likewise for the molecular beam study of Duriez *et al.*.

Theoretical Studies

Sautet *et al.* found by total energy calculations that the most stable adsorption sites of CO on Pd(111) is a combination of hcp-fcc threefold hollow sites [271]. For Pd particles, the dependence of the lattice constant on the particle size, which was observed experimentally [217–219], is reproduced by relaxed Pd particle structures in theory [226, 228]. The clusters exhibit shorter interatomic distances with respect to bulk Pd. Particularly, it was shown by density functional theory that the average calculated Pd-Pd nearest-neighbor distance decreases with decreasing linear dimension of a nanoparticle in the range of 55 to 260 atoms per cluster [227]. The impact of the reduced lattice constant in the small Pd clusters on the CO adsorption energy was theoretically studied and it was demonstrated that Pd clusters consisting of 55 to 260 atoms, with optimized structures, show systematically lower adsorption energies by about 10 to 15 kJ/mol than the clusters with a bulk termination and interatomic distances of $d(Pd-Pd) = 275\,pm$ [272]. This was rationalized by the principle of bond order conservation: for contracted bond length in the Pd clusters, one expects weaker adsorption bonds as a result of better saturated valences of the substrate atoms [272].

7.2.2. Determination of Adsorption Energies by Microcalorimetry

Experimental

The Pd particle surfaces were prepared right before the adsorption measurements. After the final annealing step to 600 K for one minute the sample was transfered to the calorimeter

The applied beam intensity was $\sim 9.7 \cdot 10^{13}$ CO molecules $\cdot\, cm^{-2}s^{-1}$. The number of impinging molecules per pulse is calculated by the pulse length of 266 ms and the beam profile area of $0.126\,cm^2$ yielding:

$$\sim 2.6 \cdot 10^{13}\,cm^{-2} \times 0.126\,cm^2 = \sim 3.2 \cdot 10^{12}$$

being the absolute amount of CO molecules impinging on the sample surface per pulse.

Results and Discussion

Determining the Number of Adsorption Sites on Fe_3O_4

The CO adsorption properties of the Fe_3O_4 support was investigated in order to account for possible contribution in the later adsorption experiments with the Pd particles. The CO adsorption experiments on Fe_3O_4 were performed at room temperature and at 120 K. At room temperature no adsorption was observed. It is concluded that the residence time of CO on the Fe_3O_4 surface at room temperature is too short to be detected.

At a temperature of 120 K, CO adsorption was detected successfully. However, the calorimeter signal exhibits only one, sometimes two adsorption signals before the onset of the adsorption-desorption equilibrium was reached. This clearly indicates a very limited number of adsorption sites. The adsorption capacity could be recovered almost completely by flashing the sample to 600 K. Quantitative analysis of the sticking probability measurement yielded the number of adsorbates varying between $1.5 \cdot 10^{13}$ and $4.5 \cdot 10^{13}\,\mathrm{cm}^{-2}$. The adsorption energy was determined to be $(73 \pm 7)\,\mathrm{kJ/mol}$, where the error refers to the standard deviation of seven measurements.

The number of adsorption site is too small with respect to the number of surface atoms to be assigned to regular surface sites. Because of the density of adsorption site of about 1% compared to the number of surface atoms, defect site are most likely associated with the CO adsorption sites. This interpretation would also explain the variation of the adsorption capacity as the defect density may vary significantly.

Previously, a TDS study by Lemire *et al.* reported CO adsorption on Fe_3O_4 [211]. The spectra show two desorption features at 150 and 230 K at small exposure, less than 0.05 L, and three desorption features at 110, 180 and 230 K at larger exposures. The surface coverages were not reported. Combining these results from TDS with further investigation by high resolution EELS and IRAS, the desorption features were proposed to originate from CO species adsorbed on the Fe^{3+} cations (230 K peak), regular sites on the terraces, which are believed to be terminated by Fe^{2+} cations (180 K peak) and a weakly bound more mobile CO (110 K peak). The small number of adsorption sites obtained in this study is in contradiction to the interpretation of the 230 and 180 K peak, being regular adsorption sites. Most likely, the features relate to defect sites. The adsorption energy of $(73 \pm 7)\,\mathrm{kJ/mol}$ is close to the adsorption energy of about $60\,\mathrm{kJ/mol}$ derived by Redhead analysis of the desorption peak temperature of 230 K, assuming a frequency factor of $\nu = 10^{13}\,\mathrm{s}^{-1}$.

Sticking Probability for CO on Pd/Fe_3O_4 and Pd(111)

The sticking probabilities as a function of CO coverage was determined for Pd(111) and iron oxide supported Pd particles at 298 K.

Figure 7.5 shows the derived sticking probabilities as a function of coverage for Pd(111) and Pd deposition thicknesses ranging from 0.3 to 7 Å. The presented curves are averages of four to six independent measurements on freshly prepared Pd particle surface.

The coverage dependency of the sticking probability for Pd(111) shown in figure 7.5f is exemplary for CO adsorption on Pd. The sticking probability is initially (0.72 ± 0.03) and stays almost constant, up to a coverage of about $1.7 \cdot 10^{14}$ CO molecules cm^{-2}. For higher CO coverages, the sticking probability decreases and converges finally in a constant value, indicating an

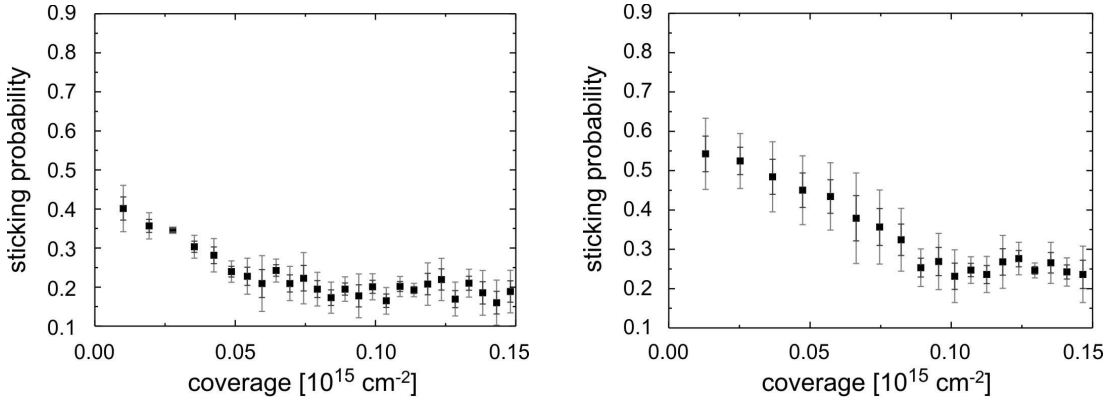

(a) Pd deposition thickness: 0.3 Å

(b) Pd deposition thickness: 0.6 Å

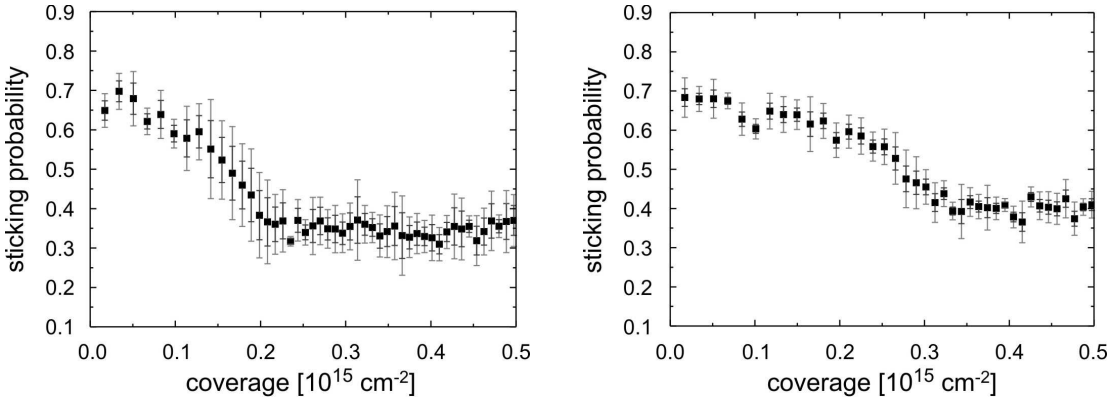

(c) Pd deposition thickness: 1.5 Å

(d) Pd deposition thickness: 4 Å

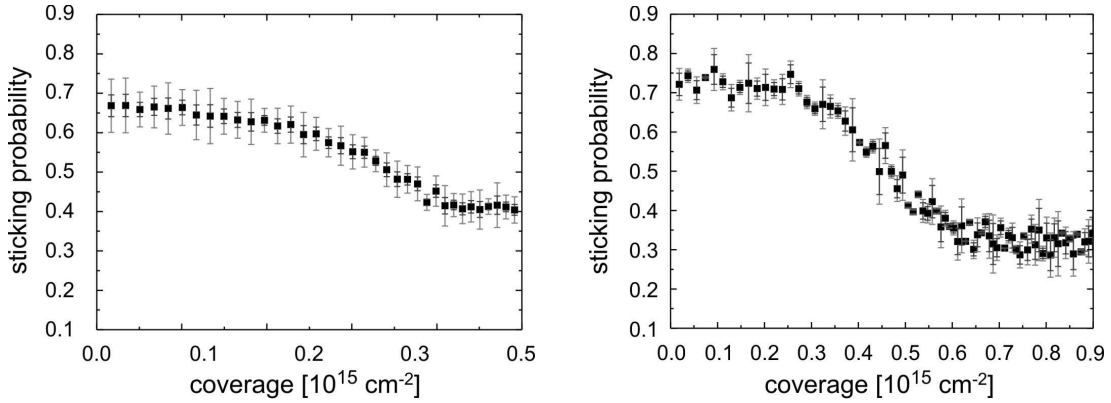

(e) Pd deposition thickness: 7 Å

(f) Pd(111)

Figure 7.5.: Sticking probabilities as a function of CO coverage at 298 K; the shown data are averages of for four to six independent measurements on freshly prepared Pd particle surfaces and Pd(111); the error bars show the according standard deviations (light gray) and errors of the mean (dark gray)

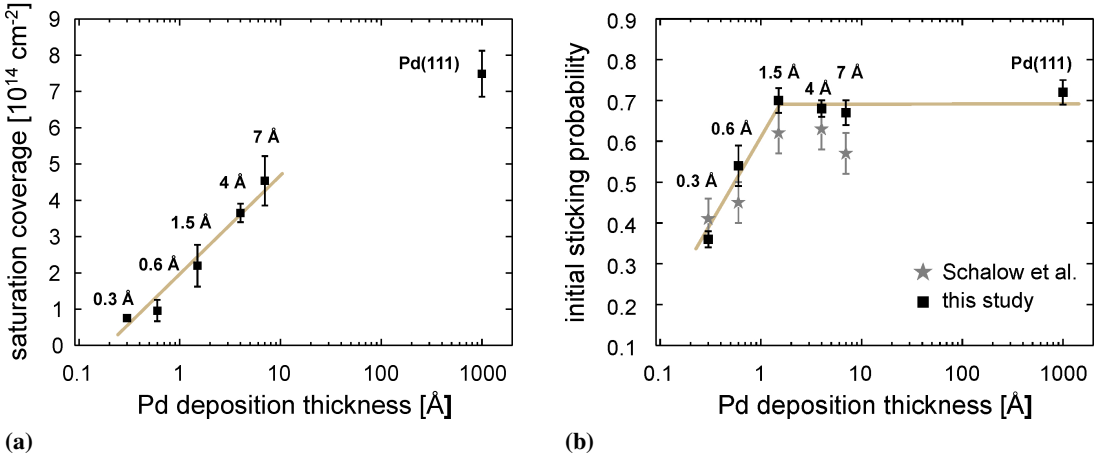

Figure 7.6.: (a) The number of adsorbed CO molecules in saturation as a function of Pd deposition thickness; the number of adsorbed CO molecules in saturation decreases with decreasing deposition thickness. (b) The initial sticking probability of CO is shown as a function of Pd coverage. Pd(111) is arbitrarily set to a deposition thickness of 1000 Å. The data of this study (squares) coincide with results previously obtained by a continuous molecular beam (stars) [247] within the error margins. The displayed errors are standard deviations. The displayed lines are added to guide the eye.

adsorption-desorption equilibrium, as already described for CO adsorption on Pt(111) in section 6.1, at a coverage of about $5 \cdot 10^{14}$ CO molecules cm^{-2}. The almost constant sticking probability at low coverage indicates a chemisorption process mediated by a mobile precursor.

The sticking probabilities for Pd particles with deposition thickness of 1.5 to 7 Å, shown in figures 7.5c to 7.5e, have qualitatively similar coverage dependencies. For smaller Pd deposition thicknesses, the sticking probabilities, shown in figure 7.5a and 7.5b, exhibit a nearly linear decline without an initial coverage range with sticking probabilities remaining more constant, which is characteristic e.g. for Pd(111). Figure 7.6a shows the determined number of adsorbed CO molecules on a model surface after saturation as a function of Pd deposition thickness. The number of adsorbed CO molecules in saturation increases continuously with increasing Pd deposition thickness.

Figure 7.6b shows two data sets of initial sticking probability as a function of the Pd deposition thickness. Pd(111) is arbitrarily set to a deposition thickness of 1000 Å. The black squares, derived from the data acquired along with the adsorption energy, coincide well within the statistical variations with earlier obtained initial sticking probabilities on freshly prepared Pd particles by a setup using a continuous molecular beam (gray stars) [247]. The initial sticking probability for the Pd(111) surface was derived to be $(73.5 \pm 0.6)\%$. The initial sticking probabilities for Pd(111) and Pd deposition thickness of 1.5 to 7 Å coincide within the error margins. This means that the probability of a CO molecule to find a Pd adsorption site is constant in this deposition thickness range despite the fact that for the Fe_3O_4 supported Pd particles a substantial fraction of the surface of 50 to 90% (based on the information in table 7.1) was not covered by Pd atoms.

Therefore, the close initial sticking probabilities evidence that the uncovered Fe_3O_4 serves as a capture zone for the Pd particles. Only for Pd deposition thicknesses of 0.3 and 0.6 Å the particle density on the surface is so low that a significant fraction of the CO impinging on the surface was not able to diffuse to the Pd particle before desorption.

The sticking probability indicates a mobile precursor-mediated adsorption as expected for oxide supported metal clusters [257]. For the Pd(111) surface, the initial sticking probability was found to be somewhat lower than the earlier reported values of $80-100\%$ [262] and $(95\pm5)\%$ [13]. It is difficult to identify the origin of the deviations in the reported initial sticking probabilities on Pd(111) and the here presented data. A reliable reference for the sticking coefficient would be needed to compare different experiments. However, for Pd(111) the onset of the adsorption-desorption equilibrium in the detected energy signal, being $(0.75\pm0.06)\cdot10^{15}\,\mathrm{cm}^{-2}$, 0.5 ML (ML refers to the number of Pd surface atoms), is in very good with previously published saturation coverages [262]. Also, the larger particles show the saturation coverages close to 0.5 ML. Only the smallest particles, with an average diameter of 1.8 nm (0.3 Å), show a higher saturation coverage of about 0.8 ML. This observation can be rationalized by the significant reduction in the surface structure as compared to the extended facets of particles or Pd(111). On the reduced surface, other adsorption sites than the threefold hollow, e.g. on-top sites or low coordinated surface sites, may become more important, accommodating an increased number of CO molecules per Pd surface atom.

Heat of Adsorption for CO on Pd/Fe_3O_4 and Pd(111)

The differential heat of adsorption of carbon monoxide was systematically studied as a function of Pd deposition thickness supported on a Fe_3O_4 film and Pd(111). The adsorption heat was calculated from the calorimetrically measured energy deposition upon adsorption and the according number of contributing adsorbates, where the latter was derived from the actual sticking probability and the number of impinging molecules.

CO diffusion on Pd is fast on the time scale of the experiment with an activation energy barrier for diffusion of $(118\pm5)\,\mathrm{meV}$, resulting in fast equilibration of adsorbed species at the energetically most favorable positions [248]. Additionally, it is important to note that CO does not dissociate on the Pd clusters in the investigated temperature regime [273].

Figure 7.7 shows the heats of adsorption for CO measured as a function of coverage on Pd(111) and Pd deposition thicknesses ranging from 0.3 to 7 Å. The presented data are averages of four to six independent measurements on freshly prepared Pd particle surface. On the smallest Pd particles ($\sim$ 120 Pd atoms/particle, figure 7.7a), the heat of CO adsorption initially amounts to $(106\pm2)\,\mathrm{kJ/mol}$. After adsorption of about $0.07\cdot10^{15}\,\mathrm{CO\ molecules/cm^2}$ corresponding to a CO surface coverage of 0.6 ML with respect to the number of surface Pd atoms. In the adsorption-desorption equilibrium the adsorption heat levels out at $(75\pm9)\,\mathrm{kJ/mol}$. Two reasons account for the decreasing adsorption energy with growing CO coverage: intermolecular repulsion of neighboring CO molecules and increasing competition for the d-electrons of Pd nanoclusters participating in the CO-Pd bonding. A qualitatively similar dependence of the adsorption heat on the CO coverage was observed for all larger Pd particles and for the single crystal surface. Figure 7.7f and 7.7e show heat of adsorption on Pd(111) and the largest Pd particles ($\sim$ 4900 Pd atoms/particle, mean diameter: $\sim$ 8 nm), respectively. On both surfaces, the

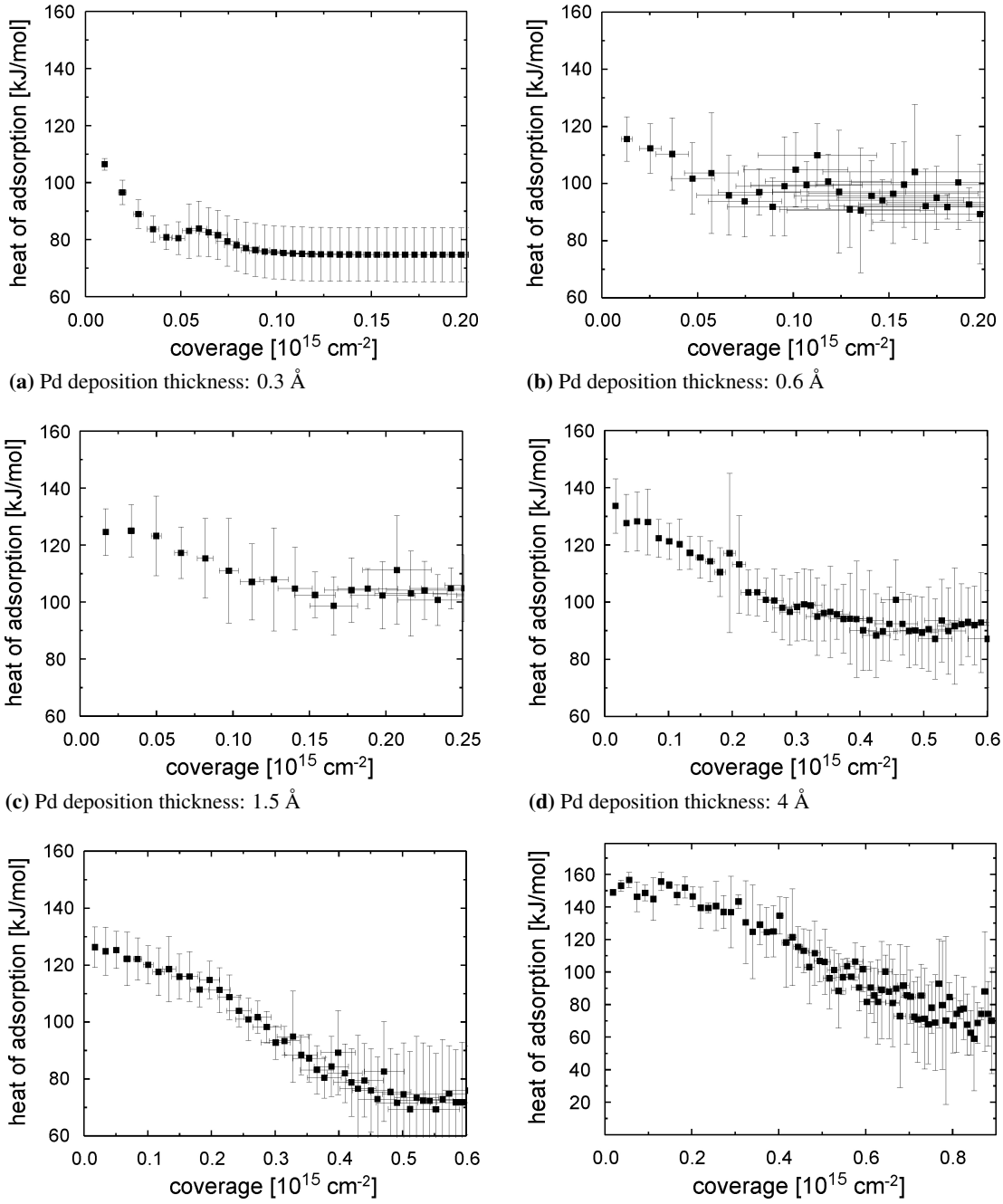

(a) Pd deposition thickness: 0.3 Å

(b) Pd deposition thickness: 0.6 Å

(c) Pd deposition thickness: 1.5 Å

(d) Pd deposition thickness: 4 Å

(e) Pd deposition thickness: 7 Å

(f) Pd(111)

Figure 7.7.: Differential heats of adsorption displayed as a function of coverage for five different Pd deposition thicknesses on Fe_3O_4 and Pd(111)

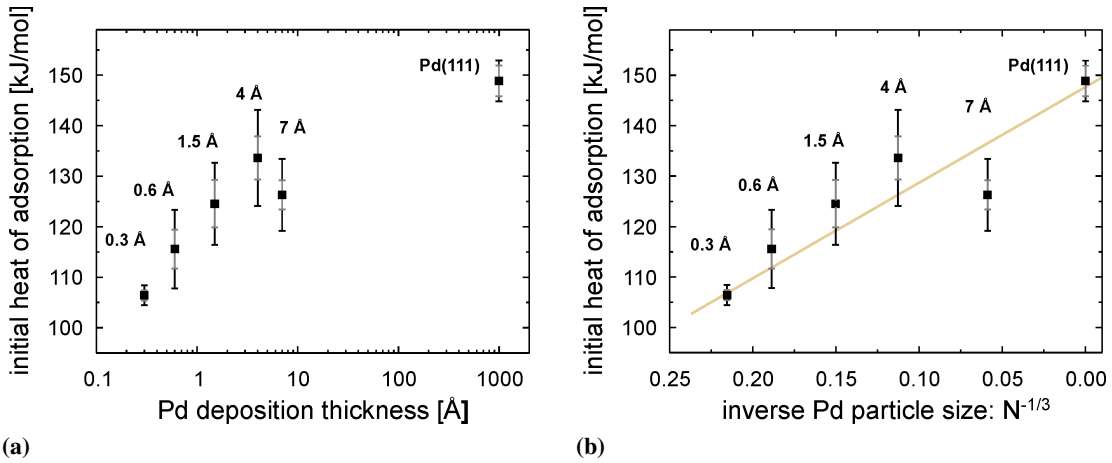

Figure 7.8.: (a) the initial heats of adsorption are shown as a function of Pd deposition thickness; a reduction of about $40\,\mathrm{kJ/mol}$ is present going from CO adsorption on Pd(111) to a Pd deposition thickness of 0.3 Å. (b) the initial heats of adsorption are shown as a function of $N^{-1/3}$, where N is the average number of atoms in a Pd particle. $N^{1/3}$ is proportional to the effective radius of a quasi-spherical particle [272].

initially high adsorption heat continuously decreases with growing CO coverage and reaches a lower steady state value in the quasi-equilibrium regime.

Initial Heats of Adsorption

Information on the particle size related change in the gas-surface interaction can be derived best from the least perturbed adsorption system, namely the first adsorption pulse, where the CO coverage is very low (0.01 to 0.08 CO molecules per surface Pd atom as estimated from the number of adsorbed molecules and the number of surface Pd atoms). Effects originating from intermolecular repulsion of neighboring CO molecules and increasing competition for the d-electrons of Pd nanoclusters are negligible. Therefore it can be assumed that the initial heats of adsorption were obtained in the low-coverage limit and governed predominantly by the interaction of a CO molecule with a Pd cluster.

Figure 7.8a shows the initial heats of adsorption as a function of Pd coverage. Pd(111) is arbitrarily set to 1000 Å to fit in the plot. The dependence of initial CO adsorption heats on the particle size shows a pronounced trend: the initial heat of adsorption decreases with the nominal Pd deposition thickness, i.e. with decreasing particle size, from $(126 \pm 7)\,\mathrm{kJ/mol}$ on 8 nm particles to $(106 \pm 2)\,\mathrm{kJ/mol}$ on the smallest 1.8 nm particles. Additionally, all investigated particles showed smaller initial adsorption energy as compared to the Pd(111) single crystal surface of $(149 \pm 4)\,\mathrm{kJ/mol}$. The initial heats of adsorption are summarized in table 7.2. Additionally, the estimated initial CO coverage after the first molecular beam pulse is presented.

Figure 7.8b shows the same data as a function of $N^{-1/3}$, where N is the average number of atoms/particle. $N^{-1/3}$ is proportional to the inverse volume of the particle. N was estimated

Table 7.2.: Initial heats of adsorption as a function of Pd deposition thickness, additionally the estimated amount of initially adsorbed CO is presented; monolayer ML refers to the number of Pd surface atoms.

Pd deposition thickness [Å]	initial heat of adsorption [kJ/mol]	initial CO coverage [ML]
0.3	106 ± 2	0.08
0.6	115 ± 8	
1.5	124 ± 8	
4.0	133 ± 4	0.02
7.0	126 ± 3	0.02
Pd(111)	149 ± 4	0.01

by use of the STM characterization of the Pd particles, summarized in table 7.1, assuming a hemispherical shape. The average particle sizes for deposition thicknesses of 0.6 and 1.5 Å were interpolated. Overall, the initial heat of adsorption is proportional to the inverse volume of the Pd particles.

Higher initial CO adsorption heats were measured on the large Pd nanoparticles (+20 kJ/mol) and the Pd(111) surface (+40 kJ/mol), with respect to the initial adsorption energy measured on the smallest particles. For the Pd(111) single crystal surface, both the initial heat of adsorption (149 ± 4) kJ/mol) was found to be in a very good quantitative agreement with the data reported in the literature [13, 262, 266]. Conrad *et al.* and Engel *et al.* reported the heat of adsorption of CO on Pt(111) to be 142 kJ/mol and 134 kJ/mol, respectively.

7.2.3. TDS Study to estimate possible Particle Contaminations from Residual Gas

A variety of contaminating species can be potentially adsorbed from the background and affect the measured initial heats of adsorption. Possible contaminants were repeatedly probed by TDS for all used Pd deposition thicknesses. After a waiting time of 30 minutes after finishing the sample preparation neither water nor CO_2 and only small amounts of CO ($\sim 1\%$ of the saturation coverage) were found.

7.2.4. Discussion

The initial heat of adsorption of CO on Pd particles shows a significant dependency regarding the particle size. The observation of a downward shift of about 40 kJ/mol for 1.8 nm particles as compared to Pd(111) resolves the longstanding controversy in the literature. The possible physical origins of this observation will be discussed in the following.

The Pd particles investigated in this work expose mainly (111) terraces alongside with a smaller fraction of (100) facets and low-coordinated defect sites such as edges and corners [216]. According to theoretical calculations, such irregular sites exhibit higher CO adsorption energies than Pd(111) [274]. Experimentally, there is a general agreement that the CO adsorption energy on the (100) plane is by about 10 to 15 kJ/mol higher than on the (111) plane [262]. However, the dramatic effect of low-coordination defect sites (like step edges) on CO adsorption energy,

such as observed for Pt(111) [43], was not seen on Pd(111) [262, 266]. This suggests that the degree of coordination of the surface atoms on stepped surfaces is not as important in determining CO adsorption energies on Pd as on other metals like Pt. Therefore, the increasing fraction of low-coordination Pd atoms with decreasing particle size, which normally would be expected to lead to higher adsorption energies for CO, might not be the dominant effect in determining how CO adsorption energies vary with particle size for Pd. Instead, other size-dependent properties of Pd nanoclusters must be responsible for the observed decrease of the initial heat of adsorption of carbon monoxide with decreasing particle size.

Two microscopic effects may contribute to the observed decrease of the initial CO adsorption heat with decreasing particle size: (i) weakening of the chemisorption interaction and (ii) reduction of the van-der-Waals attraction.

- Firstly, the decrease of the adsorption energy can result from a change in the electronic structure which is related to the contraction of the lattice constant of small metal nanoparticles (see section 7.1.2). Previously, it was demonstrated experimentally [217–219] that the interatomic bond length in small metal particles decreases with decreasing particle size. It is now well established, also by computational studies of various metals including Pd [226, 228], that relaxed structures of metal clusters exhibit shorter interatomic distances than bulk crystals. This phenomenon was rationalized as a result of decreasing average coordination number of the atoms with the higher surface-to-volume ratio of the cluster. Particularly for Pd, it was shown that the average calculated Pd-Pd nearest-neighbor distance decreases with decreasing linear dimension of a nanoparticle in the range of 55 to 260 atoms per cluster [227]. This lattice contraction in the small metal clusters was theoretically shown to result in a reduction of the adsorbate binding energy. Particularly for CO adsorption on the Pd clusters consisting of 55 to 260 atoms (in the size regime corresponding to, or lower than the smallest here investigated nanoparticles), it was demonstrated that the clusters with optimized structures show systematically lower adsorption energies by about 10 to 15 kJ/mol than the clusters with a bulk terminated geometry, i.e. with all interatomic distances $\mathrm{d(Pd-Pd)} = 275\,\mathrm{pm}$ [272]. This correlation of lattice constant contraction and the decreasing adsorption energy agrees with the principle of bond order conservation [275]: in the contracted clusters, one expects weaker adsorption bonds and stronger binding within the adsorbate as a result of better saturated valences of the substrate atoms. The decrease of the adsorbate binding energy with the lattice constant may be rationalized in terms of the strain effect, which is associated with a downward shift of the valence d-band with decreasing lattice constant [234, 258, 272]. Such effects were found not to be restricted to three-fold hollow sites on (111) facets, but reflect a general trend that also holds for adsorption at other sites of the particles, such as bridge sites and edges [272].

- A second reason for the decrease of adsorption heat of a gas-phase molecule on the small metal clusters is a feasible weakening of the dispersion force (van-der-Waals interaction) that is induced by dynamic response of bulk electrons of the metal to charge density fluctuations in an adsorbed molecule. Previously, it was shown that the electron population at the Fermi edge, which is mainly relevant for this interaction, drastically changes with the cluster size in the range of a few nanometers [236].

The two contributions can not be unambiguously disentangled by measurements of adsorption energies. The contribution of chemisorption is obvious by the observed change of the particle's and adsorbate's electronic structures [234]. Further, evidence for the particle size dependency of the Van der Waals interaction strength was previously found by a TDS study of methane on Pd particles of different sizes [276]. Desorption temperature peaks for methane were observed between 52 and 74 K on Pd particles ranging from 3.2 to 7.3 nm and Pd(111). The derived desorption energies lie between 15 and 22 kJ/mol, respectively. The reduction of the desorption temperature was attributed to the reduction of polarizability of smaller Pd particles as compared to larger Pd particles. Similar behavior was also observed for NO and N_2O desorption from Ag particles (radii $1-6$ nm) [277].

The large magnitude of the effect obtained in our study (about 40 kJ/mol relative to the Pd(111) surface) allows us to suggest that most likely reduction of both van-der-Waals interaction and chemisorption strength contributes to the overall decrease of the adsorption heat.

A more conclusive answer about the relative contributions could only be made on the basis of theoretical modeling. The present data may be especially important as benchmarks for the verification of upcoming theoretical ab initio methods for the calculation of adsorption energies, incorporating dispersive van der Waals interaction.

7.3. Conclusion

The differential heat of adsorption for CO on Fe_3O_4 supported Pd particles was investigated as a function of particle size by a combination of adsorption microcalorimetry and pulsed molecular beam techniques. Prior to the adsorption experiments the Fe_3O_4 support was characterized with respect to its optical properties and its CO adsorption capabilities. The reflectivity at a wavelength of $\lambda = 632.8$ nm was found to decrease linearly with increasing iron deposition thickness. A gradient of (0.19 ± 0.06) %/Å, where Å refers to the deposited thickness of iron, was derived. The optical reflectivity of the final oxide film, which is based on the subsequent oxidation of 24 Å of iron, was determined to be 69.2% at 298 K. CO adsorption on Fe_3O_4 was observed only at 120 K and not at 298 K. It was possible to quantify the number of adsorption sites, being $1.5 \cdot 10^{13}$ to $4.5 \cdot 10^{13}\,\mathrm{cm}^{-2}$. The limited number of adsorption sites at 120 K implies that the Co adsorbs most likely on defect sites.

Afterward, the heat of adsorption was investigated as a function of particle size for several average Pd particle sizes ranging from 1.8 to 8 nm and for Pd(111). The average particle size was varied by the deposited amount of Pd on the oxide film. For five different Pd coverages at least four independent adsorption measurements were performed on freshly prepared particles. The initial heat of adsorption as a function of mean particle size was derived and the initial heat of adsorption clearly shows a reduction with decreasing particle size. The decrease was found to amount to about 43 kJ/mol for average particle sizes of 1.8 nm with respect to the initial heat of adsorption of (149 ± 4) kJ/mol for Pd(111). Potential contributions are identified to be (i) changes in the chemisorption interaction due to changes of the lattice constant of small particles and (ii) the reduced polarizability of smaller particles due to the reduced number of free electrons. Therefore, the present data may be especially important as benchmarks for the verification of upcoming theoretical ab initio methods and tools, incorporating the dispersive

Van der Waals interactions.

8. Summary

A detailed microscopic understanding of elementary surface processes constitutes the final goal in heterogeneous catalysis research, which will enable control over the design of reaction kinetics by tuning the properties of the catalyst. In this perspective, adsorption heats represent an important information on the energetics of the adsorption and reaction processes, providing also significant benchmarks for theoretical methods.

This work was intended to contribute an accurate quantitative correlation of surface structure and adsorption energy, in particular, the heat of adsorption was determined for carbon monoxide on Pd particles as a function of particle size. For this purpose a new UHV single crystal adsorption calorimeter was set up, which allows the measurement of the heat of adsorption of atoms or gaseous molecules as a function of coverage on well-defined model catalysts.

Construction and Calibration of a new UHV Microcalorimeter

To correlate the structure of the catalyst and its interaction energy with adsorbates from the gas-phase, a new UHV single crystal adsorption calorimeter experiment was set up and calibrated. It combines single crystal adsorption calorimeter with molecular beam techniques and provides an experimental possibility to prepare model catalyst surfaces.

A dedicated preparation chamber was instrumented with all necessary means to prepare and characterize model catalyst surfaces and single crystal surfaces, including LEED, AES, thermal desorption spectroscopy, and an in situ reflectivity measurement setup. A separate calorimetry chamber was equipped with a single crystal adsorption calorimeter, a pulsed effusive molecular beam and according calibration devices to determine the absolute amount of energy deposited upon interaction of the gas-phase molecules with a model surface, and the absolute number of adsorbed molecules in absolute terms. The latter can be derived from the well-defined flux of the pulsed effusive molecular beam, and the determination of the actual sticking probability. The calorimeter is based on a pyroelectric $\beta-$PVDF ribbon, which is brought in contact with the single crystal sample. For energy calibration of the calorimeter, the gas adsorption signals are compared to laser light absorption signals. The calibration measurements involve three detectors, i.e. the calorimeter, a photodiode, and a beam monitor. The setup is based on the design of Campbell *et al.* and incorporates improvements regarding possible systematic errors in the calibration (in situ determination of the reflectivity, in situ photodiode, alignment of the three detectors by a rotatable table), the temperature stability and the susceptibility to vibrations. The calorimeter can be operated at arbitrary temperatures between 100 and 300 K.

The calorimetric measurement of the heat of adsorption comprises a series of successive measurements. The deposited energy as well as the number of adsorbed molecules have to be determined accurately. The energy calibration involves the calibration of the laser power, the pulse length and the reflectivity. Therefore, the in situ reflectivity measurement is of particular impor-

tance due to the fact that reflectivities of supported model catalysts are unknown and that also single crystals may exhibit a significant temperature dependency. The latter effect was found for the reflectivity of Pt(111) being (73.03 ± 0.08) % and (74.1 ± 0.1) % at 298 and 120 K, respectively.

The calorimetric energy measurement has a systematic error of typically 3.2 %, which is set by the pulse-to-pulse standard deviation of 15 nJ, for deposited energies around 500 nJ. The according accuracy is about 1%. The pulse-to-pulse standard deviation of 15 nJ corresponds to a detectable equivalent of about $4 \cdot 10^{-4}$ monolayer of CO on Pt(111) (monolayer: $1.5 \cdot 10^{15}\,\mathrm{cm}^{-2}$) with a heat of adsorption of 130 kJ/mol. The amount of adsorbed molecules per pulse is derived from the molecular flux, the beam profile, the pulse length and the actual sticking probability. For the determination of the amount of adsorbed molecules per pulse, successive calibration measurements yield a precision of 5.4 to 30.4%, depending mainly on the determination of the beam profile area at high sticking probabilities ($S \approx 0.7$) and variations of the sticking probability at low sticking probabilities ($S \approx 0.3$). The according accuracy is 4%. In conclusion, the heat of adsorption can be determined by the new calorimeter setup with an overall precision of 6.3 to 32.0% and an accuracy of about 5%.

Verification of reliable Operation: CO and Benzene Adsorption on Pt(111)

The heat of adsorption of CO and benzene was determined on Pt(111) in order to test the proper functioning of the microcalorimeter experiment.

CO adsorption was investigated on Pt(111)at 298 K and, for the first time, at 120 K. Energy and sticking probability data were obtained in series of six (298 K) and nine (120 K) independent measurements. The initial sticking probabilities coincide at (0.710 ± 0.005) and (0.722 ± 0.003). However, as the coverage increases the determined sticking probabilities of the 120 K experiment are systematically higher by up to 13%. The sticking probabilities level off in an adsorption-desorption equilibrium near the saturation coverage. This can be rationalized by desorption of CO between pulses which is caused by a pressure dependent saturation coverage. The initial sticking probabilities and the derived saturation coverages are compatible with previously reported studies. The derived initial heats of adsorption coincide within the experimental errors at (130 ± 3) and (124 ± 3) kJ/mol for 298 and 120 K, respectively. The coverage dependencies show qualitatively similar behavior. The heat of adsorption decreases with increasing coverage and levels off to a constant value near the saturation coverage. A minor difference is present at coverages between 0.3 and 0.45 monolayer, where monolayer refers to the number of Pt surface atoms. In this coverage range the heat of adsorption at 120 K exceeds the 298 K value by about 6 to 8 kJ/mol on average. The excess is particularly high, being 14 to 22 kJ/mol between coverages of 0.37 and 0.39 ML. The possible effect in the heat of adsorption at coverages between 0.3 and 0.45 monolayer may be rationalized by the order-disorder transition of CO on Pt(111). Ordering only occurs below 270 K, and the build-up of the ordered structure at 120 K could release more energy upon adsorption than the unordered phase at 298 K. The derived initial heat of adsorption is compared to TDS data. A compatible desorption energy of about 124 to 133 kJ/mol, where the latter value is an upper limit, was derived by Redhead analysis, assuming a frequency factor of $10^{13}\,\mathrm{s}^{-1}$. Previously reported values for the heat of adsorption from indirect measurements coincide with the obtained value. The only deviating value was

obtained by single crystal adsorption calorimetry. The apparent discrepancy can be attributed to the reflectivity value used in the data evaluation. King *et al.* used a reflectivity of 0.66, instead of 0.73 as determined in this work. Correcting for the reflectivity yields $(145 \pm 6)\,\mathrm{kJ/mol}$ at 300 K.

Benzene adsorption on Pt(111) was investigated at 298 K. Energy and sticking probability data were obtained in a series of five independent measurements. The initial sticking probability was determined to be (0.82 ± 0.01) and stays essentially constant with increasing coverage. Near the saturation coverage, the sticking probability drops to 0.5 and levels off in an adsorption-desorption equilibrium, which establishes at a coverage of about $2.25 \cdot 10^{14}\,\mathrm{molecules \cdot cm^{-2}}$. This saturation coverage is in good agreement with earlier studies. In the adsorption-desorption equilibrium regime, benzene desorption, i.e. the dissipation of energy from the system, is clearly indicated in the calorimetry data after the beam pulse ended. The initial heat of adsorption was derived to be $(119 \pm 3)\,\mathrm{kJ/mol}$ and decreases linearly with increasing coverage. A deviating value was obtained by single crystal adsorption calorimetry. The significantly higher adsorption energy of 197 kJ/mol determined by Ihm *et al.* is difficult to rationalize. The magnitude of the difference can not be understood by the stated systematic errors and may point to the necessity to put more effort into the precise analysis of systematic errors.

Particle Size dependent Heat of Adsorption for Carbon Monoxide on Pd Particles supported on Fe_3O_4/Pt(111) at 298 K

The heat of adsorption for carbon monoxide on Pd particles was determined as a function of particle size at 298 K. The Fe_3O_4 supported Pd particles were characterized previously, and exhibit mainly (111) facets and also (100) facets. Based on an earlier STM study, the mean diameter of the particles was varied between 1.8 to 8 nm. The adsorption on Pd(111) was also studied as a reference for extended surfaces. Prior to the adsorption measurements the optical reflectivities were determined, ranging from 0.717 for Pd(111) to 0.682 for the 8 nm Pd particles supported on the thin iron oxide film. Energy and sticking probability data were obtained. For each particle size, a series of at least four independent measurements was performed on freshly prepared Pd particles. Potential contaminations of the particles and the Pd(111) surface were studied by TDS. Only minute amounts of CO amounting to 1 to 2% of the saturation coverage were found. The initial heat of adsorption on Pd(111) was determined to be $(149 \pm 4)\,\mathrm{kJ/mol}$. For all particles sizes, the initial heats of adsorption are smaller than on Pd(111). It was also found that the initial heats of adsorption monotonously decreases for particles smaller than 8 nm. At the smallest particle size of 1.8 nm the initial heat of adsorption amounts to $(106 \pm 2)\,\mathrm{kJ/mol}$. The significant reduction of the initial heat of adsorption by about 40 kJ/mol can be rationalized by two contributions arising from chemisorption and Van der Waals interaction:

- Firstly, the overlap of the electron wave functions of the Pd surface and CO may be decreased. Previously published data on the lattice constant and the electronic structure of Pd particles indicate that the particle contracts with decreasing diameter and that the binding energies of their core electrons shift to higher energies. The correlation of decreasing CO adsorption energy with decreasing lattice constant was also observed in theoretical

calculations.

- Secondly, the reduced number of free electrons in small particles results in a decreasing polarizability, affecting the Van der Waals interaction strength. Previously, a decreasing Van der Waals interaction with decreasing Pd particle size was observed for physisorbed methane.

The different contributions in the interaction of CO with Pd particles can not be disentangled by adsorption microcalorimetry. A more detailed understanding would need comprehensive theoretical modeling.

In conclusion, detailed quantitative correlations of catalyst structures and adsorption energies represent important informations to understand the adsorption and reaction processes on catalyst surfaces and are now accessible by a new single crystal adsorption calorimeter experiment. Further, these correlations represent relevant benchmarks for theoretical methods. Therefore, the obtained results and future works of the new adsorption calorimeter experiment will hopefully contribute considerably to the understanding of surface processes and their accurate theoretical description.

Bibliography

[1] Gerhard Ertl, Helmut Knözinger, Ferdi Schüth, and Jens Weitkamp. *Handbook of Heterogeneous Catalysis*. Wiley-VCH Verlag GmbH & Co. KGaA, 2008.

[2] J.M. Thomas. *Principle and Practice of Heterogeneous Catalysis*. Wiley-VCH Verlag GmbH & Co. KGaA, 1997.

[3] J. Weitkamp G. Ertl, H. Knoezinger. *Environmental Catalysis*. Wiley-VCH Verlag GmbH & Co. KGaA, 1999.

[4] M. Boudart. Catalysis by supported metals. *Advances in Catalysis*, 20:153 – 166, 1969. doi: 10.1016/S0360-0564(08)60271-0. URL http://dx.doi.org/10.1016/S0360-0564(08)60271-0.

[5] Geoffrey C. Bond. The origins of particle size effects in heterogeneous catalysis. *Surface Science*, 156(Part 2):966 – 981, 1985. doi: 10.1016/0039-6028(85)90273-0. URL http://dx.doi.org/10.1016/0039-6028(85)90273-0.

[6] Michel Che and Carroll O. Bennett. The influence of particle size on the catalytic properties of supported metals. *Advances in Catalysis*, 36:55 – 172, 1989. doi: 10.1016/S0360-0564(08)60017-6. URL http://dx.doi.org/10.1016/S0360-0564(08)60017-6.

[7] Geoffrey C. Bond. Supported metal catalysts: some unsolved problems. *Chemical Society Reviews*, 20:441–475, 1991. doi: 10.1039/CS9912000441. URL http://dx.doi.org/10.1039/CS9912000441.

[8] Claude R. Henry. Surface studies of supported model catalysts. *Surf. Sci. Rep.*, 31:231–325, 1998. doi: 10.1016/S0167-5729(98)00002-8. URL http://dx.doi.org/10.1016/S0167-5729(98)00002-8.

[9] C.C. Kao, S.C. Tsai, M.K. Bahl, Y.W. Chung, and W.J. Lo. Electronic properties, structure and temperature-dependent composition of nickel deposited on rutile titanium dioxide (110) surfaces. *Surface Science*, 95(1):1 – 14, 1980. doi: 10.1016/0039-6028(80)90126-0. URL http://dx.doi.org/10.1016/0039-6028(80)90126-0.

[10] Gianfranco Pacchioni and Notker Rösch. Modeling of supported metal clusters: a density functional study of CO chemisorption on Ni clusters deposited on alumina. *Surf. Sci.*, 306:169–178, 1994. doi: 10.1016/0039-6028(94)91195-9.

[11] R. Persaud and T.E. Madey. *The Chemical Physics of Solid Surfaces and Heterogeneous Catalysis*, chapter 8. Elsevier Amsterdam, 1997.

[12] Helmut Poppa. Model studies in catalysis with uhv-deposited metal particles and clusters. *Vacuum*, 34:1081–1095, 1984. doi: 10.1016/0042-207X(84)90228-8. URL http://dx.doi.org/10.1016/0042-207X(84)90228-8.

[13] T. Engel. A molecular beam investigation of He, CO, and O_2 scattering from Pd(111). *J. Chem. Phys.*, 69:373, 1978. doi: 10.1063/1.436363. URL http://dx.doi.org/10.1063/1.436363.

[14] Gerhard Ertl. Elementary steps in heterogeneous catalysis. *Angewandte Chemie International Edition in English*, 29:1219 – 1227, 1990. doi: 10.1002/anie.199012191.

[15] H.-J. Freund. Adsorption of gases on complex solid surfaces. *Angewandte Chemie International Edition*, 36:452 – 475, 1997. doi: 10.1002/anie.199704521. URL http://dx.doi.org/10.1002/anie.199704521.

[16] H.-J. Freund, N. Ernst, T. Risse, H. Hamann, and G. Rupprechter. Model in heterogeneous catalysis: Surface science quo vadis? *physica status solidi (a)*, 187: 257 – 274, 2001. doi: 10.1002/1521-396X(200109)187:1<257::AID-PSSA257>3.0.CO;2-9. URL http://dx.doi.org/10.1002/1521-396X(200109)187:1<257::AID-PSSA257>3.0.CO;2-9.

[17] H.-J. Freund. Model studies on heterogeneous catalysts at the atomic level. *Catalysis Today*, 100(1-2):3 – 9, 2005. doi: 10.1016/j.cattod.2004.12.021. URL http://dx.doi.org/10.1016/j.cattod.2004.12.021. 100th Anniversary Issue.

[18] H.-J. Freund. Models for oxidation catalyst: Characterization and reaction at the atomic level. *Catalysis Today*, 117(1-3):6 – 14, 2006. doi: 10.1016/j.cattod.2006.05.043. URL http://dx.doi.org/10.1016/j.cattod.2006.05.043. The 5th World Congress on Oxidation Catalysis.

[19] H.-J. Freund. Model systems in heterogeneous catalysis: Selectivity studies at the atomic level. *Topics in Catalysis*, 48:137–144, 2008. doi: 10.1007/s11244-008-9052-9. URL http://dx.doi.org/10.1007/s11244-008-9052-9.

[20] H.-J. Freund. Model studies in heterogeneous catalysis. *Chemistry - A European Journal*, 2010. doi: 10.1002/chem.201001724. URL http://dx.doi.org/10.1002/chem.201001724.

[21] C. Duriez, C.R. Henry, and C. Chapon. Molecular-beam study of the chemisorption of CO on well shaped palladium particles epitaxially oriented on MgO(100). *Surf. Sci.*, 253: 190–204, 1991. doi: 10.1016/0039-6028(91)90592-G. URL http://dx.doi.org/10.1016/0039-6028(91)90592-G.

[22] I. Stará and V. Matolín. The influence of particle size on CO adsorption on Pd/alumina model catalysts. *Surf. Sci.*, 313:99–106, 1994. doi: 10.1016/0039-6028(94)91159-2. URL http://dx.doi.org/10.1016/0039-6028(94)91159-2.

[23] M. Kovár and S. Cerný. An attempt at the measurement of heat of adsorption by means of a pyroelectric detector. In *Proc. Conf. Assoc. France Calorim. Anal. Therm.*, pages 97–102, 1990.

[24] C. E. Borroni-Bird and D. A. King. An ultrahigh vacuum single crystal adsorption microcalorimeter. *Rev. Sci. Instrum.*, 62(9):2177–2185, 1991. doi: 10.1063/1.1142525. URL http://link.aip.org/link/?RSI/62/2177/1.

[25] W.A. Brown, R. Kose, and D.A. King. Femtomole adsorption calorimetry on single-crystal surfaces. *Chemical reviews*, 98(2):797–831, 1998. doi: 10.1021/cr9700890. URL http://pubs.acs.org/doi/full/10.1021/cr9700890.

[26] J. Stuckless, N.A. Frei, and C.T. Campbell. A novel single-crystal adsorption calorimeter and additions for determining metal adsorption and adhesion energies. *Rev. Sci. Instrum.*, 69(6):2427–2438, 1998. doi: 10.1063/1.1148971. URL http://dx.doi.org/10.1063/1.1148971.

[27] Ib Chorkendorff and Hans Niemantsverdriet. *Concepts of Modern Catalysis and Kinetics*. Wiley-VCH Verlag GmbH & Co. KGaA, 2007.

[28] Anders Nilsson and Lars G.M. Pettersson. Adsorbate electronic structure and bonding on metal surfaces. In *Chemical Bonding at Surfaces and Interfaces*, pages 57 – 142. Elsevier, Amsterdam, 2008. ISBN 978-0-44-452837-7. doi: 10.1016/B978-044452837-7.50003-4. URL http://dx.doi.org/10.1016/B978-044452837-7.50003-4.

[29] George Blyholder. Molecular orbital view of chemisorbed carbon monoxide. *J. Phys. Chem.*, 68:2772 – 2777, 1964. doi: 10.1021/j100792a006. URL http://dx.doi.org/10.1021/j100792a006.

[30] Jose A. Rodriguez and D. Wayne Goodman. The nature of the metal-metal bond in bimetallic surfaces. *Science*, 257(5072):897–903, 1992. doi: 10.1126/science.257.5072.897. URL http://www.sciencemag.org/cgi/content/abstract/257/5072/897.

[31] Alfred Clark. *The Theory of adsorption and catalysis*. Academic Press, 1970.

[32] Gerd Wedler. *Adsorption*. Verlag Chemie, 1970.

[33] William Arthur Steele. *The Interaction og Gases with Solid Surfaces*. Pergamon Press, 1974.

[34] Klaus Christmann. *Introduction to Surface Physical Chemistry*. Steinkopff Verlag GmbH Darmstadt, 1991.

[35] Hans-Joachim Freund. *Handbook of Heterogeneous Catalysis*, chapter 5, pages 1375 – 1415. Wiley-VCH Verlag GmbH & Co. KGaA, 2008. doi: 10.1002/9783527610044.hetcat0075. URL http://dx.doi.org/10.1002/9783527610044.hetcat0075.

[36] J. T. Stuckless, N. Al-Sarraf, C. Wartnaby, and D. A. King. Calorimetric heats of adsorption for CO on nickel single crystal surfaces. *The Journal of Chemical Physics*, 99(3): 2202–2212, 1993. doi: 10.1063/1.465282. URL http://link.aip.org/link/?JCP/99/2202/1.

[37] John L. Falconer and James A. Schwarz. Temperature-programmed desorption and reaction: Applications to supported catalysts. *Catalysis Reviews*, 25:141 – 227, 1983. doi: 10.1080/01614948308079666. URL http://dx.doi.org/10.1080/01614948308079666.

[38] A.M. de Jong and J.W. Niemantsverdriet. Thermal desorption analysis: Comparative test of ten commonly applied procedures. *Surface Science*, 233(3):355 – 365, 1990. doi: 10.1016/0039-6028(90)90649-S. URL http://dx.doi.org/10.1016/0039-6028(90)90649-S.

[39] P.A. Redhead. Thermal desorption of gases. *Vacuum*, 12(4):203 – 211, 1962. doi: 10.1016/0042-207X(62)90978-8. URL http://dx.doi.org/10.1016/0042-207X(62)90978-8.

[40] E. Habenschaden and J. Küppers. Evaluation of flash desorption spectra. *Surface Science*, 138(1):L147 – L150, 1984. doi: 10.1016/0039-6028(84)90488-6. URL http://dx.doi.org/10.1016/0039-6028(84)90488-6.

[41] David A. King. Thermal desorption from metal surfaces: A review. *Surface Science*, 47 (1):384 – 402, 1975. doi: 10.1016/0039-6028(75)90302-7. URL http://dx.doi.org/10.1016/0039-6028(75)90302-7. Proceedings of the Third Symposium on Surface Physics University of Utrecht, The Netherlands 26-28 June 1974.

[42] Kurt W. Kolasinski. *Surface Science*. Wiley-VCH Verlag GmbH, 2004.

[43] C.T. Campbell, G. Ertl, H. Kuipers, and J. Segner. A molecular beam investigation of the interactions of CO with a Pt(111) surface. *Surf. Sci.*, 107:207–219, 1981. doi: 10.1016/0039-6028(81)90621-X. URL http://dx.doi.org/10.1016/0039-6028(81)90621-X.

[44] Laurens K. Verheij, Joachim Lux, A.Brad Anton, Bene Poelsema, and George Comsa. A molecular beam study of the interaction of co molecules with a pt(111) surface using pulse shape analysis. *Surface Science*, 182(3):390 – 410, 1987. doi: 10.1016/0039-6028(87)90008-2. URL http://dx.doi.org/10.1016/0039-6028(87)90008-2.

[45] D. King and M.G. Wells. Molecular-beam investigation of adsorption kinetics on bulk metal target - nitrogen on tungsten. *Surf. Sci.*, 29(2):454 – 482, 1972. doi: 10.1016/0039-6028(72)90232-4. URL http://dx.doi.org/10.1016/0039-6028(72)90232-4.

[46] J. M. Burgers. *The nonlinear diffusion equation*. D. Reidel Pub. Co., 1974. ISBN 9027704945.

[47] J.A. Dumesic, D.F. Rudd, L.M. Aparicio, J.E. Rekoske, and A.A. Trevino. *The Microkinetics of Heterogeneous Catalysis*. Wiley-Vch, 1993. ISBN 0-8412-2214-2.

[48] Cyril Norman Hinshelwood. *The Kinetics Of Chemical Change*. Clarendon Press, 1940. URL http://ia331306.us.archive.org/0/items/kineticsofchemic030965mbp/kineticsofchemic030965mbp.pdf.

[49] D. D. Eley and E. K. Rideal. Parahydrogen conversion on tungsten. *Nature*, 146: 401 – 402, 1940. doi: 10.1038/146401d0. URL http://dx.doi.org/10.1038/146401d0.

[50] A. Winkler. Interaction of atomic hydrogen with metal surfaces. *Applied Physics A: Materials Science & Processing*, 67:637–644, 1998. doi: 10.1007/s003390050835. URL http://www.springerlink.com/content/y1416ugg19vftppj/.

[51] Z.-H. Qin, M. Lewandowski, Y.-N. Sun, S. Shaikhutdinov, and H.-J. Freund. Encapsulation of Pt nanoparticles as a result of strong metal-support interaction with $Fe_3O_4(111)$. *J. Phys. Chem. C*, 112:10209–10213, 2008. doi: 10.1021/jp801756q. URL http://dx.doi.org/10.1021/jp801756q.

[52] V. Matolin and E. Gillet. The surface diffusion in CO oxidation on small supported Pd particles: Experimental evidence. *Surface Science*, 166(1):L115 – L118, 1986. doi: 10.1016/0039-6028(86)90520-0. URL 10.1016/0039-6028(86)90520-0.

[53] Y.-N. Sun, Z.-H. Qin, M. Lewandowski, E. Carrasco, M. Sterrer, S. Shaikhutdinov, and H.-J. Freund. Monolayer iron oxide film on platinum promotes low temperature co oxidation. *Journal of Catalysis*, 266(2):359 – 368, 2009. doi: 10.1016/j.jcat.2009.07.002. URL http://dx.doi.org/10.1016/j.jcat.2009.07.002.

[54] B. Brandt, Y. Sun, J.-H. Fischer-Wolfarth, J. Libuda, S. Shaikhutdinov, S. Schauermann, and H.-J. Freund. Methanol dissociation on $Fe_3O_4(111)$ model oxide film. in preparation, 2010.

[55] K. Højrup Hansen, Z. Sljivancanin, E. Lægsgaard, F. Besenbacher, and I. Stensgaard. Adsorption of oxygen and NO on Pd nanocrystals supported on Al_2O_3/NiAl(110): overlayer and edge structures. *Surface Science*, 505:25 – 38, 2002. doi: 10.1016/S0039-6028(02)01437-1. URL http://dx.doi.org/10.1016/S0039-6028(02)01437-1.

[56] L.D. Landau and E.M. Lifshitz. *Statistical Physics,*. Pergamon Press, Oxford, 1993.

[57] A. I. Rusanov. Thermodynamics of solid surfaces. *Surface Science Reports*, 23(6-8):173 – 247, 1996. doi: 10.1016/0167-5729(95)00007-0. URL http://dx.doi.org/10.1016/0167-5729(95)00007-0.

[58] R Kubo, A Kawabata, and S Kobayashi. Electronic properties of small particles. *Annual Review of Materials Science*, 14(1):49–66, 1984. doi: 10.1146/annurev.ms.14.080184.000405. URL http://arjournals.annualreviews.org/doi/abs/10.1146/annurev.ms.14.080184.000405.

[59] C. N. R. Rao, Kulkarni G. U., P. John Thomas, and Peter P. Edwards. Size-dependent chemistry: Properties of nanocrystals. *Chemistry - A European Journal*, 8:28 – 35, 2001. doi: 10.1002/1521-3765(20020104)8:1<28::AID-CHEM28>3.0.CO;2-B. URL http://dx.doi.org/10.1002/1521-3765(20020104)8:1<28::AID-CHEM28>3.0.CO;2-B.

[60] V. P. Zhdanov and B. Kasemo. Kinetics of rapid reactions on nanometer catalyst particles. *Phys. Rev. B*, 55(7):4105–4108, Feb 1997. doi: 10.1103/PhysRevB.55.4105. URL http://link.aps.org/doi/10.1103/PhysRevB.55.4105.

[61] V. P. Zhdanov and B. Kasemo. Kinetics of rapid heterogeneous reactions on the nanometer scale. *Journal of Catalysis*, 170(2):377 – 389, 1997. doi: 10.1006/jcat.1997.1747. URL http://dx.doi.org/10.1006/jcat.1997.1747.

[62] V. P. Zhdanov and B. Kasemo. Monte carlo simulation of the kinetics of rapid reactions on nanometer catalyst particles. *Surface Science*, 405(1):27 – 37, 1998. doi: 10.1016/S0039-6028(97)01078-9. URL http://dx.doi.org/10.1016/S0039-6028(97)01078-9.

[63] Slavoj Cerný. Adsorption microcalorimetry in surface science studies sixty years of its development into a modern powerful method. *Surface Science Reports*, 26(1-2):1 – 59, 1996. doi: 10.1016/S0167-5729(96)00008-8. URL http://dx.doi.org/10.1016/S0167-5729(96)00008-8.

[64] H. Preston-Thomas. The international temperature scale of 1990. *Metrologia*, 27:3–10, 1990. doi: 10.1088/0026-1394/27/1/002.

[65] H Kraus. Superconductive bolometers and calorimeters. *Superconductor Science and Technology*, 9(10):827–842, 1996. URL http://stacks.iop.org/0953-2048/9/827.

[66] B. Cabrera, R. M. Clarke, P. Colling, A. J. Miller, S. Nam, and R. W. Romani. Detection of single infrared, optical, and ultraviolet photons using superconducting transition edge sensors. *Applied Physics Letters*, 73(6):735–737, 1998. doi: 10.1063/1.121984. URL http://link.aip.org/link/?APL/73/735/1.

[67] Markus Marksteiner, Alexander Divochiy, Michele Sclafani, Philipp Haslinger, Hendrik Ulbricht, Alexander Korneev, Alexander Semenov, Gregory Gol'tsman, and Markus Arndt. A superconducting NbN detector for neutral nanoparticles. *Nanotechnology*, 20(45):455501 (6pp), 2009. doi: 10.1088/0957-4484/20/45/455501. URL http://stacks.iop.org/0957-4484/20/455501.

[68] D. W. Denlinger, E. N. Abarra, Kimberly Allen, P. W. Rooney, M. T. Messer, S. K. Watson, and F. Hellman. Thin film microcalorimeter for heat capacity measurements from 1.5 to 800 K. *Review of Scientific Instruments*, 65(4):946–959, 1994. doi: 10.1063/1.1144925. URL http://link.aip.org/link/?RSI/65/946/1.

[69] Fernando Fominaya, Thierry Fournier, Philippe Gandit, and Jacques Chaussy. Nanocalorimeter for high resolution measurements of low temperature heat capacities of thin films and single crystals. *Review of Scientific Instruments*, 68(11):4191–4195, 1997. doi: 10.1063/1.1148366. URL http://link.aip.org/link/?RSI/68/4191/1.

[70] S. L. Lai, G. Ramanath, L. H. Allen, P. Infante, and Z. Ma. High-speed scanning microcalorimetry with monolayer sensitivity. *Applied Physics Letters*, 67(9):1229–1231, 1995. doi: 10.1063/1.115016. URL http://link.aip.org/link/?APL/67/1229/1.

[71] S. L. Lai, G. Ramanath, L. H. Allen, and P. Infante. Heat capacity measurements of Sn nanostructures using a thin-film differential scanning calorimeter with 0.2 nJ sensitivity. *Applied Physics Letters*, 70(1):43–45, 1997. doi: 10.1063/1.119299. URL http://link.aip.org/link/?APL/70/43/1.

[72] G. Wedler. Elektronische Wechselwirkung und Adsorptionswärme bei der Chemisorption von Gasen an aufgedampften Metallfilmen. *Zeitschrift für physikalische Chemie - Frankfurt/*, 24:73, 1960.

[73] D. A. Kyser and R. I. Masel. Development of single-crystal adsorption calorimetry. *Journal of Vacuum Science & Technology A: Vacuum, Surfaces, and Films*, 4(3):1431–1432, May 1986. doi: 10.1116/1.573529. URL http://link.aip.org/link/?JVA/4/1431/1.

[74] R. Masel and Kyser. Design of a calorimeter capable of measuring heats of adsorption on single-crystal surfaces. *Rev. Sci. Instrum.*, 58(11):2141–2144, 1987. doi: 10.1063/1.1139477. URL http://link.aip.org/link/?RSINAK/58/2141/1.

[75] J. R. Barnes, R. J. Stephenson, C. N. Woodburn, S. J. O'Shea, M. E. Welland, T. Rayment, J. K. Gimzewski, and Ch. Gerber. A femtojoule calorimeter using micromechanical sensors. *Review of Scientific Instruments*, 65(12):3793–3798, 1994. doi: 10.1063/1.1144509. URL http://link.aip.org/link/?RSI/65/3793/1.

[76] J. K. Gimzewski, Ch. Gerber, E. Meyer, and R. R. Schlittler. Observation of a chemical reaction using a micromechanical sensor. *Chemical Physics Letters*, 217(5-6):589 – 594, 1994. doi: 10.1016/0009-2614(93)E1419-H. URL http://dx.doi.org/10.1016/0009-2614(93)E1419-H.

[77] T. Bachels, F. Tiefenbacher, and R. Schäfer. Condensation of isolated metal clusters studied with a calorimeter. *The Journal of Chemical Physics*, 110(20):10008–10015, 1999. doi: 10.1063/1.478874. URL http://link.aip.org/link/?JCP/110/10008/1.

[78] JM Antonietti, J Gong, V Habibpour, MA Rottgen, S Abbet, CJ Harding, M Arenz, U Heiz, and C Gerber. Micromechanical sensor for studying heats of surface reactions, adsorption, and cluster deposition processes. *Rev. Sci. Instrum.*, 78(5):054101, May 2007. doi: 10.1063/1.2740165. URL http://dx.doi.org/10.1063/1.2740165.

[79] Thomas Bachels, Hans-Joachim Güntherodt, and Rolf Schäfer. Melting of isolated tin nanoparticles. *Phys. Rev. Lett.*, 85(6):1250–1253, Aug 2000. doi: 10.1103/PhysRevLett.85.1250. URL http://link.aps.org/doi/10.1103/PhysRevLett.85.1250.

[80] Christian Punckt, Pablo S. Bodega, and Harm Hinrich Rotermund. Quantitative measurement of the deformation of ultra-thin platinum foils during adsorption and reaction of CO and oxygen. *Surface Science*, 600(16):3101 – 3109, 2006. doi: 10.1016/j.susc.2006.04.031. URL http://dx.doi.org/10.1016/j.susc.2006.04.031.

[81] N Alsarraf, J.T. Stuckless, C.E. Wartnaby, and D.A. King. Adsorption microcalorimetry and sticking probabilities on metal single-crystal surfaces. *Surf. Sci.*, 283(1-3):427–437, 1993. doi: 10.1016/0039-6028(93)91015-H. URL http://dx.doi.org/10.1016/0039-6028(93)91015-H.

[82] A. Stuck, C.E. Wartnaby, Y.Y. Yeo, J.T. Stuckless, N. Alsarraf, and D.A. King. An improved single crystal adsorption calorimeter. *Surf. Sci.*, 349(2):229–240, 1996. doi: 10.1016/0039-6028(95)01070-X. URL http://dx.doi.org/10.1016/0039-6028(95)01070-X.

[83] V. Fiorin, Karmazyn, and D. A. King. Calorimetric studies of NO on Ni(211): criteria for switching from dissociative to molecular adsorption. *Surf. Sci.*, 547(1-2):184–192, 2003. doi: 10.1016/j.susc.2003.09.030. URL http://dx.doi.org/10.1016/j.susc.2003.09.030.

[84] Y Yeo, L. Vattuone, and D.A. King. Energetics and kinetics of CO and NO adsorption on Pt(100): Restructuring and lateral interactions. *J. Chem. Phys.*, 104(10):3810–3821, 1996. doi: 10.1063/1.471034. URL http://dx.doi.org/10.1063/1.471034.

[85] Y. Yeo, L. Vattuone, and D.A. King. Calorimetric investigation of NO and CO adsorption on Pd(100) and the influence of preadsorbed carbon. *J. Chem. Phys.*, 106(5):1990–1996, 1997. doi: 10.1063/1.473306. URL http://dx.doi.org/10.1063/1.473306.

[86] W. Brown and Kose. Calorimetric heats of dissociative adsorption for oxygen on Rh(100). *Surf. Sci.*, 402(1-3):856–860, 1998. doi: 10.1016/S0039-6028(97)01027-3. URL http://dx.doi.org/10.1016/S0039-6028(97)01027-3.

[87] David Borthwick, Vittorio Fiorin, Stephen J. Jenkins, and David A. King. Facile dissociation of CO on Fe(211): Evidence from microcalorimetry and first-principles theory. *Surface Science*, 602(13):2325 – 2332, 2008. doi: 10.1016/j.susc.2008.05.014. URL http://dx.doi.org/10.1016/j.susc.2008.05.014.

[88] C. E. Wartnaby, A. Stuck, Y. Y. Yeo, and D. A. King. Microcalorimetric heats of adsorption for CO, NO, and oxygen on Pt(110). *Journal of Physical Chemistry*, 100(30):12483–12488, January 1996. doi: 10.1021/jp953624d. URL http://dx.doi.org/10.1021/jp953624d.

[89] R. Kose, Brown, and D. A. King. Calorimetric measurements of the adsorption heat for ethene on Pt(211) and Pt(311). *Surf. Sci.*, 440(1-2):271–278, 1999. doi: 10.1016/S0039-6028(99)00814-6. URL http://dx.doi.org/10.1016/S0039-6028(99)00814-6.

[90] Vittorio Fiorin, David Borthwick, and David A. King. Microcalorimetry of oxygen and NO on flat and stepped platinum surfaces. *Surface Science*, 603(10-12):1360 – 1364, 2009. doi: 10.1016/j.susc.2008.08.034. URL http://dx.doi.org/10.1016/j.susc.2008.08.034. Special Issue of Surface Science dedicated to Prof. Dr. Dr. h.c. mult. Gerhard Ertl, Nobel-Laureate in Chemistry 2007.

[91] D. King and Alsarraf. Calorimetric adsorbation heats on low-index nickel surfaces. *Surf. Sci.*, 307:1–7, 1994. doi: 10.1016/0039-6028(94)90361-1. URL http://dx.doi.org/10.1016/0039-6028(94)90361-1.

[92] M. Kovár, L. Dvorák, and S. Cerný. Application of pyroelectric properties of LiTaO3 single crystal to microcalorimetric measurement of the heat of adsorption. *Applied Surface Science*, 74(1):51 – 59, 1994. doi: 10.1016/0169-4332(94)90099-X. URL 10.1038/146401d010.1016/0039-6028(94)90361-1.

[93] L. Dvorák, M. Kovár, and S. Cerný. A new approach to adsorption microcalorimetry based on a LiTaO3 pyroelectric temperature sensor and a pulsed molecular beam. *Thermochimica Acta*, 245:163 – 171, 1994. doi: 10.1016/0040-6031(94)85076-3. URL http://dx.doi.org/10.1016/0040-6031(94)85076-3.

[94] M. Simhony and A. Shaulov. Pyroelectric voltage response to step signals of infrared radiation in triglycine sulphate and strontium-barium niobate. *Journal of Applied Physics*, 42(10):3741–3744, 1971. doi: 10.1063/1.1659679. URL http://link.aip.org/link/?JAP/42/3741/1.

[95] A. Shaulov and M. Simhony. Pyroelectric voltage response to rectangular infrared signals in triglycine sulphate and strontium-barium niobate. *Journal of Applied Physics*, 43(4):1440–1444, 1972. doi: 10.1063/1.1661338. URL http://link.aip.org/link/?JAP/43/1440/1.

[96] M. Simhony, A. Shaulov, and A. Maman. Temperature dependence of the pyroelectric voltage response to step infrared signals in triglycine sulphate. *Journal of Applied Physics*, 44(6):2464–2469, 1973. doi: 10.1063/1.1662598. URL http://link.aip.org/link/?JAP/44/2464/1.

[97] H. Coufal and P. Hefferle. Thermal diffusivity measurements of thin films with a pyroelectric calorimeter. *Applied Physics A: Materials Science & Processing*, 38:213–219, 1985. doi: 10.1007/BF00616499. URL http://dx.doi.org/10.1007/BF00616499.

[98] H. Coufal and W. Lee. Time resolved calorimetry of te films during pulsed laser annealing. *Applied Physics B Photophysics and Laser Chemistry*, 44(2):141, 1987. doi: 10.1007/BF00694207. URL http://dx.doi.org/10.1007/BF00694207.

[99] Hans J. Coufal, Robert K. Grygier, Donald E. Horne, and Jacob E. Fromm. Pyroelectric calorimeter for photothermal studies of thin films and adsorbates. *Journal of Vacuum Science & Technology A: Vacuum, Surfaces, and Films*, 5(5):2875–2889, 1987. doi: 10.1116/1.574258. URL http://link.aip.org/link/?JVA/5/2875/1.

[100] Joan F. Power and Andreas Mandelis. Photopyroelectric thin-film instrumentation and impulse-response detection. Part I: A theoretical model. *Rev. Sci. Instrum.*, 58(11):2018–2023, 1987. doi: 10.1063/1.1139509. URL http://link.aip.org/link/?RSI/58/2018/1.

[101] Joan F. Power and Andreas Mandelis. Photopyroelectric thin-film instrumentation and impulse-response detection. Part II: Methodology. *Rev. Sci. Instrum.*, 58(11):2024–2032, 1987. doi: 10.1063/1.1139510. URL http://link.aip.org/link/?RSI/58/2024/1.

[102] Joan F. Power and Andreas Mandelis. Photopyroelectric thin-film instrumentation and impulse-response detection. Part III: Performance and signal recovery techniques. *Review of Scientific Instruments*, 58(11):2033–2043, 1987. doi: 10.1063/1.1139511. URL http://link.aip.org/link/?RSI/58/2033/1.

[103] S. G. Porter. A brief guide to pyroelectric detectors. *Ferroelectrics*, 33(1-4):193–206, 1981. doi: 10.1080/00150198108008086. URL http://www.informaworld.com/10.1080/00150198108008086.

[104] R W Whatmore. Pyroelectric devices and materials. *Reports on Progress in Physics*, 49:1335–1386, 1986. doi: 10.1088/0034-4885/49/12/002. URL http://dx.doi.org/10.1088/0034-4885/49/12/002.

[105] M.H. Lee, R. Guo, and A.S. Bhalla. Pyroelectric sensors. *Journal of Electroceramics*, 2:229–242, 1998. doi: 10.1023/A:1009922522642. URL http://dx.doi.org/10.1023/A:1009922522642.

[106] St. J. Dixon-Warren, M. Kovar, C. E. Wartnaby, and D. A. King. Pyroelectric single-crystal adsorption microcalorimetry at low-temperatures - oxygen on Ni(100). *Surf. Sci.*, 307:16–22, 1994. doi: 10.1016/0039-6028(94)90363-8. URL http://dx.doi.org/10.1016/0039-6028(94)90363-8.

[107] C Campbell, Stuckless JT, and Starr D. A new single-crystal adsorption microcalorimeter: Applications in metal film growth on oxides. *Abstracts of papers*, 213:292–COLL, 1997.

[108] H. M. Ajo, H. Ihm, D. E. Moilanen, and C. T. Campbell. Calorimeter for adsorption energies of larger molecules on single crystal surfaces. *Rev. Sci. Instrum.*, 75(11):4471–4480, November 2004. doi: 10.1063/1.1794391. URL http://rsi.aip.org/rsinak/v75/i11/p4471_s1.

[109] S. F. Diaz, J. F. Zhu, N. Shamir, and C. T. Campbell. Pyroelectric heat detector for measuring adsorption energies on thicker single crystals. *Sensors And Actuators B-*

Chemical, 107(1):454–460, May 2005. doi: 10.1016/j.snb.2004.11.037. URL http://dx.doi.org/10.1016/j.snb.2004.11.037.

[110] Wanda Lew, Ole Lytken, Jason A. Farmer, Matthew C. Crowe, and Charles T. Campbell. Improved pyroelectric detectors for single crystal adsorption calorimetry from 100 to 350 K. *Review of Scientific Instruments*, 81(2):024102, 2010. doi: 10.1063/1.3290632. URL http://link.aip.org/link/?RSI/81/024102/1.

[111] D. E. Starr, J. T. Stuckless, D. J. Bald, and Charles T. Campbell. Metal adsorption calorimetry and adhesion energies on clean single-crystal surfaces. *J. Chem. Phys.*, 107(14):5547–5553, 1997. doi: 10.1063/1.474230. URL http://link.aip.org/link/?JCPSA6/107/5547/1.

[112] D. E. Starr and C. T. Campbell. Low-temperature adsorption microcalorimetry: Pb on MgO(100). *J. Phys. Chem. B*, 105:3776–3782, 2001. doi: 10.1021/jp003411a. URL http://dx.doi.org/10.1021/jp003411a.

[113] J. H. Larsen, D. E. Starr, and C. T. Campbell. Enthalpies of adsorption of metal atoms on single-crystalline surfaces by microcalorimetry. *J. Chem. Thermodyn.*, 33(3):333–345, March 2001. doi: 10.1006/jcht.2000.0747. URL http://dx.doi.org/10.1006/jcht.2000.0747.

[114] C. Campbell, A.W.Grantand D.E. Starr, S.C. Parker, and V.A. Bondzie. Model oxide-supported metal catalysts: energetics, particle thicknesses, chemisorption and catalytic properties. *Top. Catal.*, 14(1-4):43–51, 2001. doi: 10.1023/A:1009002915667. URL http://dx.doi.org/10.1023/A:1009002915667.

[115] D. E. Starr, S. F. Diaz, J. E. Musgrove, J. T. Ranney, D. J. Bald, L. Nelen, H. Ihm, and C. T. Campbell. Heat of absorption of Cu and Pb on hydroxyl-covered MgO(100). *Surf. Sci.*, 515(1):13–20, August 2002. doi: 10.1016/S0039-6028(02)01915-5. URL http://dx.doi.org/10.1016/S0039-6028(02)01915-5.

[116] S.F. Diaz, J.F. Zhu, J.J.W. Harris, P. Goetsch, L.R. Merte, and Charles T. Campbell. Heats of adsorption of Pb on pristine and electron-irradiated poly(methyl methacrylate) by microcalorimetry. *Surface Science*, 598(1-3):22 – 34, 2005. doi: 10.1016/j.susc.2005.09.015. URL http://dx.doi.org/10.1016/j.susc.2005.09.015.

[117] H. Ihm, H. M. Ajo, J. M. Gottfried, P. Bera, and C. T. Campbell. Calorimetric measurement of the heat of adsorption of benzene on Pt(111). *J. Phys. Chem. B*, 108(38):14627–14633, September 2004. doi: 10.1021/jp040159o. URL http://pubs.acs.org/doi/full/10.1021/jp040159o.

[118] J. Michael Gottfried, Ebbe K. Vestergaard, Parthasarathi Bera, and Charles T. Campbell. Heat of adsorption of naphthalene on Pt(111) measured by adsorption calorimetry. *J. Phys. Chem. B*, 110:17539 – 17545, 2006. doi: 10.1021/jp062659i. URL http://dx.doi.org/10.1021/jp062659i.

[119] O Lytken, W Lew, JJW Harris, EK Vestergaard, JM Gottfried, and CT Campbell. Energetics of cyclohexene adsorption and reaction on Pt(111) by low-temperature microcalorimetry. *J. Am. Chem. Soc.*, 130(31):10247–10257, August 2008. doi: 10.1021/ja801856s. URL http://dx.doi.org/10.1021/ja801856s.

[120] C. Campbell and H. Gross. Metal-carbon bond energies for adsorbed hydrocarbons from calorimetric data. *Surf. Sci.*, 572(2-3):179–190, 2004. doi: 10.1016/j.susc.2004.08.015. URL http://dx.doi.org/10.1016/j.susc.2004.08.015.

[121] O. Lytken, W. Lew, and C. T. Campbell. Catalytic reaction energetics by single crystal adsorption calorimetry: hydrocarbons on Pt(111). *Chem. Soc. Rev.*, 37(10):2172–2179, October 2008. doi: 10.1039/b719543p. URL http://dx.doi.org/10.1039/b719543p.

[122] Charles T. Campbell and Ole Lytken. Experimental measurements of the energetics of surface reactions. *Surf. Sci.*, 603:1365–1372, 2009. doi: 10.1016/j.susc.2008.08.028. URL http://dx.doi.org/10.1016/j.susc.2008.08.028.

[123] Norman F. Ramsey. *Molecular Beams*. Oxford University Press, 1956.

[124] M. Zen and G. Scoles. *Atomic and Molecular Beam Methods*, volume 1. Oxford University Press, 1988.

[125] Hans Pauly. *Atom, Molecule and Cluster Beams 1: Basic theory, Production and Detection of Thermal Energy Beams*, volume 28 of *Springer series on atomic, optical and plasma physics*. Springer Berlin / Heidelberg, 2000.

[126] J.L. Falconer and R.J. Madix. Flash desorption activation energies: DCOOH decomposition and CO desorption from Ni(110). *Surface Science*, 48(2):393 – 405, 1975. doi: 10.1016/0039-6028(75)90414-8. URL http://dx.doi.org/10.1016/0039-6028(75)90414-8.

[127] Gerhard Ertl and Jürgen Küppers. *Low energy electrons and surface chemistry*. VCH, 2nd edition, 1985. ISBN 3-527-26056-0.

[128] Martin Henzler and Wolfgang Göpel. *Oberflächenphysik des Festkörpers*. B.G. Teubner Stuttgart, 2. auflage edition, 1994.

[129] D. P. Woodruff and T. A. Delchar. *Modern Techniques of Surface Science*. Cambridge Solid State Science Series. Cambridge University Press, 2nd edition edition, 1994. ISBN 521424984.

[130] Peter H. Dawson. *Quadrupole mass spectrometry and its applications*. AIP press, 1995.

[131] Wolfgang Bauer, Alexander Moldenhauer, and Hansjochen Oertel. Thermal radiation properties of different metals. In Jonathan J. Miles, G. Raymond Peacock, and Kathryn M. Knettel, editors, *Proc. SPIE*, page 62050E. SPIE, 2006. doi: 10.1117/12.683947. URL http://link.aip.org/link/?PSI/6205/62050E/1.

[132] Laurent Ibos, G. Teyssedre, A. Bernes, and C. Lacabanne. Thermal aging of pyroelectricity in PVDF and P(VDF-TrFE) copolymers. In Andrzej Wlochowicz, editor, *Proc. SPIE*, pages 29–36. SPIE, 1999. doi: 10.1117/12.373716. URL http://link.aip.org/link/?PSI/4017/29/1.

[133] L Ibos, A Bernes, and C Lacabanne. Annealing or storage influence on pyroelectricity of ferroelectric PVDF and P(VDF-TrFE) copolymer. *Ferroelectrics*, 320(1):15–489, 2005. doi: 10.1080/00150190590966739. URL http://dx.doi.org/10.1080/00150190590966739.

[134] Keithley. Low level measurements handbook; precision DC current, voltage, and resistance measurements, 2004.

[135] David R. Lide. *Handbook of Chemistry and Physics*. CRC Press, 90 edition, 2009. ISBN 9781420090840. URL http://www.crcpress.com/product/isbn/9781420090840.

[136] J. Libuda, I. Meusel I, J. Hartmann, and H.-J. Freund. A molecular beam/surface spectroscopy apparatus for the study of reactions on complex model catalysts. *Rev. Sci. Instrum.*, 71(12):4395–4408, 2000. doi: 10.1063/1.1318919. URL http://dx.doi.org/10.1063/1.1318919.

[137] Ying-Na Sun, Livia Giordano, Jacek Goniakowski, Mikolaj Lewandowski, Zhi-Hui Qin, Claudine Noguera, Shamil Shaikhutdinov, Gianfranco Pacchioni, and Hans-Joachim Freund. The interplay between structure and CO oxidation catalysis on metal-supported ultrathin oxide films. *Angewandte Chemie International Edition*, 49:4418 –4421, 2010. doi: 10.1002/anie.201000437. URL http://www3.interscience.wiley.com/journal/123438789/abstract.

[138] Charles Kittel. *Introduction to Solide State Physics*. John-Wiley & Sons, Inc, 8th edition, 2005.

[139] A. Y-C. Yu, W. E. Spicer, and G. Hass. Optical properties of platinum. *Phys. Rev.*, 171(3):834–835, Jul 1968. doi: 10.1103/PhysRev.171.834. URL http://link.aps.org/doi/10.1103/PhysRev.171.834.

[140] J. H. Weaver. Optical properties of Rh, Pd, Ir, and Pt. *Phys. Rev. B*, 11(4):1416–1425, Feb 1975. doi: 10.1103/PhysRevB.11.1416. URL http://link.aps.org/doi/10.1103/PhysRevB.11.1416.

[141] G. Ertl. Scattering of atomic and molecular beams at metal surfaces. *Surface Science*, 89(1-3):525 – 539, 1979. doi: 10.1016/0039-6028(79)90635-6. URL http://dx.doi.org/10.1016/0039-6028(79)90635-6.

[142] L.Q. Jiang, B.E. Koel, and J.L. Falconer. Effects of K, O, and H adatoms on the adsorption kinetics of CO on Pt(111). *Surf. Sci.*, 273(3):273 – 284, 1992. doi: 10.1016/0039-6028(92)90065-E. URL http://dx.doi.org/10.1016/0039-6028(92)90065-E.

[143] J. Liu, M. Xu, T. Nordmeyer, and F. Zaera. Sticking probabilities for CO adsorption on Pt(111) surfaces revisited. *J. Phys. Chem.*, 99:6167 – 6175, 1995. doi: 10.1021/j100016a062. URL http://pubs.acs.org/doi/abs/10.1021/j100016a062.

[144] Y. Yeo, L. Vattuone, and D.A. King. Calorimetric heats for CO and oxygen adsorption and for the catalytic CO oxidation reaction on Pt(111). *J. Chem. Phys.*, 106:392–401, 1997. doi: 10.1063/1.473203. URL http://jcp.aip.org/jcpsa6/v106/i1/p392_s1.

[145] R. A. Shigeishi and David A. King. Chemisorption of carbon monoxide on platinum (111): Reflection-absorption infrared spectroscopy. *Surface Science*, 58(2):379 – 396, 1976. doi: 10.1016/0039-6028(76)90477-5. URL http://dx.doi.org/10.1016/0039-6028(76)90477-5.

[146] H. Steininger, S. Lehwald, and H. Ibach. On the adsorption of CO on Pt(111). *Surf. Sci.*, 123(2-3):264 – 282, 1982. doi: 10.1016/0039-6028(82)90328-4. URL http://dx.doi.org/10.1016/0039-6028(82)90328-4.

[147] Bene Poelsema, Laurens K. Verheij, and George Comsa. He-scattering investigation of CO migration on Pt(111). *Phys. Rev. Lett.*, 49:1731 – 1735, 1982. doi: 10.1103/PhysRevLett.49.1731. URL http://link.aps.org/doi/10.1103/PhysRevLett.49.1731.

[148] J. E. Reutt-Robey, D. J. Doren, Y. J. Chabal, and S. B. Christman. Microscopic CO diffusion on a Pt(111) surface by time-resolved infrared spectroscopy. *Phys. Rev. Lett.*, 61:2778 – 2781, 1988. doi: 10.1103/PhysRevLett.61.2778. URL http://link.aps.org/doi/10.1103/PhysRevLett.61.2778.

[149] J. E. Reutt-Robey, D. J. Doren, Y. J. Chabal, and S. B. Christman. CO diffusion on Pt(111) with time-resolved infrared-pulsed molecular beam methods: Critical tests and analysis. *J. Chem. Phys.*, 93(12):9113–9129, 1990. doi: 10.1063/1.459202. URL http://link.aip.org/link/?JCP/93/9113/1.

[150] H. Froitzheim, H. Hopster, H. Ibach, and S. Lehwald. Adsorption sites of CO on Pt(111). *Applied Physics A: Materials Science & Processing*, 13:147–151, 1977. doi: 10.1007/BF00882473. URL http://dx.doi.org/10.1007/BF00882473.

[151] H. Froitzheim and M. Schulze. The kinetics of the adsorption and desorption of the system CO/Pt(111) derived from high resolution TREELS. *Surf. Sci.*, 211-212:837 – 843, 1989. doi: 10.1016/0039-6028(89)90848-0. URL http://dx.doi.org/10.1016/0039-6028(89)90848-0.

[152] H. Froitzheim and M. Schulze. Surface diffusion of CO on Pt(111): a HREELS study at high temperatures. *Surf. Sci.*, 320(1-2):85 – 92, 1994. doi: 10.1016/0039-6028(94)00498-6. URL http://dx.doi.org/10.1016/0039-6028(94)00498-6.

[153] V.J. Kwasniewski and L.D. Schmidt. Surface diffusion of CO on Pt(111). *Surf. Sci.*, 274 (3):329 – 340, 1992. doi: 10.1016/0039-6028(92)90838-W. URL http://dx.doi.org/10.1016/0039-6028(92)90838-W.

[154] Jianwei Ma, Xudong Xiao, N. J. DiNardo, and M. M. T. Loy. Diffusion of CO on Pt(111) studied by an optical diffraction method. *Phys. Rev. B*, 58(8):4977–4983, Aug 1998. doi: 10.1103/PhysRevB.58.4977. URL http://link.aps.org/doi/10.1103/PhysRevB.58.4977.

[155] Jianwei Ma, Lei Cai, Xudong Xiao, and Michael M. T. Loy. On the mechanism limiting CO diffusion perpendicular to steps on Pt(111). *Surf. Sci.*, 425(1):131 – 137, 1999. doi: 10.1016/S0039-6028(99)00201-0. URL http://dx.doi.org/10.1016/S0039-6028(99)00201-0.

[156] Jianwei Ma, Xudong Xiao, and M. M. T. Loy. Experimental study of surface diffusion rate enhancement along steps: CO on Pt(111). *Surf. Sci.*, 436(1-3):L661 – L665, 1999. doi: 10.1016/S0039-6028(99)00641-X. URL http://dx.doi.org/10.1016/S0039-6028(99)00641-X.

[157] C. M. Yim, K. L. Man, Xudong Xiao, and M. S. Altman. Low-energy electron microscopy of CO/Pt(111) surface diffusion by nonequilibrium coverage profile evolution. *Physical Review B (Condensed Matter and Materials Physics)*, 78(15):155439, 2008. doi: 10.1103/PhysRevB.78.155439. URL http://link.aps.org/abstract/PRB/v78/e155439.

[158] Gil Alexandrowicz, Pepijn R. Kole, Everett Y. M. Lee, Holly Hedgeland, Riccardo Ferrando, Andrew P. Jardine, William Allison, and John Ellis. Observation of uncorrelated microscopic motion in a strongly interacting adsorbate system. *J. Am. Chem. Soc.*, 130:6789 – 6794, 2008. doi: 10.1021/ja800118x. URL http://dx.doi.org/10.1021/ja800118x.

[159] A.P. Jardine, H. Hedgeland, G. Alexandrowicz, W. Allison, and J. Ellis. Helium-3 spin-echo: Principles and application to dynamics at surfaces. *Prog. Surf. Sci.*, 84:323–379, 2009. doi: 10.1016/j.progsurf.2009.07.001. URL http://dx.doi.org/10.1016/j.progsurf.2009.07.001.

[160] A. P. Jardine, G. Alexandrowicz, H. Hedgeland, W. Allison, and J. Ellis. Studying the microscopic nature of diffusion with helium-3 spin-echo. *Phys. Chem. Chem. Phys.*, 11:3355 – 3374, 2009. doi: 10.1039/b810769f. URL http://dx.doi.org/10.1039/b810769f.

[161] W. D. Mieher, L. J. Whitman, and W. Ho. A time resolved electron energy loss spectroscopy study of CO on Pt(111): Adsorption site occupations versus coverage and temperature. *J. Chem. Phys.*, 91(5):3228–3239, 1989. doi: 10.1063/1.456944. URL http://link.aip.org/link/?JCP/91/3228/1.

[162] A. Cudok, H. Froitzheim, and M. Schulze. Low-temperature adsorption kinetics of CO on Pt(111) derived from nonequilibrium time-resolved electron-energy-loss spectroscopy measurements. *Phys. Rev. B*, 47(20):13682–13686, May 1993. doi: 10.1103/PhysRevB.47.13682. URL http://link.aps.org/doi/10.1103/PhysRevB.47.13682.

[163] J.V. Nekrylova, C. French, A.N. Artsyukhovich, V.A. Ukraintsev, and I. Harrison. Low temperature adsorption of CO on Pt(111): disequilibrium and the occupation of three-fold hollow sites. *Surface Science Letters*, 295(1-2):L987 – L992, 1993. doi: 10.1016/0167-2584(93)91008-C. URL http://dx.doi.org/10.1016/0167-2584(93)91008-C.

[164] J. V. Nekrylova and I. Harrison. Single hop diffusion of CO from bridge to top sites on Pt(111). *J. Chem. Phys.*, 101:1730, 1994. doi: 10.1063/1.468435. URL http://link.aip.org/link/?JCPSA6/101/1730/1.

[165] J. V. Nekrylova and I. Harrison. Site resolved adsorption dynamics of CO on Pt(111). *Chem. Phys.*, 205(1-2):37 – 46, 1996. doi: 10.1016/0301-0104(95)00304-5. URL http://dx.doi.org/10.1016/0301-0104(95)00304-5. Surface Reaction Dynamics.

[166] Jun Yoshinobu and Maki Kawai. Initial adsorption sites of CO on Pt(111) and Ni(100) at low temperature. *Surf. Sci.*, 363(1-3):105 – 111, 1996. doi: 10.1016/0039-6028(96)00117-3. URL http://dx.doi.org/10.1016/0039-6028(96)00117-3.

[167] M. Kinne, T. Fuhrmann, C. M. Whelan, J. F. Zhu, J. Pantforder, M. Probst, G. Held, R. Denecke, and H.-P. Steinruck. Kinetic parameters of CO adsorbed on Pt(111) studied by in situ high resolution x-ray photoelectron spectroscopy. *J. Chem. Phys.*, 117(23):10852–10859, 2002. doi: 10.1063/1.1522405. URL http://link.aip.org/link/?JCP/117/10852/1.

[168] G. Ertl, M. Neumann, and K. M. Streit. Chemisorption of CO on the Pt(111) surface. *Surf. Sci.*, 64:393–410, 1977. doi: 10.1016/0039-6028(77)90052-8. URL http://dx.doi.org/10.1016/0039-6028(77)90052-8.

[169] B.E. Hayden and A.M. Bradshaw. The adsorption of CO on Pt(111) studied by infrared reflection–absorption spectroscopy. *Surf. Sci.*, 125(3):787 – 802, 1983. doi: 10.1016/S0039-6028(83)80060-0. URL http://dx.doi.org/10.1016/S0039-6028(83)80060-0.

[170] E. Schweizer, B.N.J. Persson, M. Tüshaus, D. Hoge, and A.M. Bradshaw. The potential energy surface, vibrational phase relaxation and the order-disorder transition in the adsorption system Pt(111)-CO. *Surf. Sci.*, 213(1):49 – 89, 1989. doi: 10.1016/0039-6028(89)90252-5. URL http://dx.doi.org/10.1016/0039-6028(89)90252-5.

[171] R. C. Baetzold, G. Apai, E. Shustorovich, and R. Jaeger. Surface core-level shifts for Pt single-crystal surfaces. *Phys. Rev. B*, 26(8):4022–4027, Oct 1982. doi: 10.1103/PhysRevB.26.4022. URL http://link.aps.org/doi/10.1103/PhysRevB.26.4022.

[172] D.M. Collins and W.E. Spicer. The adsorption of CO, oxygen, and hydrogen on Pt: I. Thermal desorption spectroscopy studies. *Surf. Sci.*, 69(1):85 – 113, 1977. doi: 10.1016/0039-6028(77)90163-7. URL http://dx.doi.org/10.1016/0039-6028(77)90163-7.

[173] R.W McCabe and L.D Schmidt. Binding states of CO and hydrogen on clean and oxidized Pt(111). *Surf. Sci.*, 65(1):189 – 209, 1977. doi: 10.1016/0039-6028(77)90301-6. URL http://dx.doi.org/10.1016/0039-6028(77)90301-6.

[174] P.R. Norton, J.W. Goodale, and E.B. Selkirk. Adsorption of CO on Pt(111) studied by photoemission, thermal desorption spectroscopy and high resolution dynamic measurements of work function. *Surf. Sci.*, 83(1):189 – 227, 1979. doi: 10.1016/0039-6028(79)90488-6. URL http://dx.doi.org/10.1016/0039-6028(79)90488-6.

[175] T.H. Lin and G.A. Somorjai. Modulated molecular beam scattering of CO and NO from Pt(111) and the stepped Pt(557) crystal surfaces. *Surf. Sci.*, 107(2-3):573 – 585, 1981. doi: 10.1016/0039-6028(81)90546-X. URL http://dx.doi.org/10.1016/0039-6028(81)90546-X.

[176] Bene Poelsema, Robert L. Palmer, and George Comsa. A thermal He scattering study of CO adsorption on Pt(111). *Surf. Sci.*, 136(1):1 – 14, 1984. doi: 10.1016/0039-6028(84)90651-4. URL http://dx.doi.org/10.1016/0039-6028(84)90651-4.

[177] Peter J. Feibelman, B. Hammer, J. K. Norskov, F. Wagner, M. Scheffler, R. Stumpf, R. Watwe, and J. Dumesic. The CO/Pt(111) puzzle. *J. Phys. Chem. B*, 105:4018–4025, 2001. doi: 10.1021/jp002302t. URL http://dx.doi.org/10.1021/jp002302t.

[178] P. Lazic, M. Alaei, N. Atodiresei, V. Caciuc, R. Brako, and S. Blügel. Density functional theory with nonlocal correlation: A key to the solution of the CO adsorption puzzle. *Phys. Rev. B*, 81(4):045401, Jan 2010. doi: 10.1103/PhysRevB.81.045401. URL http://link.aps.org/doi/10.1103/PhysRevB.81.045401.

[179] Sarah R. Longwitz, Joachim Schnadt, Ebbe Kruse Vestergaard, Ronnie T. Vang, Erik Lægsgaard, Ivan Stensgaard, Harald Brune, and Flemming Besenbacher. High-coverage structures of carbon monoxide adsorbed on Pt(111) studied by high-pressure scanning tunneling microscopy. *J. Phys. Chem. B*, 108:14497–14502, 2004. doi: 10.1021/jp0492218. URL http://dx.doi.org/10.1021/jp0492218.

[180] C. T. Rettner, E. K. Schweizer, and C. B. Mullins. Desorption and trapping of argon at a 2H–W(100) surface and a test of the applicability of detailed balance to a nonequilibrium system. *The Journal of Chemical Physics*, 90(7):3800–3813, 1989. doi: 10.1063/1.455838. URL http://link.aip.org/link/?JCP/90/3800/1.

[181] C. T. Rettner, D. J. Auerbach, J. C. Tully, and A. W. Kleyn. Chemical dynamics at the gas-surface interface. *The Journal of Physical Chemistry*, 100(31):13021–13033, 1996. doi: 10.1021/jp9536007. URL http://pubs.acs.org/doi/abs/10.1021/jp9536007.

[182] Robert D. Goodwin. Carbon monoxide thermophysical properties from 68 to 1000 K at pressures to 100 MPa. *Journal of Physical and Chemical Reference Data*, 14(4):849–932, 1985. doi: 10.1063/1.555742. URL http://link.aip.org/link/?JPR/14/849/1.

[183] Min Chi Tsai and E. L. Muetterties. Platinum metal surface chemistry of benzene and toluene. *J. Am. Chem. Soc.*, 104:2534–2539, 1982. doi: 10.1021/ja00373a034. URL http://dx.doi.org/10.1021/ja00373a034.

[184] M. Abon, J.C. Bertolini, J. Billy, J. Massardier, and B. Tardy. Adsorption states of benzene and toluene on Pt(111): A vibrational EELS, workfunction, AES and TDS study. *Surface Science*, 162(1-3):395 – 401, 1985. doi: 10.1016/0039-6028(85)90926-4. URL http://dx.doi.org/10.1016/0039-6028(85)90926-4.

[185] J. M. Campbell, S. Seimanides, and C. T. Campbell. Probing ensemble effects in surface reactions: 2. benzene adsorption on clean and bismuth covered Pt(111). *Journal of Physical Chemistry*, 93(2):815–826, 1989. doi: 10.1021/j100339a057. URL http://pubs.acs.org/doi/pdf/10.1021/j100339a057.

[186] Chen Xu, Yi Li Tsai, and Bruce E. Koel. Adsorption of cyclohexane and benzene on ordered tin/platinum (111) surface alloys. *J. Phys. Chem.*, 98:585–593, 1994. doi: 10.1021/j100053a038. URL http://dx.doi.org/10.1021/j100053a038.

[187] P. S. Weiss and D. M. Eigler. Site dependence of the apparent shape of a molecule in scanning tunneling micoscope images: Benzene on Pt111. *Phys. Rev. Lett.*, 71(19):3139–3142, Nov 1993. doi: 10.1103/PhysRevLett.71.3139. URL http://link.aps.org/doi/10.1103/PhysRevLett.71.3139.

[188] A. Wander, G. Held, R.Q. Hwang, G.S. Blackman, M.L. Xu, P. de Andres, M.A. Van Hove, and G.A. Somorjai. A diffuse LEED study of the adsorption structure of disordered benzene on Pt(111). *Surface Science*, 249(1-3):21 – 34, 1991. doi: 10.1016/0039-6028(91)90830-L. URL http://dx.doi.org/10.1016/0039-6028(91)90830-L.

[189] J Somers, M.E Bridge, D.R Lloyd, and T McCabe. An ARUPS investigation of benzene on Pt(111): Evidence for distortion. *Surface Science*, 181(3):L167 – L170, 1987. doi: 10.1016/0039-6028(87)90190-7. URL http://dx.doi.org/10.1016/0039-6028(87)90190-7.

[190] J. A. Horsley, J. Stohr, A. P. Hitchcock, D. C. Newbury, A. L. Johnson, and F. Sette. Resonances in the K shell excitation spectra of benzene and pyridine: Gas phase, solid, and chemisorbed states. *The Journal of Chemical Physics*, 83(12):6099–6107, 1985. doi: 10.1063/1.449601. URL http://link.aip.org/link/?JCP/83/6099/1.

[191] P. Sautet and M.-L. Bocquet. Shape of molecular adsorbates in STM images: A theoretical study of benzene on Pt(111). *Phys. Rev. B*, 53(8):4910–4925, Feb 1996. doi: 10.1103/PhysRevB.53.4910. URL http://link.aps.org/doi/10.1103/PhysRevB.53.4910.

[192] E. L. Garfunkel, M. H. Farias, and G. A. Somorjai. The modification of benzene and carbon monoxide adsorption on platinum(111) by the coadsorption of potassium or sulfur. *J. Am. Chem. Soc.*, 107:349–353, 1985. doi: 10.1021/ja00288a013. URL http://dx.doi.org/10.1021/ja00288a013.

[193] Mark Saeys, Marie-Françoise Reyniers, and Guy B. Marin. Density functional study of benzene adsorption on Pt(111). *J. Phys. Chem. B*, 106:7489 – 7498, 2002. doi: 10.1021/jp0201231. URL http://dx.doi.org/10.1021/jp0201231.

[194] Adam F. Lee, K.Wilson, and Richard M. Lambert. On the coverage-dependent adsorption geometry of benzene adsorbed on Pd(111): A study by fast XPS and NEXAFS. *J. Phys. Chem. B*, 104:11729–11733, 2000. doi: 10.1021/jp002635q. URL http://pubs.acs.org/doi/full/10.1021/jp002635q.

[195] M. Bäumer, J. Libuda, and H.-J. Freund. Metal deposits on thin well ordered oxide films: Morphology, adsorption and reactivity. In *Chemisorption and Reactivity on Supported Clusters and Thin Films*, NATO ASI Ser. Vol. E, pages 61 – 104. Kluwer Acad. Publ, 1997.

[196] Marcus Bäumer and Hans-Joachim Freund. Metal deposits on well-ordered oxide films. *Prog. Surf. Sci.*, 61(7-8):127 – 198, 1999. doi: 10.1016/S0079-6816(99)00012-X. URL http://dx.doi.org/10.1016/S0079-6816(99)00012-X.

[197] G. H. Vurens, M. Salmeron, and G. A. Somorjai. Structure, composition and chemisorption studies of thin ordered iron oxide films on platinum (111). *Surface Science*, 201(1-2): 129 – 144, 1988. doi: 10.1016/0039-6028(88)90602-4. URL http://dx.doi.org/10.1016/0039-6028(88)90602-4.

[198] G. H. Vurens, V. Maurice, M. Salmeron, and G. A. Somorjai. Growth, structure and chemical properties of FeO overlayers on Pt(100) and Pt(111). *Surface Science*, 268(1-3):170 – 178, 1992. doi: 10.1016/0039-6028(92)90960-E. URL http://dx.doi.org/10.1016/0039-6028(92)90960-E.

[199] H.C. Galloway, J.J. Benítez, and M. Salmeron. The structure of monolayer films of FeO on Pt(111). *Surface Science*, 298(1):127 – 133, 1993. doi: 10.1016/0039-6028(93)90089-3. URL http://dx.doi.org/10.1016/0039-6028(93)90089-3.

[200] W. Weiss, A. Barbieri, M. A. Van Hove, and G. A. Somorjai. Surface structure determination of an oxide film grown on a foreign substrate: Fe_3O_4 multilayer on Pt(111) identified by low energy electron diffraction. *Phys. Rev. Lett.*, 71(12):1848–1851, Sep 1993. doi: 10.1103/PhysRevLett.71.1848. URL http://dx.doi.org/10.1103/PhysRevLett.71.1848.

[201] A. Barbieri, W. Weiss, M.A. Van Hove, and G.A. Somorjai. Magnetite $Fe_3O_4(111)$: Surface structure by LEED crystallography and energetics. *Surface Science*, 302(3):259 – 279, 1994. doi: 10.1016/0039-6028(94)90832-X. URL http://dx.doi.org/10.1016/0039-6028(94)90832-X.

[202] W. Weiss. Structure and composition of thin epitaxial iron oxide films grown onto Pt(111). *Surface Science*, 377-379:943 – 947, 1997. doi: 10.1016/S0039-6028(96)01526-9. URL http://dx.doi.org/10.1016/S0039-6028(96)01526-9.

[203] Y. J. Kim, C. Westphal, R. X. Ynzunza, Z. Wang, H. C. Galloway, M. Salmeron, M. A. Van Hove, and C. S. Fadley. The growth of iron oxide films on Pt(111): a combined XPD, STM, and LEED study. *Surface Science*, 416(1-2):68 – 111, 1998. doi: 10.1016/S0039-6028(98)00506-8. URL http://dx.doi.org/10.1016/S0039-6028(98)00506-8.

[204] Y. Q. Cai, M. Ritter, W. Weiss, and A. M. Bradshaw. Valence-band structure of epitaxially grown $Fe_3O_4(111)$ films. *Phys. Rev. B*, 58(8):5043–5051, Aug 1998. doi: 10.1103/PhysRevB.58.5043. URL http://dx.doi.org/10.1103/PhysRevB.58.5043.

[205] M. Ritter and W. Weiss. $Fe_3O_4(111)$ surface structure determined by LEED crystallography. *Surface Science*, 432(1-2):81 – 94, 1999. doi: 10.1016/S0039-6028(99)00518-X. URL http://dx.doi.org/10.1016/S0039-6028(99)00518-X.

[206] W. Weiss and M. Ritter. Metal oxide heteroepitaxy: Stranski-Krastanov growth for iron oxides on Pt(111). *Phys. Rev. B*, 59(7):5201–5213, Feb 1999. doi: 10.1103/PhysRevB.59.5201. URL http://dx.doi.org/10.1103/PhysRevB.59.5201.

[207] Sh. K. Shaikhutdinov, M. Ritter, X.-G. Wang, H. Over, and W. Weiss. Defect structures on epitaxial $Fe_3O_4(111)$ films. *Phys. Rev. B*, 60(15):11062–11069, Oct 1999. doi: 10.1103/PhysRevB.60.11062. URL http://dx.doi.org/10.1103/PhysRevB.60.11062.

[208] V. V. Roddatis, D. S. Su, C. Kuhrs, W. Ranke, and R. Schlögl. Transmission electron microscopy investigation of Fe_3O_4 films grown on Pt(111) substrates. *Thin Solid Films*, 396(1-2):78 – 83, 2001. doi: 10.1016/S0040-6090(01)01240-8. URL http://dx.doi.org/10.1016/S0040-6090(01)01240-8.

[209] Y. Joseph, G. Ketteler, C. Kuhrs, W. Ranke, W. Weiss, and R. Schlögl. On the preparation and composition of potassium promoted iron oxide model catalyst films. *Phys. Chem. Chem. Phys.*, 3:4141 – 4153, 2001. doi: 10.1039/b104263g. URL http://dx.doi.org/10.1039/b104263g.

[210] Werner Weiss and Wolfgang Ranke. Surface chemistry and catalysis on well-defined epitaxial iron-oxide layers. *Progress in Surface Science*, 70(1-3):1 – 151, 2002. doi: 10.1016/S0079-6816(01)00056-9. URL http://dx.doi.org/10.1016/S0079-6816(01)00056-9.

[211] C. Lemire, R. Meyer, V.E. Henrich, Sh. Shaikhutdinov, and H.-J. Freund. The surface structure of $Fe_3O_4(111)$ films as studied by CO adsorption. *Surf. Sci.*, 572(1):103 – 114, 2004. doi: 10.1016/j.susc.2004.08.033. URL http://dx.doi.org/10.1016/j.susc.2004.08.033.

[212] L. Zhu, K. L. Yao, and Z. L. Liu. First-principles study of the polar (111) surface of Fe_3O_4. *Phys. Rev. B*, 74(3):035409, Jul 2006. doi: 10.1103/PhysRevB.74.035409. URL http://dx.doi.org/10.1103/PhysRevB.74.035409.

[213] E. J. W. Verwey. Electronic conduction of magnetite (Fe_3O_4) and its transition point at low temperatures. *Nature*, 144:327–328, 1939. doi: 10.1038/144327b0. URL http://dx.doi.org/10.1038/144327b0.

[214] R. Meyer, S. K. Shaikhutdinov, and H.-J. Freund. CO oxidation on a $Pd/Fe_3O_4(111)$ model catalyst. *Z. Phys. Chem.*, 218:905–914, 2004. doi: 10.1524/zpch.218.8.905.35983. URL http://dx.doi.org/10.1524/zpch.218.8.905.35983.

[215] T. Schalow, B. Brandt, D. E. Starr, M. Laurin, S. Schauermann, Sh. K. Shaikhutdinov, J. Libuda, and H.-J. Freund. Oxygen-induced restructuring of a Pd/Fe_3O_4 model catalyst. *Catalysis Letters*, 107:189–196, 2006. doi: 10.1007/s10562-005-0007-5. URL http://dx.doi.org/10.1007/s10562-005-0007-5.

[216] T. Schalow, B. Brandt, D. E. Starr, M. Laurin, S. K. Shaikhutdinov, S. Schauermann, J. Libuda, and H.-J. Freund. Particle size dependent adsorption and reaction kinetics on reduced and partially oxidized Pd nanoparticles. *Phys. Chem. Chem. Phys.*, 9:1347–1361, 2007. doi: 10.1039/b614546a. URL http://www.rsc.org/ej/CP/2007/b614546a.pdf.

[217] Ryszard Lamber, Stefan Wetjen, and Nils I. Jaeger. Size dependence of the lattice parameter of small palladium particles. *Phys. Rev. B*, 51(16):10968–10971, Apr 1995. doi: 10.1103/PhysRevB.51.10968. URL http://link.aps.org/doi/10.1103/PhysRevB.51.10968.

[218] S. A. Nepijko, M. Klimenkov, M. Adelt, H. Kuhlenbeck R. Schlögl, and H.-J. Freund. Structural investigation of palladium clusters on $\gamma - Al_2O_3(111)/NiAl(110)$ with transmission electron microscopy. *Langmuir*, 15:5309 – 5313, 1999. doi: 10.1021/la981012p. URL http://dx.doi.org/10.1021/la981012p.

[219] Chih-Ming Lin, Tsu-Lien Hung, Yen-Heng Huang, Kung-Te Wu, Mau-Tsu Tang, Chih-Hao Lee, C. T. Chen, and Y. Y. Chen. Size-dependent lattice structure of palladium studied by X-ray absorption spectroscopy. *Physical Review B (Condensed Matter and Materials Physics)*, 75(12):125426, 2007. doi: 10.1103/PhysRevB.75.125426. URL http://link.aps.org/abstract/PRB/v75/e125426.

[220] I. Aruna, B. R. Mehta, L. K. Malhotra, and S. M. Shivaprasad. Size dependence of core and valence binding energies in Pd nanoparticles: Interplay of quantum confinement and coordination reduction. *J. Appl. Phys.*, 104(6):064308, 2008. doi: 10.1063/1.2973682. URL http://link.aip.org/link/?JAP/104/064308/1.

[221] M. Klimenkov, S. Nepijko, H. Kuhlenbeck, M. Bäumer, R. Schlögl, and H. J. Freund. The structure of Pt-aggregates on a supported thin aluminum oxide film in comparison with unsupported alumina: a transmission electron microscopy study. *Surf. Sci.*, 391(1-3):27 – 36, 1997. doi: 10.1016/S0039-6028(97)00449-4. URL http://dx.doi.org/10.1016/S0039-6028(97)00449-4.

[222] S. A. Nepijko, M. Klimenkov, H. Kuhlenbeck, D. Zemlyanov, D. Herein, R. Schlögl, and H. J. Freund. TEM study of tantalum clusters on $Al_2O_3(111)/NiAl(110)$. *Surf. Sci.*, 412-413:192 – 201, 1998. doi: 10.1016/S0039-6028(98)00387-2. URL http://dx.doi.org/10.1016/S0039-6028(98)00387-2.

[223] G. Apai, J. F. Hamilton, J. Stohr, and A. Thompson. Extended X-ray absorption fine structure of small Cu and Ni clusters: Binding-energy and bond-length changes with cluster size. *Phys. Rev. Lett.*, 43(2):165–169, Jul 1979. doi: 10.1103/PhysRevLett.43.165. URL http://link.aps.org/doi/10.1103/PhysRevLett.43.165.

[224] P. A. Montano, W. Schulze, B. Tesche, G. K. Shenoy, and T. I. Morrison. Extended X-ray-absorption fine-structure study of Ag particles isolated in solid argon. *Phys. Rev. B*, 30(2):672–677, Jul 1984. doi: 10.1103/PhysRevB.30.672. URL http://link.aps.org/doi/10.1103/PhysRevB.30.672.

[225] J.T. Miller, A.J. Kropf, Y. Zha, J.R. Regalbuto, L. Delannoy, C. Louis, E. Bus, and J.A. van Bokhoven. The effect of gold particle size on AuAu bond length and reactivity toward oxygen in supported catalysts. *J. Catal.*, 240(2):222 – 234, 2006. doi: 10.1016/j.jcat.2006.04.004. URL http://dx.doi.org/10.1016/j.jcat.2006.04.004.

[226] Sven Kruger, Stefan Vent, Folke Nortemann, Markus Staufer, and Notker Rösch. The average bond length in Pd clusters Pd_n, n = 4–309: A density-functional case study on the scaling of cluster properties. *The Journal of Chemical Physics*, 115(5):2082–2087, 2001. doi: 10.1063/1.1383985. URL http://link.aip.org/link/?JCP/115/2082/1.

[227] Ilya V. Yudanov, Riadh Sahnoun, Konstantin M. Neyman, and Notker Rösch. Metal nanoparticles as models of single crystal surfaces and supported catalysts: Density functional study of size effects for CO/Pd(111). *The Journal of Chemical Physics*, 117(21):9887–9896, 2002. doi: 10.1063/1.1516798. URL http://link.aip.org/link/?JCP/117/9887/1.

[228] P Nava, M Sierka, and R Ahlrichs. Effects of ligand coverage on properties of palladium clusters. a density functional theory study. *Phys. Chem. Chem. Phys.*, 6(23):5338–5346, 2004. doi: 10.1039/b413110j. URL http://dx.doi.org/10.1039/b413110j.

[229] W. J. Huang, R. Sun, J. Tao, L. D. Menard, and R. G. Nuzzoand J. M. Zuo. Coordination-dependent surface atomic contraction in nanocrystals revealed by coherent diffraction. *Nat. Mater.*, 7:308 – 313, 2008. doi: 10.1038/nmat2132. URL http://dx.doi.org/10.1038/nmat2132.

[230] M. G. Mason. Electronic structure of supported small metal clusters. *Phys. Rev. B*, 27(2): 748–762, Jan 1983. doi: 10.1103/PhysRevB.27.748. URL http://link.aps.org/doi/10.1103/PhysRevB.27.748.

[231] G. K. Wertheim, S. B. DiCenzo, and D. N. E. Buchanan. Noble- and transition-metal clusters: The d bands of silver and palladium. *Phys. Rev. B*, 33(8):5384–5390, Apr 1986. doi: 10.1103/PhysRevB.33.5384. URL http://link.aps.org/doi/10.1103/PhysRevB.33.5384.

[232] G. K. Wertheim. Electronic structure of metal clusters. *Zeitschrift für Physik D Atoms, Molecules and Clusters*, 12:319–326, 1988. doi: 10.1007/BF01426965. URL http://dx.doi.org/10.1007/BF01426965.

[233] Hemantkumar N. Aiyer, V. Vijayakrishnan, G.N. Subbanna, and C.N.R. Rao. Investigations of Pd clusters by the combined use of HREM, STM, high-energy spectroscopies and tunneling conductance measurements. *Surface Science*, 313(3):392 – 398, 1994. doi: 10.1016/0039-6028(94)90059-0. URL http://dx.doi.org/10.1016/0039-6028(94)90059-0.

[234] A. Sandell, J. Libuda, P. A. Bruhwiler, S. Andersson, A. J. Maxwell, M. Baumer, N. Martensson, and H. J. Freund. Interaction of CO with Pd clusters supported on a thin alumina film. *J. Vac. Sci. Technol. A*, 14(3):1546–1551, 1996. doi: 10.1116/1.580293. URL http://link.aip.org/link/?JVA/14/1546/1.

[235] B. Balamurugan and Toshiro Maruyama. Size-modified d bands and associated interband absorption of Ag nanoparticles. *Journal of Applied Physics*, 102(3):034306, 2007. doi: 10.1063/1.2767837. URL http://link.aip.org/link/?JAP/102/034306/1.

[236] A. Sandell, J. Libuda, P. Brühwiler, S. Andersson, A. Maxwell, M. Bäumer, N. Mårtensson, and H. J. Freund. Electron spectroscopy studies of small deposited metal particles. *Journal of Electron Spectroscopy and Related Phenomena*, 76:301 – 306, 1995. doi: 10.1016/0368-2048(95)02422-0. URL http://dx.doi.org/10.1016/0368-2048(95)02422-0.

[237] B. Richter, H. Kuhlenbeck, H.-J. Freund, and P. S. Bagus. Cluster core-level binding-energy shifts: The role of lattice strain. *Phys. Rev. Lett.*, 93(2):026805, Jul 2004. doi: 10.1103/PhysRevLett.93.026805. URL http://link.aps.org/doi/10.1103/PhysRevLett.93.026805.

[238] Jose A. Rodriguez, Robert A. Campbell, and D. Wayne Goodman. Electronic interactions in bimetallic systems: Core-level binding energy shifts. *The 37th Annual Symposium of the American Vacuum Society*, 9(3):1698–1702, 1991. doi: 10.1116/1.577489. URL http://link.aip.org/link/?JVA/9/1698/1.

[239] Wei Zhang, Jan-Henrik Fischer-Wolfarth, Mikowai Lewandowski, Jose-Manuel Flores-Camacho, Shamil Shaikhutdinov, Swetlana Schauermann, Hans-Joachim Freund Dan

Sheng Su, and Robert Schlögel. TEM investigations of the metal support interface for Pd and Pt particles on Fe_3O_4. in preparation, 2010.

[240] A Schlegel, S F Alvarado, and P Wachter. Optical properties of magnetite (Fe_3O_4). *J. Phys. C*, 12:1158–1165, 1979. doi: 10.1088/0022-3719/12/6/027.

[241] A. Y-C. Yu and W. E. Spicer. Photoemission and optical studies of the electronic structure of palladium. *Phys. Rev.*, 169(3):497 – 507, May 1968. doi: 10.1103/PhysRev.169.497. URL http://link.aps.org/doi/10.1103/PhysRev.169.497.

[242] P. B. Johnson and R. W. Christy. Optical constants of transition metals: Ti, V, Cr, Mn, Fe, Co, Ni, and Pd. *Phys. Rev. B*, 9(12):5056–5070, Jun 1974. doi: 10.1103/PhysRevB.9.5056. URL http://dx.doi.org/10.1103/PhysRevB.9.5056.

[243] J. H. Weaver and R. L. Benbow. Low-energy interband absorption in Pd. *Phys. Rev. B*, 12(8):3509–3510, Oct 1975. doi: 10.1103/PhysRevB.12.3509. URL http://link.aps.org/doi/10.1103/PhysRevB.12.3509.

[244] J Lafait, F Abeles, M L Theye, and G Vuye. Determination of the infrared optical constants of highly reflecting materials by means of surface plasmon excitation-application to Pd. *Journal of Physics F: Metal Physics*, 8(7):1597–1606, 1978. URL http://stacks.iop.org/0305-4608/8/1597.

[245] G. Doyen and G. Ertl. Theory of carbon monoxide chemisorption on transition metals. *Surface Science*, 43(1):197 – 229, 1974. doi: 10.1016/0039-6028(74)90228-3. URL http://dx.doi.org/10.1016/0039-6028(74)90228-3.

[246] R. J. Behm, K. Christmann, G. Ertl, and M. A. Van Hove. Adsorption of CO on Pd(100). *The Journal of Chemical Physics*, 73(6):2984–2995, 1980. doi: 10.1063/1.440430. URL http://link.aip.org/link/?JCP/73/2984/1.

[247] T. Schalow and B. Brandt. Initial sticking probabilities for unstabilized Pd particles supported on Fe_3O_4. unpublished, September 2005.

[248] T. Mitsui, M. K. Rose, E. Fomin, D. F. Ogletree, and M. Salmeron. Diffusion and pair interactions of CO molecules on Pd(111). *Phys. Rev. Lett.*, 94(3):036101, Jan 2005. doi: 10.1103/PhysRevLett.94.036101. URL http://link.aps.org/doi/10.1103/PhysRevLett.94.036101.

[249] M. K. Rose, T. Mitsui, J. Dunphy, A. Borg, D. F. Ogletree, M. Salmeron, and P. Sautet. Ordered structures of CO on Pd(111) studied by STM. *Surface Science*, 512(1-2):48 – 60, 2002. doi: 10.1016/S0039-6028(02)01560-1. URL http://dx.doi.org/10.1016/S0039-6028(02)01560-1.

[250] A. M. Bradshaw and F. M. Hoffmann. The chemisorption of carbon monoxide on palladium single crystal surfaces: IR spectroscopic evidence for localised site adsorption. *Surface Science*, 72(3):513 – 535, 1978. doi: 10.1016/0039-6028(78)90367-9. URL http://dx.doi.org/10.1016/0039-6028(78)90367-9.

[251] A. Ortega, F.M. Hoffman, and A.M. Bradshaw. The adsorption of CO on Pd(100) studied by IR reflection absorption spectroscopy. *Surface Science*, 119(1):79 – 94, 1982. doi: 10.1016/0039-6028(82)90189-3. URL http://dx.doi.org/10.1016/0039-6028(82)90189-3.

[252] H. Ohtani, M.A. Van Hove, and G.A. Somorjai. LEED intensity analysis of the surface structures of Pd(111) and of CO adsorbed on Pd(111) in a $(\sqrt{3} \times \sqrt{3})$ r30° arrangement. *Surface Science*, 187(2-3):372 – 386, 1987. doi: 10.1016/S0039-6028(87)80063-8. URL http://dx.doi.org/10.1016/S0039-6028(87)80063-8.

[253] M. Tüshaus, W. Berndt, H. Conrad, A. M. Bradshaw, and B. Persson. Understanding the structure of high coverage CO adlayers. *Applied Physics A*, 51:91–98, 1990. doi: 10.1007/BF00324270. URL http://www.springerlink.com/content/hx11r8182813458k/.

[254] Tobias Schalow. *Bildung und katalytische Aktivit¨at partiell oxidierter Pd-Nanopartikel*. PhD thesis, Technische Universität Berlin, 2006. URL http://opus.kobv.de/tuberlin/volltexte/2007/1474/.

[255] Friedrich M. Hoffmann. Infrared reflection-absorption spectroscopy of adsorbed molecules. *Surface Science Reports*, 3(2-3):107 – 107, 1983. doi: 10.1016/0167-5729(83)90001-8. URL http://dx.doi.org/10.1016/0167-5729(83)90001-8.

[256] T. Gießel, O. Schaff, C. J. Hirschmugl, V. Fernandez, K. M. Schindler, A. Theobald, S. Bao, R. Lindsay, W. Berndt, A. M. Bradshaw, C. Baddeley, A. F. Lee, R. M. Lambert, and D. P. Woodruff. A photoelectron diffraction study of ordered structures in the chemisorption system Pd(111)-CO. *Surface Science*, 406(1-3):90 – 102, 1998. doi: 10.1016/S0039-6028(98)00098-3. URL http://dx.doi.org/10.1016/S0039-6028(98)00098-3.

[257] J. Libuda and H.-J. Freund. Reaction kinetics on complex model catalysts under single scattering conditions. *J. Phys. Chem. B*, 106:4901–4915, 2002. doi: 10.1021/jp014055e. URL http://pubs.acs.org/doi/abs/10.1021/jp014055e.

[258] B. Hammer, Y. Morikawa, and J. K. Nørskov. CO chemisorption at metal surfaces and overlayers. *Phys. Rev. Lett.*, 76(12):2141–2144, Mar 1996. doi: 10.1103/PhysRevLett.76.2141. URL http://link.aps.org/doi/10.1103/PhysRevLett.76.2141.

[259] M.P. Kiskinova and G.M. Bliznakov. Adsorption and coadsorption of carbon monoxide and hydrogen on Pd(111). *Surface Science*, 123(1):61 – 76, 1982. doi: 10.1016/0039-6028(82)90129-7. URL http://dx.doi.org/10.1016/0039-6028(82)90129-7.

[260] A. Noordermeer, G.A. Kok, and B.E. Nieuwenhuys. Comparison between the adsorption properties of Pd(111) and PdCu(111) surfaces for carbon monoxide and hydrogen. *Surface Science*, 172(2):349 – 362, 1986. doi: 10.1016/0039-6028(86)90760-0. URL http://dx.doi.org/10.1016/0039-6028(86)90760-0.

[261] Xingcai Guo and Jr. John T. Yates. Dependence of effective desorption kinetic parameters on surface coverage and adsorption temperature: CO on Pd(111). *J. Chem. Phys.*, 90(11): 6761–6766, 1989. doi: 10.1063/1.456294. URL http://link.aip.org/link/?JCP/90/6761/1.

[262] H. Conrad, G. Ertl, J. Kocha, and E.E. Lattaa. Adsorption of CO on Pd single crystal surfaces. *Surf. Sci.*, 43:462–480, 1974. doi: 10.1016/0039-6028(74)90270-2. URL http://dx.doi.org/10.1016/0039-6028(74)90270-2.

[263] H. Conrad, G. Ertl, and J. Küppers. Interactions between oxygen and carbon monoxide on a Pd(111) surface. *Surf. Sci.*, 76:323–342, 1978. doi: 10.1016/0039-6028(78)90101-2. URL http://dx.doi.org/10.1016/0039-6028(78)90101-2.

[264] G. Ertl and J. Kocha. Adsorption of CO on a palladium (111) surface. *Zeitschrift für Naturforschung A*, A 25:1906, 1970.

[265] Janos Szanyi, W. Kevin Kuhn, and D. Wayne Goodman. CO adsorption on Pd(111) and Pd(100): Low and high pressure correlations. *39th National Symposium of the American Vacuum Society*, 11(4):1969–1974, 1993. doi: 10.1116/1.578532. URL http://link.aip.org/link/?JVA/11/1969/1.

[266] R. D. Ramsier, K. W. Lee, and J. T. Yates. CO adsorption on stepped Pd(112): studies by thermal and electron stimulated desorption. *Surface Science*, 322(1-3):243 – 255, 1995. doi: 10.1016/0039-6028(95)90034-9. URL http://dx.doi.org/10.1016/0039-6028(95)90034-9.

[267] C. R. Henry, C. Chapon, and C. Duriez. Adsorption - desorption kinetics on epitaxially oriented palladium clusters. *Zeitschrift für Physik D Atoms, Molecules and Clusters*, 19: 347–351, 1991. doi: 10.1007/BF01448326.

[268] C. R. Henry, C. Chapon, and C. Duriez. Precursor state in the chemisorption of co on supported palladium clusters. *J. Chem. Phys.*, 95:700–705, 1991. doi: 10.1063/1.461419. URL http://link.aip.org/link/?JCPSA6/95/700/1.

[269] C.R. Henry, C. Chapon, C. Goyhenex, and R. Monot. Size effect in the CO chemisorption on palladium clusters supported on magnesium oxide. *Surf. Sci.*, 272:283–288, 1992. doi: 10.1016/0039-6028(92)91451-G.

[270] C. M. Chan, R. Aris, and W. H. Weinberg. An analysis of thermal desorption mass spectra. I. *Applications of Surface Science*, 1(3):360 – 376, 1978. doi: 10.1016/0378-5963(78)90038-7. URL http://dx.doi.org/10.1016/0378-5963(78)90038-7.

[271] P. Sautet, M. K. Rose, J. C. Dunphy, S. Behler, and M. Salmeron. Adsorption and energetics of isolated CO molecules on Pd(111). *Surface Science*, 453(1-3):25 – 31, 2000. doi: 10.1016/S0039-6028(00)00243-0. URL http://dx.doi.org/10.1016/S0039-6028(00)00243-0.

[272] Ilya V. Yudanov, Manuela Metzner, Alexander Genest, and Notker Rösch. Size-dependence of adsorption properties of metal nanoparticles: A density functional study on palladium nanoclusters. *J. Phys. Chem. C*, 112:20269 – 20275, 2008. doi: 10.1021/jp8075673. URL http://dx.doi.org/10.1021/jp8075673.

[273] J. Libuda, I. Meusel, J. Hoffmann, J. Hartmann, L. Piccolo, C. R. Henry, and H.-J. Freund. The CO oxidation kinetics on supported Pd model catalysts: A molecular beam/in situ time-resolved infrared reflection absorption spectroscopy study. *J. Chem. Phys.*, 114(10): 4669–4684, 2001. doi: 10.1063/1.1342240. URL http://link.aip.org/link/?JCP/114/4669/1.

[274] Ilya V. Yudanov, Riadh Sahnoun, Konstantin M. Neyman, Notker Rösch, Jens Hoffmann, Swetlana Schauermann, Viktor Johanek, Holger Unterhalt, Gunther Rupprechter, Jörg Libuda, and Hans-Joachim Freund. CO adsorption on Pd nanoparticles: Density functional and vibrational spectroscopy studies. *J. Phys. Chem. B*, 107(1):255–264, 2003. doi: 10.1021/jp022052b. URL http://dx.doi.org/10.1021/jp022052b.

[275] Evgeny Shustorovich and Harrell Sellers. The UBI-QEP method: A practical theoretical approach to understanding chemistry on transition metal surfaces. *Surface Science Reports*, 31(1-3):1 – 119, 1998. doi: 10.1016/S0167-5729(97)00016-2. URL http://dx.doi.org/10.1016/S0167-5729(97)00016-2.

[276] Kazuo Watanabe, Yoshiyasu Matsumoto, Margarethe Kampling, Katharina Al-Shamery, and Hans-Joachim Freund. Photochemistry of methane on Pd/Al_2O_3 model catalysts: Control of photochemistry on transition metal surfaces. *Angewandte Chemie International Edition*, 38:2192 – 2194, 1999. doi: 10.1002/(SICI)1521-3773(19990802)38:15<2192::AID-ANIE2192>3.0.CO;2-X. URL http://dx.doi.org/10.1002/(SICI)1521-3773(19990802)38:15<2192::AID-ANIE2192>3.0.CO;2-X.

[277] Daniel Mulugeta, Ki Hyun Kim, Kazuo Watanabe, Dietrich Menzel, and Hans-Joachim Freund. Size effects in thermal and photochemistry of NO_2 on Ag nanoparticles. *Phys. Rev. Lett.*, 101(14):146103, 2008. doi: 10.1103/PhysRevLett.101.146103. URL http://link.aps.org/abstract/PRL/v101/e146103.

List of Figures

List of Tables

Danksagung

I would like to thank Prof. Freund for the great opportunity to work in the CP department of the Fritz-Haber-Institute. The offered project to build a new machine and obtain information about gas-surface energetics was very interesting with its diverse aspects, comprising work on hardware, software and scientific results. Basically, it was a lot of fun in an inspiring environment!

Accordingly, I would like to thank Prof. Helmut Winter for taking the responsibility for this work at the Humboldt-University Berlin.

During my PhD time I had the great pleasure to work in the molecular beam group with: Swetlana Schauermann, being always available for discussions and invaluable feedback, Björn Brandt, who introduced me to UHV machines and molecular beam methods, Wiebke Ludwig and Aditya Savara for the enlightening discussions and the quick and effective help whenever I needed it. Jose-Manuel Flores-Camacho, who's expertise in optics was very helpful, and Matthias Peters joined the microcalorimeter experiment and will continue the just started scientific efforts. Of foremost importance for the success of my work was the contribution of Jens Hartmann who really racked his brains over the proper design of the machine.
Thank all of you for the good time!

I would like to thank the people in the department of chemical physics providing a enjoyable working atmosphere and for their permanent availability for advice and support.

All workshops at the Fritz-Haber-Institute were involved during the construction of the new microcalorimeter and I always enjoyed the discussions about possible solutions for my special problems. In the electronic workshop, I would like to thank Georg Heyne, Viktor Platschkowski and Wilko Genz whom I had a lot of contact with and Harald Fischer for all the unexpected emails. In the chemical physics department, a lot of time would have been wasted if not Klaus-Peter Vogelgesang would be there to help with his expertise in metal machining. It was always a pleasure and amusing to enter your workshop.

I am thankful to Prof. Charlie Campbell at UW Seattle who was willing to start a collaboration and let us participate in his experience in single crystal adsorption microcalorimetry. I enjoyed the two stays of Jason Farmer who joined the early stage of the construction and the beginning of the adsorption measurements on Pd particles.

Thank you for your help and good luck for the future!

My family gave me an overwhelming amount of support. **I love you!**

Selbständigkeitserklärung

Ich erkläre, dass ich die vorliegende Arbeit selbständig und nur unter Verwendung der angegebenen Literatur und Hilfsmittel angefertigt habe.

Berlin, den 15.09.2010 Jan-Henrik Fischer-Wolfarth (geb. Fischer)